Fakultät für Medizin

Institute of Biological and Medical Imaging, Helmholtz Zentrum München

Rapid Functional Optoacoustic Imaging of Brain Activity in Murine and Zebrafish Models

Moritz Kneipp

Vollständiger Abdruck der von der Fakultät für Medizin der Technischen Universität München zur Erlangung des akademischen Grades eines

Doctor of Philosophy (Ph.D.)

genehmigten Dissertation.

Vorsitzender: Univ.-Prof. Dr. Arthur Konnerth

Betreuer: Univ.-Prof. Dr. Daniel Razansky

Prüfer der Dissertation:

1. Univ.-Prof. Dr. Vasilis Ntziachristos

2. Univ.- Prof. Dr. Gil Westmeyer

Die Dissertation wurde am 17.04.2015 bei der Fakultät für Medizin der Technischen Universität München eingereicht und durch die Fakultät für Medizin am 09.06.2015 angenommen.

For my family and friends.

Abstract

Longitudinal functional imaging studies of neurological diseases are key in identifying the disease progression and possible therapeutic interventions. Optoacoustic imaging is an emerging method that promises high tissue penetration and non-invasive imaging of optical contrast in whole volumes. This thesis demonstrates the advantages of optoacoustic imaging and works to apply the method for neuroimaging applications. In doing so, the applicability of real-time functional optoacoustic imaging for monitoring of stroke progression in the whole brain of living animals is demonstrated. The middle cerebral artery occlusion model was used to model stroke in mice, and an asymmetry of deoxygenated haemoglobin in the brain is observed as a region of hypoxia in the hemisphere affected by the ischaemic event. Furthermore, the penumbra is visualised *in vivo* as a localised haemodynamically-compromised area adjacent to the region of the stroke-induced perfusion deficit.

In efforts to increase the achievable resolution, a hybrid focus optoacoustic microscope is developed, providing a smooth transition from optical resolution in superficial layers to acoustic resolution at greater depths within intensely scattering tissue layers. However, a variety of acoustic and light-related effects introduced by the adult murine skull severely compromise the performance of optoacoustics in transcranial imaging and microscopy. An adapted perfusion-based fixation technique is used to better quantify effects of the skull on the optoacoustically-generated signals, independently from other possible *in vivo* imaging artefacts. It is shown that strong low-pass filtering characteristics of adult murine skulls may significantly deteriorate the achievable spatial resolution in non-invasive animal studies, limiting the possibility of imaging capillary structures in deep brain tissues where light focusing is not possible. Significant improvements to the minimally detectable resolution are seen through cranial windows and thinned skull experiments.

While imaging neural activation via haemodynamic changes is possible, direct imaging using activatable calcium indicators offers a faster response to neuronal events. Here, a real-time volumetric and multispectral (five-dimensional) optoacoustic tomography platform for imaging of neural activation deep in scattering brains is described. Experiments performed in immobilised and freely swimming larvae and in adult zebrafish brains demonstrate, for the first time, the fundamental ability to optoacoustically

track calcium dynamics in the nervous system of animals labelled with the genetically encoded calcium indicator GCaMP5G.

In summary, this thesis uses experiments with model organisms in an effort to combine the merits of optoacoustic imaging with the high impact of neuroscience.

Contents

Part I

Introduction

Chapter 1

Motivation - Neurodegenerative diseases and socioeconomic impact

The significance of neurodegenerative diseases is ever increasing in causing morbidity and mortality in the developed world [1]. This development can be largely attributed to changes in the world population demographics, where changes include the ageing population, due to increased life expectancy and the ageing of baby boomers [2].

By the year 2030, 25% of Europe's population is expected to be over 65, profoundly increasing the socioeconomic impact of the neurodegenerative diseases linked to age. These diseases include Alzheimer's disease (AD), Parkinson's disease (PD) and Motor neurone diseases (MND), with dementias creating current costs in excess of €130 billion per annum in Europe alone [3]. The total cost of brain disorders however, was estimated to be as high as €798 billion in 2010 [4]. In the United States, AD alone is projected to create costs of above 1000 billion US$ by 2050 (see Fig. 1.1) [5]. As the population ages and the occurrences of these diseases increase - the prevalence of dementias doubles every 4-5 years after the age of 60 [6]- it will therefore become vital to improve the understanding of the diseases themselves and to develop more advanced and effective treatments and therapies [2]. Without these developments, the personal, social and economic costs of neurodegenerative diseases will increase unfathomably [7]. Reducing the socioeconomic cost, could be achieved through more advanced early detection techniques, possibly limiting the severity of the disease progression [8].

Many of the neurodegenerative diseases are defined through the prop-

erties of the corresponding neuropathological lesions associated with the disease. These lesions are however not mere markers, but appear to be tied closely to the disease pathogenesis. Furthermore, many of these lesions exhibit similarities between disorders and are therefore promising targets for future therapies [2].

Structural imaging of AD has previously yielded results showing promise in finding markers for early detection of disease onset [8]. It follows, that both longitudinal and functional imaging are essential tools in understanding the progression of these diseases and are invaluable in finding suitable treatments and therapies [9], thus reducing the burden on the patients and socioeconomic system.

It is this clear need for the advancement of imaging techniques in the neuroscientific setting, that is the motivation for this thesis, where a new modality for neuroimaging is described and applied.

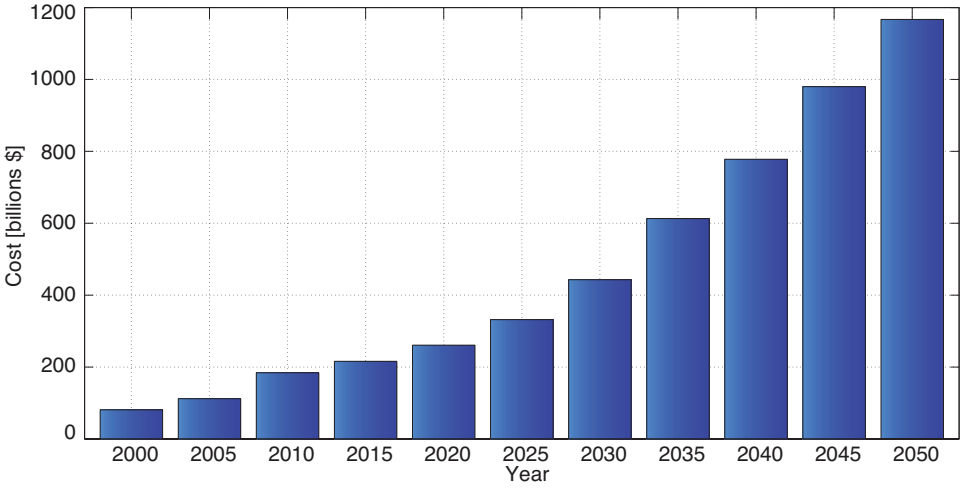

Figure 1.1: Projected cost of AD in the USA alone. Reproduced from [5].

Chapter 2

Neuroimaging

The objective of neuroimaging is to visualise the nervous system. In general, neuroimaging can be divided into structural and functional imaging. While both branches either directly or indirectly image the nervous system, their applications are different.

Structural imaging is mainly concerned with large scale changes that include tumours and injuries, where the imaging procedure aims to represent the biological system in temporally invariant datasets. In order to treat the patients, therapeutical and surgical plans are created using the information gained from the analysis of the datasets and reconstructed images. The beginnings of clinical structural neuroimaging date back to 1919 when Walter Dandy developed ventriculography, a method where x-rays were used to image the ventricular system by replacing most of the cerebral spinal fluid with a gas [10]. Current structural imaging technologies have become less invasive, requiring less extreme procedures and can produce both two-dimensional and three-dimensional imaging data.

Functional imaging deals with the diagnosis of smaller scale changes that affect the metabolic status of the nervous system [11]. Since these metabolic changes are usually directly linked to brain acitivity, time-resolved imaging can visualise the activity of brain regions and their interconnections [12]. Functional imaging has become an invaluable tool in cognitive neuroscience as well as in clinical applications. One of the earliest forms of functional imaging was electroencephalography (EEG) [13]. EEG is a one-dimensional modality that offers unprecedented safety and high temporal resolution at the millisecond scale. Its spatial resolution is however very limited. As EEG merely records the potentials at the scalp surface, reconstruction algorithms solving an ill-post inversion problem are required to produce spatial

maps of potential changes, resulting in highly artefact prone imaging data [14]. Current methods provide higher dimensional data, with the most common being functional magnetic resonance imaging (fMRI), single photon emission tomography (SPECT), positron emission tomography (PET) and optical imaging. As an example, functional MRI was first demonstrated by Belliveau et al. over 20 years ago [15]. This research proved that gadolinium could be used to image and monitor activation-related increases in the cerebral blood volume of the visual cortex upon visual stimulation. The method has seen rapid development and spread since 1991, owing largely to the fact that it is able to reliably obtain clear and reproducible brain activation data [16]. Over the years, fMRI has enabled developments producing more robust and faster processing platforms, higher field strengths and more advanced radio frequency coil systems. This, combined with imaging protocols of ever increasing sophistication have equipped the modality for future research.

Overall, these modalities produce data that is at least two-dimensional (planar images or slices), with some being able to create volumetric data. The resulting research has created new insights to the interconnections of cortical tissue and the effects that disease and injuries can have on these connections [14]. A description of the main imaging techniques used in clinics today can be found in Chapter 6.

Chapter 3

Objectives

Optoacoustics (OA) is an emerging field in biomedical imaging, with a promising future in both biological and medical research. This thesis aims to advance and equip optoacoustics for biological and preclinical neuroimaging studies. In achieving this goal, several questions and challenges arise that need answering and solving.

Can optoacoustics be used to perform functional neuroimaging studies? The power of an imaging modality lies in its ability to perform well in functional studies. Most model organisms and disease models are very well characterised with regard to their structural and anatomical information. The functional interconnections between cellular processes within tissues and between different tissues, however has yet to be characterised. It is therefore imperative to proof that optoacoustics can be used in functional studies.

Is optoacoustic imaging applicable in longitudinal studies, is it non-invasive? Most disease models do not require data from just one single time point. Disease progression and the possible inhibition of it is what is needed in understanding the disease itself and in developing drugs and therapies to treat the disease. Because invasive imaging that requires ionising radiation or surgical procedures can change the outcome of a disease, it is crucial that the new and enhanced modality is non-invasive.

Can the whole brain be imaged? Is the depth penetration high enough? Imaging large organs is challenging. All functional parameters and interconnections are however important in understanding the fundamental processes of neural activation and disease breakout and progression. If optoacoustics is to become the valuable tool it promises to be, it will have to be able to acquire whole brain data, deep within the tissue.

What are the current limitations? Improving a modality or any technology or process requires understanding the current limitations, be they related to technological, conceptual or application constraints.

What spatio-temporal resolutions can be achieved? Highly resolved data in the spatial and in the temporal domain enable analysis of the observed processes in great detail. The higher the spatio-temporal resolution achievable with optoacoustics, the greater its impact can be in the biomedical sciences.

What challenges arise when increasing the resolution? As mentioned above, limitations are not only technological in nature. Especially in biomedical research, the context and application play an immense role in deciding the outcome of a study. In biomedical imaging, the effective achievable resolution can be greatly influenced by the size and anatomy of the imaged organism. It is therefore critical to understand what difficulties and challenges a certain application creates for the chosen modality and imaging setup.

How can we monitor neural activation with optoacoustics? Is direct imaging of neural activation possible? Neural activation has been linked to functional changes in the cerebral blood flow and blood volume. Monitoring these changes can yield great insights, is however limited in its temporal resolution, because vascular responses are only secondary effects of neural activation. The possibility of direct imaging using indicators and dyes would therefore be highly beneficial.

This thesis will answer these questions on both, a theoretical and experimental basis and explain remaining challenges for optoacoustic neuroimaging.

Chapter 4

Thesis Outline

As this thesis aims to bridge the gap between the novel optoacoustic imaging modality and neuroimaging in order to combine the superior qualities of the modality with the significant impact of neurological research, several obstacles have to be overcome. This includes producing proof of optoacoustic imaging's applicability for functional neuroimaging, increasing the spatio-temporal resolution of optoacoustic imaging systems and overcoming the difficulties imposed by imaging small animal models longitudinally and non-invasively.

Part II describes the theoretical background of optoacoustics and gives first descriptions of the existing imaging modalities based on the method. It further compares optoacoustic imaging to the most common and established clinical and biological imaging modalities.

In Part III, the applicability of real-time multispectral optoacoustic tomography is investigated as a tool for monitoring stroke progression in a longitudinal functional imaging study. The middle cerebral artery occlusion model is used to induce stroke in mice. Visualising major blood vessels in the whole head is possible and the optoacoustic data show a decrease in cerebral blood volume in the cortex during occlusion. An asymmetry in the deoxygenated haemoglobin signal was identified as the penumbra – a hypoxic area surrounding the ischaemic lesion.

Part IV deals with the development of a hybrid focus optoacoustic microscope. It describes the system and its imaging performance parameters and shows results of several studies conducted with the setup, this includes imaging of zebrafish in both the larval and adult stages. Furthermore, a fixation method is described for creating biological samples perfectly suited for optimising a system prior to *in vivo* imaging. Additionally, the strong

frequency dependent attenuation effects of the murine skull are studied.

The strong attenuation effects are in part responsible for the study described in Part V. The much thinner skulls of zebrafish, together with the lower central frequency of the volumetric optoacoustic scanner allowed for direct optoacoustic imaging of neural activation, using the genetically encoded calcium indicator GCaMP5G. Mutant zebrafish are imaged as larvae in both freely swimming and immobilised settings. Freshly excised brains of adult fish are imaged to provide proof of the method's superior penetration depth, even deep into optically scattering tissues.

Part VI summarises the thesis and describes ideas and plans for future developments and studies to be conducted with regard to direct optoacoustic imaging of neural activation.

All procedures were performed in conformity with institutional guidelines for animal welfare law and approved by the local administration.

Part II

Theoretical and Technical Background

Chapter 5

Optoacoustic Imaging

This chapter introduces the theoretical background of the optoacoustic effect. It moves on to give a short description of possible biomedical applications and outlines the optoacoustic technologies developed and in development thus far.

5.1 The Optoacoustic Effect

The optoacoustic (or photoacoustic) effect was discovered by Alexander Graham Bell in 1880 and describes the formation of sound waves succeeding light absorption in a sample [17]. Herein, sound waves are generated through optical stimulation. A prerequisite for the effect is the presence of varying light intensities, this can be achieved by illuminating the sample with pulsed laser light [18], [19]. The pulsed energy deposition within the sample causes the absorbers to undergo thermal expansion, thus creating broadband ultrasound waves that propagate outwards. These pressure waves are then registered using ultrasound transducers and converted into voltages, with the amplitude of the typical N-shape signals being proportional to the energy deposited in the absorber, see Figure 5.1.

In an effort to formally describe and express the process, the following formulas are adapted from Li et al. [20] and Diebold et al. [21] and describe the process of energy absorption, local heating and the following expansion.

$$h(r) = \int_0^\tau \mu_a(r)\Phi(r,t)dt = \mu_a(r)\phi(r), \tag{5.1}$$

describes the energy $h(r)$ absorbed per volume during a pulse of length τ is dependent on the fluence rate $\Phi(r,t)$ in $(Js^{-1}m^{-2})$ and the fluence $\phi(r)$

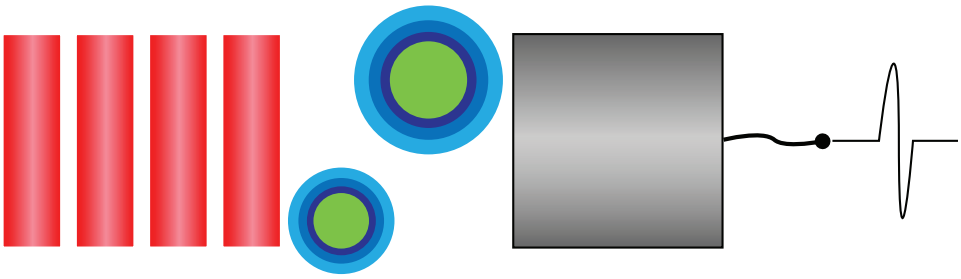

Figure 5.1: pulsed laser light (red) excites absorbers (green) in a sample. The thermal expansion creates pressure waves (blue) that are recorded by a transducer (grey), resulting in a typical N-shape signal (black).

in (Jm^{-2}), at position r. Because the excitation pulse duration is $\tau < 1\mu s$, thermal diffusion is negligible and the thermal confinement approximation holds true [22], more specifically:

$$\tau < \tau_s = \frac{d_c}{v_s}, \tag{5.2}$$

where v_s is the speed of sound and d_c the size of the absorber. In aiming for a resolution of 15 μm, we get $\tau_p < 10ns$. The local temperature rise is described by:

$$\Delta T = \frac{h}{\rho C_V}, \tag{5.3}$$

where h is the deposited energy, ρ is the volume density and C_V its heat capacity. In considering the volume to be constant for pulses below $\tau < 10ns$, with a taget resolution of $15\mu m$ [20], it follows that the pressure change is given by:

$$\Delta p = \frac{\beta \Delta T}{K_T}, \tag{5.4}$$

with β being the volume thermal expansivity in (K^{-1}) and K_T being the isothermal compressibility in $(m^2 N^{-1})$. Inserting equation (5.3) into equation (5.4) yields:

$$\Delta p = \frac{\beta h}{K_T \rho C_V}. \tag{5.5}$$

With the square of the speed of sound in the medium $v_s^2 = c_p (K_T \rho C_V)^{-1}$, the specific heat at constant pressure c_p in $(JK^{-1}g^{-1})$ and by defining the Grüneisen coefficient as $\Gamma = \beta v_s^2 / c_P$ we get

$$\Delta p = \Gamma h. \tag{5.6}$$

Using equation (5.1) we can relate the pressure change to the local optical absorption and fluence:

$$\Delta p = \Gamma \mu_a \Phi. \tag{5.7}$$

It is this pressure change that gives rise to the propagating optoacoustic waves and is therefore the source of optoacoustic data.

The most dominant and abundant absorbers in biological tissues are water and haemoglobin [23] (see Fig. 5.2). The strong absorbance of haemoglobin in the short wavelength ranges of the visible spectrum means that light cannot penetrate to deep within the tissue, thus limiting the optical imaging depth. The haemoglobin absorbance decreases however significantly in the near-infrared region of the spectrum. Conversely, the absorbance of water rises with wavelength, starting from the visible spectrum. This rise prohibits imaging in the far-infrared region of the electromagnetic spectrum. Most deep tissue optical imaging is therefore done in the imaging window of between 650 nm and 900 nm.

Biomedical imaging must not result in skin burns, it is therefore imperative that the excitation fluence remains lower than the maximum permissible exposure set by governing bodies [24]. To calculate typical values, an excitation wavelength of 800 nm is chosen. The resulting fluence maximum is $32\,\mathrm{mJ/cm^2}$ and the absorbance of blood is approximately $\mu_a = 4.22$. Using $\Gamma = 0.25$ [20], it follows that:

$$\Delta p = 0.25 \times 4.22 \times 32 = 33.8\mathrm{kPa}. \tag{5.8}$$

In the case of water [25], $K_T = 4.6 \times 10^{-10}\,\mathrm{m^2/N}$ and $\beta = 4 \times 10^{-4}\,\mathrm{K^{-}1}$ yield from Equation 5.5:

$$\Delta T = \frac{33.8 \times 10^3 \times 4.6 \times 10^{-10}}{4 \times 10^{-4}} = 39\,\mathrm{mK} \tag{5.9}$$

5.2 Optoacoustic Sources

The possible sources for optoacoustic imaging are mainly dictated by the available illumination. In order for optoacoustic signals to be created, the imaged sample has to absorb enough energy to produce a detectable optoacoustic wave. This means that samples and illumination have to be matched. In most established setups, lasers operating in and above the visible spectrum are used for illumination, thus requiring samples that absorb in this wavelength range. Black sutures and microsphere have been the samples of

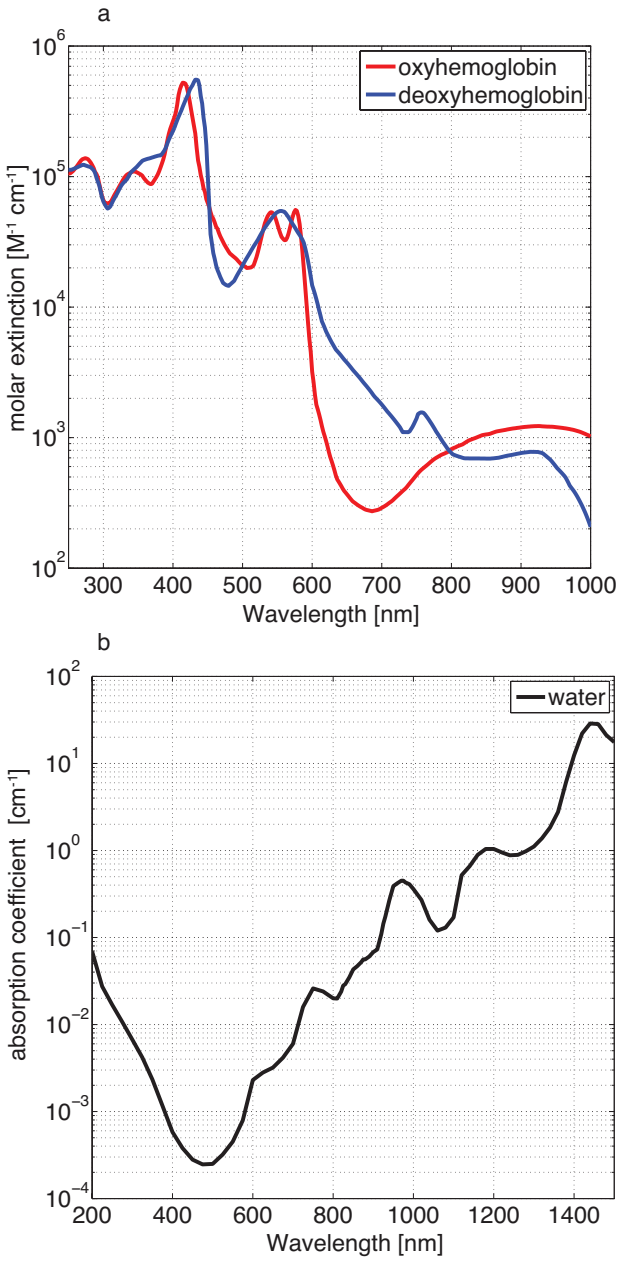

Figure 5.2: Extinction spectra of haemoglobin (a) and absorption spectrum of water (b). Reproduced from Scott Prahl, Oregon Medical Laser Center (http://omlc.ogi.edu/spectra).

choice for system characterisation and demonstration, as they exhibit strong absorption throughout the visible spectrum.

5.3 Biomedical Optoacoustic Imaging

While the underlying principles were discovered over 100 years ago, it wasn't until the 1970s, when the optoacoustic effect saw its first implementation, where photoacoustic spectroscopy was used in analytical chemistry [26]. The first imaging application in tissue mimicking media was proposed by Kruger et al in 1994 [27]. In his work, Kruger first proposed xenon flash lamps as the excitation source, not pulsed lasers. Interest in the field continued to grow and with the development of high power pulsed nanosecond lasers, biological applications became reality [28]. The growing interest and the continued efforts to develop the field are largely motivated by the fact that optoacoustics can, unlike purely optical techniques, retain resolution at depth independent of optical scattering, while still retaining spatial information of the absorption distribution map in the region of interest. With the detection being based on ultrasound, the significantly reduced scattering of ultrasound in tissues causes only minor deterioration in the achievable resolution.

5.4 Optoacoustic Imaging Setups

The optoacoustic effect has found multiple applications in biological and medical imaging, with setups becoming ever faster and higher in resolution. This section gives a short summary of current setups.

One of the first fully functional setups was described by Razansky et al. [29], [30]. This setup acquired images by rotating the sample and recording time-resolved projection data from a single element transducer. The resulting data can be reconstructed to yield very high resolution images with very little artefacts, owing to the high number of projections. This method is however slow, as only one single projection can be acquired with every laser pulse. Acquiring several slices further multiplies the acquisition time.

The natural progression was therefore to use transducer arrays to acquire signals [31], see Chapter 8 for a more detailed description. Here, each transducer element in the ring shaped array is responsible for acquiring a projection along a specific angle. This means that a full set of projections is acquired for every laser pulse, massively reducing acquisition time. However, because of technical limitations that include the finite element size and construction hindrances, the number of projections and the angle of coverage is

limited, resulting in images that are more prone to artefacts.

In enhancing the approach, fully volumetric systems have been designed and built [32], [33]. Similar to the ring shaped array, multiple elements are used to acquire a set of projections for every laser pulse. The elements are however distributed on a spherical surface, meaning that whole volumes are acquired for every excitation pulse. An example of such a setup is presented and used in Part V.

Optoacoustic microscopes have been developed using high frequency transducers [34]. They typically acquire images in a raster scanning scenario, thus creating data of whole volumes on the fly. Part IV describes such a high frequency system.

Other applications include intravascular catheter systems. As optoacoustics is able to perform spectral analysis, it could be used to differentiate harmful vessel changes, like in the case of atherosclerosis. A common approach herein is to excite optoacoustic sources using a thin optical fiber and recording the resulting acoustic pressure wave with an intravascular ultrasound system [35]. Long acquisition times and the high abundance of blood in the vessels remain to be solved.

Efforts have furthermore been made to create optoacoustic endoscopes [36]. These, like catheters would allow for minimally invasive spectral imaging, even reaching the deep organs in humans.

As largely biological and preclinical systems, optoacoustic setups typically acquire structural and functional data from small animals [29]. Recent developments have however translated the modality closer to the bedside [37].

The following chapter compares optoacoustics to the already established imaging modalities.

Chapter 6

Existing modalities and Comparison to Optoacoustics

In this chapter, I will introduce existing biomedical imaging technologies and will compare them to the field of optoacoustics. The modalities will be compared in a multitude of characteristics, that include the acquisition cost, resolution performance, throughput and contrast. The most common clinical and biomedical imaging modalities are described below.

6.1 Ultrasound

Diagnostic sonography or ultrasonography, is an imaging technique based on the use of ultrasound (US), meaning sound waves with frequencies too high for humans to hear. For medical use, frequency bands between $1-10$MHz are typical [38]. Ultrasound images are formed by exciting an ultrasound transducer with a known electrical pulse, thus creating and sending an ultrasonic pulse into the tissue [39]. This pulse then gets reflected at the interfaces of different tissues and structures within the samples and the resulting echoes are collected by the transducer and used to form the image. US images can be made up of line scans, two-dimensional cross-sectional B-mode images and even three-dimensional images [40]. Functional data such as blood flow can also be imaged and tracked over time using the doppler effect [41]. US imaging is a real-time technique that is cheap to run and portable enough, to be operated at the patients' bedside. Due to the absence of ionising radiation, it is considered very safe. It's limited ability in imaging behind bone and air cavities is however a major drawback for some applications [42].

6.2 X-ray Computed Tomography

X-ray computed tomography (XCT) uses x-rays to produce cross-sectional images of the imaged sample. A largely anatomical modality, it creates images that map the radiodensity, meaning the x-ray attenuation of the investigated tissues [43], [38]. XCT uses ionising x-ray radiation to produce images and its use in medical practice should therefore be planned and controlled to reduce adverse effects [44]. In medical XCT, a source and detector gantry rotate about the patient and acquire projection images at different angles. The resulting reconstructed images then correspond to the density distribution within the tissue. XCT has excellent contrast between bone and soft tissue, it is however very difficult to distinguish between different kinds of soft tissues. The high penetration depth of x-rays makes XCT a highly valuable tool for whole body imaging in humans [42].

6.3 Single Photon Emission Tomography

Single photon emission tomography (SPECT) is a functional imaging modality with applications ranging from oncology to cardiology and neurology. It uses a gamma camera to acquire images at different projection angles and the resulting data is reconstructed to form images [45], [46]. The photons acquired by the cameras are emitted by contrast agents usually injected into the bloodstream of the patient, allowing SPECT to be used to image blood flow in the brain [47]. Its acquisition speed and resolution are however limited.

6.4 Positron Emission Tomography

Positron emission tomography (PET) is a functional imaging modality based on positron-emitting contrast agents. The most common contrast agent is fluorodeoxyglucose, an analogue of glucose that is metabolised in the body. The radioactive labelling is capable of highlighting tissues with increased metabolic activity. In PET, the tracer isotope decays by emitting a positron, which in turn annihilates together with an electron. This process emits to photons travelling in opposite directions. It's these photons that are then recorded using gamma cameras positioned around the patient [48] ,[49]. Like SPECT, the temporal and spatial resolution of PET are comparatively low, but the acquisition cost of a PET scanner can run as high as US$ 2.5 million [38].

6.5 Magnetic Resonance Imaging

Magnetic resonance imaging (MRI) can be used to image both, the anatomy and functional parameters of a patient. MRI is a non-ionising technique that can image whole volumes, but at a low temporal resolution, with each scan requiring minutes of acquisition time [38]. Typical clinical scanners operate above 1.5T and cost in access of US$ 1 million [38]. MRI scanners function by aligning the spins of protons in the patient's body along strong magnetic fields. Gradient fields are used to spatially encode the spins within the volume of interest and the spins' precession phases and frequencies are recorded by radio-frequency coils in order to reconstruct images [38], [50]. By varying the imaging parameters and sequences, the contrast between different tissue types and their functional parameters may be enhanced [51].

6.6 Optical Imaging

Optical imaging (OI) in a biomedical setting has applications ranging from clinical diagnosis to molecular biology. OI can be used to obtain both functional and anatomical data at high temporal and spatial resolution [52]. The main limitation of OI is its inferior penetration depth. Due to strong optical scattering, resolution degrades quickly as the light travels through tissue and signals acquired beyond a few millimetres in depth consist of diffuse light [53]. The optical contrast in *in vivo* settings is however strong and the signal-to-noise ratio in many other molecular imaging modalities does not match that of optical imaging [54].

6.7 Summary

The key characteristics of the different modalities described above have been summarised in Table 6.1 on page 21. Different modalities offer different benefits and drawbacks. While some applications might require the best performance in a single category, no modality combines as many advantages at once as optoacoustic imaging.

No ionising radiation is required in optoacoustics. Assuming safety standards are met, the illumination wavelengths are not able to cause any damage to the animals or patients. This holds true during the actual experiments, but also in studies that require long term imaging.

Many biological changes cause differences in the optical contrast. While planar optical imaging works great in identifying these differences, it is not

able to acquire the images at depth. Optoacoustics can image this optical contrast in deep tissues non-invasively.

Using multispectral optoacoustics and the spectral information of contrast agents, the method performs with molecular specificity. The resulting information can be used to perform biodistribution and pharmacokinetic studies non-invasively, see Chapter 8 for more details.

Like ultrasound sonography, optoacoustic imaging is scalable. Imaging systems can be build for different penetration depths and resolutions, depending on the application requirement.

Cost-effectiveness is becoming more and more important. Optoacoustic imaging setups do not require expensive liquid helium cooling like MRI and require much less physical space than MRI, PET or SPECT.

Using multi-element transducer arrays, volumetric real-time imaging has become a reality (Chapter 22). The short acquisition times are highly beneficial for *in vivo* experiments and result in volumetric data at unprecedented resolution of the optical contrast distribution.

Overall, these advantages make optoacoustics a valuable tool in a variety of biomedical applications and make for a rapidly developing field and create the scientific groundwork for this thesis.

Modality	Contrast	Sensitivity	Resolution	Cost	Safety	Throughput	Ease of use	Equipment size	Penetration depth
US	Poor	nmol(10^{-9})	$\sim 50\mu$m	Low	High	Medium	High	Small	Average
XCT	Average	μmol10^{-6}	$\sim 50\mu$m	High	Low	Low	Average	Very Large	High
SPECT	High	fmol(10^{-15})	1 cm	High	Low	Low	Low	Very Large	High
PET	High	fmol(10^{-15})	$3-5$mm	Very High	Low	Low	Low	Very Large	High
MRI	High	nmol(10^{-9})	$\sim 50\mu$m	Very High	High	Low	Average	Very Large	Large
OI	Average	pmol(10^{-12})	$1-2$mm	Low	High	Medium	High	Small	Poor
OA	**High**	**pmol(10^{-12})**	**$\sim 50\mu$m**	**Low**	**High**	**High**	**High**	**Small**	Average

Table 6.1: Comparison of imaging systems. Optoacoustic cases for best in category are highlighted with bold text. [42], [38]

Part III

Whole Head Imaging of Haemodynamic Responses in Mice

Chapter 7

Introduction

This part explains biomedical optoacoustic imaging in more detail. A study concerned with the functional imaging of a mouse model for stroke is used as an example. This part thus describes the technical details of a biomedical optoacoustic imaging setup, covering the necessary components for imaging as well as details about image reconstruction and physical difficulties and limitation of optoacoustic imaging.

7.1 Study Background

With 17 million people suffering a stroke each year, stroke is a leading cause of morbidity and mortality, leading to permanent disability in many of its survivors. While the survival rate has been increased for patients, stroke still results in permanent disability for a large portion of the survivors, with 40% of stroke patients requiring active rehabilitation [55]. Stroke has many subtypes, but its most prevalent form is ischaemic stroke, with 80% of clinical strokes being ischaemic [56]. Caregivers of stroke patients face the difficulty of dealing with the patients' impaired mobility, self-care and communication, as well as the patients' cognitive impairment, depression and personality changes [57]. The occurrence likelihood of a stroke can be influenced by several diseases and patient behaviours, with the most common, including smoking, high blood pressure, heart disease, diabetes, atherosclerosis and gradual cholesterol deposition causing a narrowing of the arteries in the neck or head [58]. Upon sufficient narrowing, blood clots may form, possibly occluding the blood supply. In ischaemic strokes, blood supply through the arteries to the brain is no longer sufficient or possible. This occlusion is usually caused by the formation of a blood clot, either

forming within a cerebral artery (thrombotic) or somewhere outside the brain (embolic) [58]. In the case of embolic strokes, the clot travels in the bloodstream and gets lodged in a cerebral artery, occluding it and restricting the blood flow. In the thrombotic case, both the formation of the clot and the site of occlusion belong to the cerebral vasculature network. The latter case is responsible for over 50% of all strokes [58]. While stroke is a disease of the brain, the effects of stroke can influence the functionality of the whole body. These effects can include, to different degrees of severity, paralysis, problems with thinking and speaking and emotional problems. Pain and numbness are further common outcomes [56].

Quick and immediate treatment is key in trying to increase the chances for recovery. Currently, only one treatment, tPA (tissue plasminogen activator), for stroke is approved by the FDA. Herein, tPA is administered through intravenous injection into the arm and works to dissolve the clot and recover and improve blood flow to and in the brain. If administered within between 3 and 4.5 hours after the occurrence of a stroke, tPA can help to improve the outcome of the disease. Other treatments, currently under development, include endovascular procedures to remove the clots [59].

In trying to reduce the incident rate of strokes, a carotid endarterectomy can be performed. This procedure entails the surgical removal of fatty tissue build up, known as plaque in the carotid arteries and is usually performed in older patients. The procedure was able to reduce the 2-year risk of stroke by more 80%, to less than 10% [58].

The last 25 years have shown great progress in understanding the disease, but research is far from being completed. It has been the objective of (pre-) clinical and small animal studies to further understand the development and formation of the ischaemic lesion, with non-invasive imaging being an essential tool in conducting the studies. Advances include the detection of ischaemic and infarcted tissue, as well as hypoperfused tissue, at the risk of becoming infarcted [60]. These new capabilities have increased the understanding of the pathology of stroke, thus creating a wealth of opportunities for possible treatments.

7.2 Why combine optoacoustics and stroke research?

As described above (see Chapter 6), the imaging modalities most commonly used to visualise and study stroke in clinical and preclinical settings typically have high acquisition and running costs and in some cases suffer from inferior specificity, low spatial and temporal resolution as well as low pene-

tration depth [61], [9], [62]. The need for the development of new therapies and treatments is however great and ever increasing. We therefore propose the use of multispectral optoacoustic tomography to study the disease progression of stroke in a mouse model. Optoacoustics can provide a low-cost and high throughput alternative to the established methods, thus potentially enabling groundbreaking and necessary research on a much larger scale. This study has been published in Kneipp et al. [63].

Chapter 8

Multispectral Optoacoustic Tomography

This chapter describes the optoacoustic setup, its components and gives details concerning image reconstruction and practical effects influencing imaging outcome, such as light penetration and contrast agents.

8.1 Imaging Setup

Multispectral optoacoustic tomography (MSOT) is an imaging modality based on the optoacoustic effect and has become a significant tool for *in vivo* biomedical research [64]. In MSOT, absorbers are excited using a wavelength tuneable light source, with optical parametric oscillator (OPO) technology providing high power illumination combined with the possibility of fast wavelength switching. Because the aim is to translate optoacoustic imaging to preclinical and clinical applications, the maximum exposure limits have to be accounted for [24].

Optical absorption is very high in biological samples in the visible range, MSOT therefore usually operates in the red or near-infrared (NIR) range [23]. Since the optoacoustic signal amplitude is proportional to the energy deposited in the tissue, lasers capable of exhausting the maximum permissible exposure limits are favourable. A setup comprising a Q-switched Nd:YAG laser is used in this application. The laser delivers laser pulses in the nanosecond range at $\lambda = 1064\,nm$. The pulses are then frequency doubled to $532\,nm$ and coupled into the OPO, which in turn is capable of working in the NIR tuning range. For spatial guidance of the illumination, the light is coupled into fiber bundles, that are used to direct the

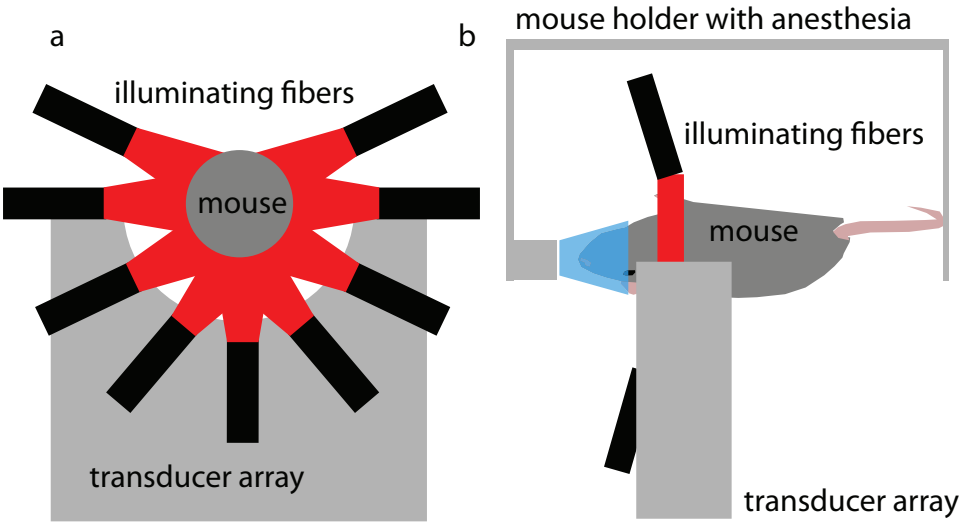

Figure 8.1: a: a 64-element transducer array acquires optoacoustic signals. Illumination is achieved using multimode fiber bundles. b: the mouse holder with integrated anaesthesia supply translates the mouse through the imaging plane.

light safely to the sample and illuminate it uniformly. A custom made 64-element transducer array (Imasonic, France) handles ultrasound detection. The transducer array covers a solid angle of 172° around the imaged sample, therefore acquiring a whole cross-sectional slice instantly. Each of the 64 elements is manufactured using piezocomposite technology, giving the elements a central frequency of around 5 MHz with a bandwidth of over 50% (when considering the -6dB drop-off) [64]. The arrangement of the transducer elements results in cylindrical-like focusing, achieving an in-plane resolution of around 150 μm.

Optoacoustic signals are generally considered weak [65]. It is therefore essential that the data acquisition system is characterised by an ultra-low noise floor and a sampling frequency high enough to satisfy the Nyquist-theorem regarding the maximal acquirable ultrasound frequencies.

The imaged sample is translated through the imaging plane using a stage-mounted mouse holder that is capable of supplying gas anaesthesia through a breathing mask, see Figure 8.1. The imaging chamber is filled with water to ensure ultrasonic coupling between the sample and the transducer array, with a thin film being used to protect the animal from direct contact with the coupling medium. Feedback controlled heating elements ensure that the

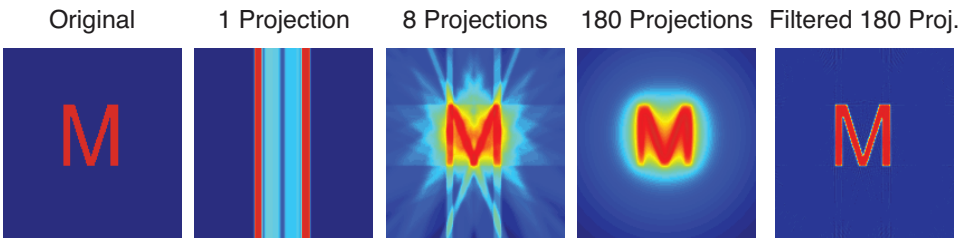

Figure 8.2: Reconstruction details improve with the number of projections. Filtered back projection recovers smearing of the objects, yielding an almost identical result to the original image.

animal's body temperature is stable and the speed of sound shifts due to temperature shifts are kept to a minimum.

8.2 Image Reconstruction

Optoacoustic signals are acquired using a multi-element detector array, drastically reducing acquisition time. Because multiple projections (64 in the 64-element array) covering 172° are acquired for every laser pulse, there is no need to rotate the sample or the transducer to produce a single slice. This improvement comes at the cost of image quality. Because the transducer array does not form a complete ring with 360° of coverage, limited view artefacts appear in the image reconstructions [42], [64], [66], [29]. Two methods for image reconstruction in optoacoustic experiments are presented below.

8.2.1 Back projection Image Reconstruction

Tomographic images may be reconstructed using a back projection algorithm [67], [68] (see Fig. 8.2). This method is computationally inexpensive and allows for fast real-time reconstruction at very high frame rates. In back projection, several assumptions are made to reconstruct the images. The time resolved optoacoustic signals are translated into signals along a straight line away from the transducer, where the time of flight of a signal amplitude is translated into distance from the transducer surface. By summing the signals onto a two-dimensional grid, the spatial distribution of absorbers may be found. A limited number of projections results in a non-uniform acoustic field that will cause smearing upon summing onto the grid. Filtering and weighting factors have been used in efforts to account

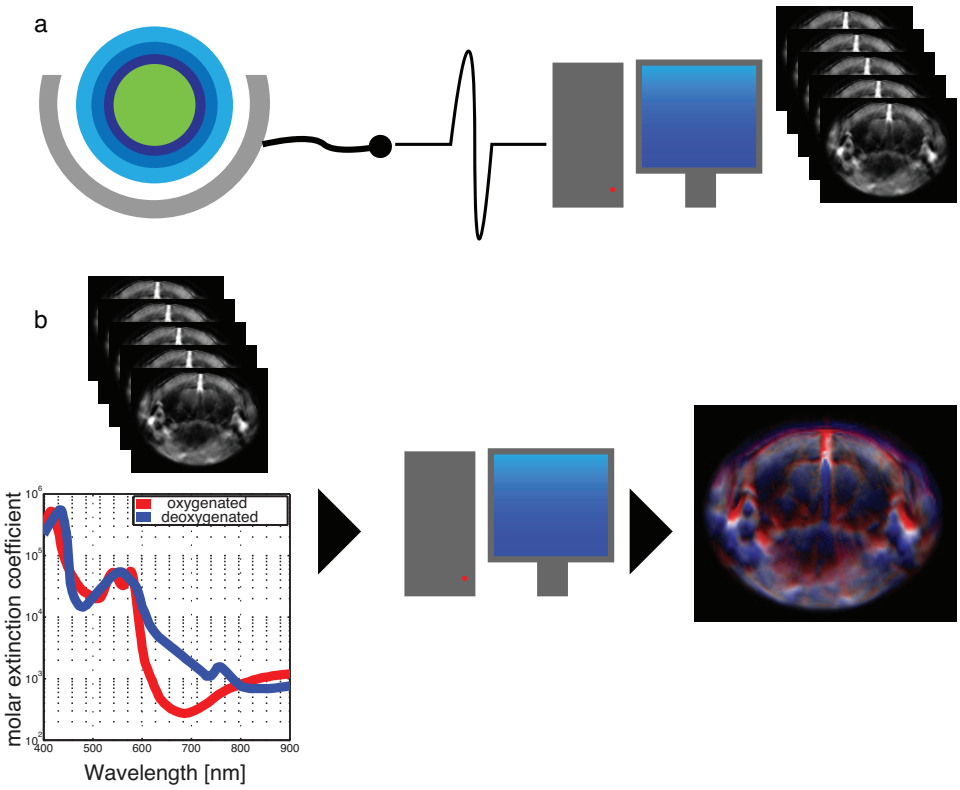

Figure 8.3: a: optoacoustic signals are acquired using a transducer array and the single wavelength images are reconstructed using a PC b: By combining the single wavelength images with spectral information of contrast agents, their distribution can be found with unmixing algorithms.

for the detection geometry of different signals [69], [68], the results however still remain inaccurate.

8.2.2 Model-based Image Reconstruction

In order to yield more accurate results, a model based reconstruction approach was developed by Rosenthal et al. [70]. This method is based on modelling the imaging system and inverting the resulting model matrix to calculate the image. This can be described as:

$$\vec{p} = M\vec{z}, \tag{8.1}$$

where $\vec{p}$ is a vector containing the measured signals, M is the model matrix describing the imaging system and signal propagation and $\vec{z}$ is a vector containing the image, thus the image can be reconstructed by inverting the model matrix. M is geometry specific and depends on the imaging grid, not on the imaged object. The image is formed by solving equation (8.1) for $\vec{z}$. The solution is found by minimising the square error of:

$$\vec{z}_{sol} = \arg\min_{z} \parallel \vec{p} - M\vec{z} \parallel \tag{8.2}$$

where $\vec{z}_{sol}$ is the solution image that minimises the square error. In most applications, the method of choice for minimising the error and solving the equation is the LSQR algorithm [71].

The main advantage of the model based approach is its adaptability to different imaging scenarios. It can include non-uniform and non-ideal characteristics, such as incomplete projection data [31]. These incomplete projection sets are the norm in real setups, as it is often a mechanical and technical requirement to include gaps in the transducer arrays for sample translation or to facilitate uniform illumination in the imaging plane.

Further adding to the benefits of the model based approach is the possibility to include the transducer shape in the reconstruction. While most reconstruction algorithms use idealised point detectors, including a more realistic finite-sized transducer surface can recover lateral resolution [72].

The method is however computationally very expensive and image reconstruction of data from a typical experiment using the model based approach takes multiple times longer than reconstruction using back projection. The computational time can be divided into two separate parts, the calculation of the model matrix and the iterative process of minimising the error of the reconstruction. Overall, the obvious benefits mentioned above outweigh the algorithm's drawback of being computationally expensive.

8.3 Spectral unmixing

In spectral unmixing, the goal is to convert the information contained in the acquired stack of images and produce new images that correspond to the distribution maps of single absorbers.

In linear unmixing, as illustrated in figure 8.3, the reconstructed stack of single wavelength images can be spectrally unmixed by combining the images with prior knowledge of the spectral behaviour of the contrast agents and absorbers. These contrast agents can be endogenous, like oxygenated

haemoglobin (HbO_2) and deoxygenated haemoglobin (Hb) (see Fig. 5.2a), or may be injected like indocyanine green, see Section 8.5 for details.

Spectral unmixing of the reconstructed images to find the spatial distribution of contrast agents, is done using a linear regression method [30]. The unmixing procedure is performed on a per-pixel basis by solving the linear set of equations:

$$\mu_a(\lambda_i) = \sum_{j=1}^{N} \epsilon_j(\lambda_i) c_j, \tag{8.3}$$

where λ_i is the illumination wavelength, ϵ_i is the wavelength-dependent molar extinction coefficient of a particular chromophore j at a local concentration c_j [73]. By solving equation (8.3) using the LSQR algorithm, a distribution map of the particular chromophore within the imaging plane is created. In order to produce reliable results, the stack of images has to be corrected for wavelength-dependent fluence and energy fluctuations of the excitation laser prior to unmixing. Furthermore, because of the wavelength-dependent absorption, not all wavelengths are able to penetrate equally deep into the tissue. This difference in penetration depth has to therefore be negligibly small or the analysis has to restricted to shallow regions under the skin, see Section 8.4 for more details.

Alternatively to using prior knowledge of the absorbers, blind unmixing can be used to separate the distribution of absorbers within a sample [74]. This method has its merits, because absorbers might change their absorption spectra, depending on the environment. A purified absorber is not required to retain the exact same absorption spectrum, when injected into a model organism. Furthermore, because the optoacoustic signature of an absorber depends not only on its absorption coefficient, but also on the wavelength-dependent fluence, blind unmixing can potentially yield realistic results of the absorber distribution.

Blind unmixing typically uses either principal component analysis (PCA) or independent component analysis (ICA) [74]. In PCA, components are separated using orthogonal transformations to create a dataset of linearly uncorrelated absorbers. In ICA, components are separated by assuming that they are statistically independent from each other.

In efforts to maximise the value of the image stack, single wavelength images at the isosbestic point of haemoglobin can be used to represent anatomical data, because they include equal contributions from both deoxygenated and oxygenated haemoglobin. By then overlaying unmixed distribution maps of Hb and HbO_2 over these anatomical images, individual

veins and arteries may be easily identified.

8.4 The Light Attenuation and Fluence Problem

The optoacoustic signal depends on the initial pressure distribution, which in turn is proportional to the absorbed energy. The local absorption properties, together with the available local fluence govern the amount of absorbed energy. In biological tissues, the fluence distribution varies and cannot be measured accurately and reliably. This inaccuracy poses problems concerning quantitative imaging experiments with multispectral optoacoustics. Overall, the fluence that an absorber sees is dependent on two things.

First, tuneable lasers do not have constant output energies. Rather their output energy is wavelength-dependent, also known as the tuning curve. Correcting for this wavelength dependence can be achieved in a very trivial manner. The tuning curve is either recorded before the measurement, or a sampling diode records the laser output fluctuations in real-time. The images are then corrected by normalising them with the corresponding diode or tuning curve value.

Second, light is attenuated as it propagates through tissue. The attenuation is caused by both scattering and absorption of light in biological tissue. This leads to optoacoustic images that generally exhibit a drop-off in fluence with tissue depth. Since the attenuation is wavelength-dependent, every single-wavelength acquisition suffers from a different attenuation map than the other acquisitions in a stack.

Correcting for this effect is not as simple as in the first case and poses a substantial problem for quantitative imaging. A possible approach for correction could be to invert non-linear models that model light propagation in tissue mimicking media. These are however computationally expensive and not suitable for real-time imaging. A robust correction method for this problem, combined with the quantitative nature of the reconstructions has yet to be found.

8.5 Optoacoustic Contrast in Biomedical Applications

Optoacoustic imaging creates spatial distribution maps of optical contrast. In biomedical applications, it maps the position of absorbers present in tissue samples. Overall, two main types of optoacoustic sources can be described for biological applications. The first consists of intrinsic contrast

agents that include haemoglobin and melanin. The second type, exogenous contrast agents includes indocyanine green and gold nanorods. The contrast agents will be explained below.

8.5.1 Intrinsic Optoacoustic Contrast

Blood is most likely the optoacoustic contrast agent with the highest importance. It is present in almost all types of tissues and therefore highly abundant throughout the body of humans and model organisms alike. Furthermore, it exhibits significant optoacoustic contrast. The absorbance of whole blood is largely governed by haemoglobin, which creates high contrast when comparing haemoglobin to the surrounding tissue [75]. This makes vascular imaging a highly interesting field for optoacoustic imaging and advances in the method have yielded promising first results, even in humans [32]. Haemoglobin is furthermore the main contrast agent used in the stroke study described below.

Haemoglobin is however also highly useful for functional optoacoustic imaging. As apparent from Figure 5.2a, deoxygenated and oxygenated haemoglobin exhibit different absorption spectra. Using unmixing algorithms (see Section 8.3), the spatial distribution of oxygenated and deoxygenated haemoglobin can thus be found and the oxygen saturation of the tissue can be estimated using:

$$S_{O_2} = \frac{HbO_2}{HbO_2 + Hb}, \tag{8.4}$$

where S_{O_2} is the oxygen saturation, HBO_2 is the concentration of oxygenated haemoglobin and Hb is the concentration of deoxygenated haemoglobin.

A second strong intrinsic source for optoacoustic is melanin. Melanin is a dark and thus highly absorbing biological pigment that is most abundant in the skin and hair. The strong absorption of melanin makes optoacoustic imaging a possible tool in studying the progression and possible treatments of melanomas [76]. An example of optoacoustic imaging with melanin as the main source of contrast is presented in Chapter 16.

Optoacoustic imaging has furthermore been proven to be applicable in imaging both water and lipid distributions [77], [35]. Specifically, water imaging was proposed for the imaging of tumours, as they exhibit increased water retention. Due to the high abundance of water in the healthy surrounding tissue, this method is limited regarding its achievable SNR. Optoacoustic imaging of lipids may become very important in vascular imaging, where atherosclerotic plaques are a sample of interest.

8.5.2 Exogenous Optoacoustic Contrast

A common property amongst most of the exogenous contrast agents used in optoacoustics is their absorption in the near-infrared part of the spectrum. This ensure detectability at greater tissue depths. The simplest application for such exogenous contrast agents would entail the constant monitoring of a region of interest at a single wavelength, preferably the peak absorbance of the contrast agent, over time. Upon injection of the agent, the signal would increase, thus capturing the kinetics of said agent.

In *in vivo* experiments, motion artefacts can severely change the position of the observed tissue or organ. This is especially apparent in long term studies that require imaging at several distinct time points, where the animal is removed from the system in between measurements, and thus it is not possible to perform simple single wavelength analysis anymore. In order for spectral unmixing to yield reliable results, the contrast agents should exhibit a characteristic absorbance spectrum, allowing for clear separation of the absorbers present in the imaged sample.

In an ideal case, the absorption spectrum is characterised by a narrow peak in near infrared range. This enables unmixing with a minimal number of wavelengths. Specifically, a minimum of two wavelengths could be theoretically sufficient for unmixing. If the sample is excited once at the peak absorbance of the contrast agent and once at a wavelength very close to the narrow peak, but much lower in absorbance, a simple difference image would then result in the distribution map of the contrast agent. This is possible, because the average background absorbance of biological tissue is considered relatively flat for small changes in wavelength. To the author's knowledge, such contrast agents do not exist, a typical multispectral image stack therefore usually includes more than two wavelengths.

One of the key deciding factors for choosing a contrast agent is the desired application. In small animal models, the possibilities are far greater than in clinical or preclinical settings. Specifically, indocyanine green (ICG) is approved for clinical imaging, gold nanorods are not.

Organic dyes have seen widespread applications in optoacoustic imaging [30], [64]. These dyes have been established in biological research and have mainly seen fluorescence applications. They therefore offer great possibilities in extending current biological research with the superior imaging capabilities of multispectral optoacoustics. Many of these dyes are commercially available and their absorption characteristics are well understood. Dyes exist for applications with a myriad of wavelengths, including the near-infrared range and are therefore well suited for optoacoustics.

Apart from organic dyes, nanoparticles have been applied in an increasing number of optoacoustic experiments [78]. Gold nanorods are particles that exhibit high optical absorption and therefore create strong optoacoustic signals. Their absorbance peak is situated in the near infrared and is tuneable through their longitudinal plasmon resonances.

A short overview of contrast agents can be seen in Table 8.1.

Agent name	Peak absorbance
Methylene blue	677 nm
Indocyanine green	810 nm
IRDye 800CW	774 nm
Gold nanoparticles	tuneable in near infrared
Carbon nanotubes	flat spectrum

Table 8.1: List of exogenous contrast agents.

Overall, contrast agents, both exogenous and intrinsic offer a wealth of opportunities for multispectral optoacoustics. It should be noted that contrast agents have to be chosen carefully for each application and that there is no single contrast agent suited best for optoacoustics. Limitations arise from a legal point of view, where not all agents are equally approved for biological, preclinical and clinical research, but also from specific limitations such as targeting, absorption characteristics, photostability etc. Contrast agents with sharply defined peaks are preferred, but the large tuneable range of current OPO technology increases the useable arsenal of agents.

Chapter 9

Experimental Outline

This chapter explains the required procedures to perform the *in vivo* study. It is split into two parts, explaining the stroke model as well as the imaging protocol used in this study.

9.1 Middle Cerebral Artery Occlusion Model

The majority of ischaemic strokes, around 80%, appear in the territory of the middle cerebral artery [79]. Therefore, the stroke model chosen for this experiment was the middle cerebral artery occlusion model (MCAO) [80]. MCAO is used to study experimental focal ischaemia after permanent or transient occlusion of the middle cerebral artery (MCA) and can be used in mice [79]. The clear benefit of using mice is that, because of the availability of transgenic and knockout strains, more comprehensive and complete studies can be performed.

Compared to other established methods, MCAO is technically easier to perform and less invasive as it does not require a craniotomy to achieve local occlusion of the MCA [81].

As described in Figure 9.1, a filament is used to limit the blood supply to a partial volume of the brain tissue. The animal is anaesthetised using 1.5% isoflurane (Penlon vaporiser, UK) vaporised in pure oxygen. Constant body temperature is ensured with a heating pad. When the animal is sufficiently subdued, the neck area is disinfected and a small incision is made at the neck of the animal and the left external and internal carotid arteries (ECA, ICA) are freed from the surrounding tissue. A filament is coated in silicone to reduce friction between the filament and the vessel walls and to increase its diameter enough in order to fully occlude the target artery. Sutures and

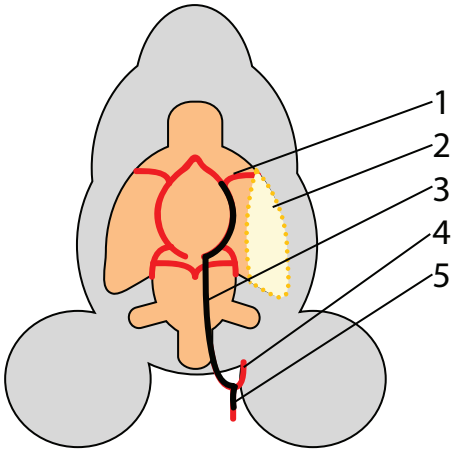

Figure 9.1: Middle cerebral artery occlusion: The filament (black) is forwarded into the MCA (1) through the ICA (3), starting at the bifurcation of the CCA (5) into the ECA (4) and ICA. This causes formation of the stroke volume (2).

vessel clips are used to inhibit bleeding upon opening of the artery. The coated filament is inserted into an incision made in the common carotid artery (CCA) and advanced into the ICA, until it reaches the origin of middle cerebral artery (MCA). It is then secured using a suture knot and left in place for 60 minutes. After 60 minutes of ischaemia, the procedure is reversed. The securing knot is loosened, the occlusion filament is extracted and the wound is closed. The animals are kept alive for the next 24 hours, after which the animals are sacrificed, with their brains being removed for slicing and imaging result validation.

9.2 Multispectral Optoacoustic Tomography Imaging

The optoacoustic data in this experiment is acquired using a cross-sectional MSOT scanner (see Chapter 8). The acquired multispectral data is subsequently reconstructed using a model-based reconstruction approach. This allows for accurate modelling of light and sound propagation and incorporates the detector geometry, thereby ensuring that highly accurate results for the functional blood parameters can be extracted from the acquired datasets. The spectral signatures of oxygenated and deoxygenated haemoglobin can

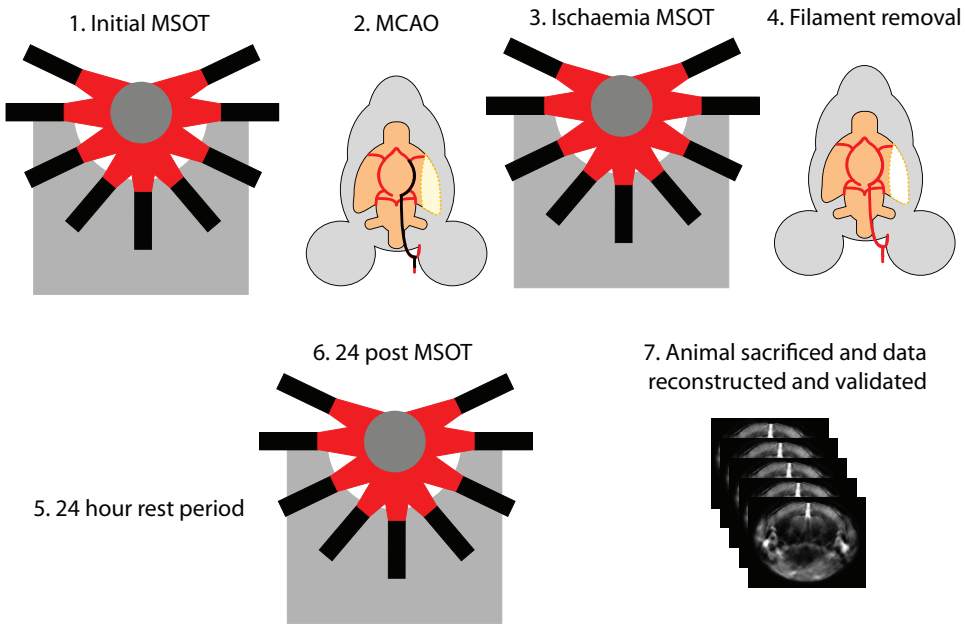

Figure 9.2: Experiment schedule for middle cerebral artery occlusion functional MSOT imaging.

be seen in Figure 5.2a and Figure 8.3b. By using the spectral information in combination with the acquired multispectral image stacks, spectral unmixing through linear regression results in distribution maps of oxygenated and deoxygenated haemoglobin (Figure 8.1).

The animals are scanned as follows (see Fig. 9.2). Every mouse in the study, the total amounting to seven mice, undergoes an initial multispectral scan in the MSOT system. This scan is used as an initial pre-ischaemia condition, thus creating a highly precise and individual base line for every mouse of the experiment cohort. The animals then undergo surgery (see Section 9.1) to create the stroke volume. While the filament is in place, the mouse is scanned again, yielding a dataset that contains functional haemodynamic characteristics during ischaemia. After 24 hours, the mice are scanned a final time, before being sacrificed. The brains of the animals are excised *post mortum* and frozen for sectioning at $-80°$ C. For validation of the stroke volume, the brains are sliced using a cryostat. Slices are 10 μm in thickness, with two copies being mounted on glass slides every 500 μm. The slices are then histochemically stained using H & E staining to analyse the stroke volume.

Chapter 10

Optoacoustic Visualisation of Stroke

This chapter presents the results of the optoacoustic imaging study of stroke. It is divided to represent two distinct parts of study. In the first part, the functional nature of optoacoustic imaging is presented through imaging of the blood oxygenation status of the the naïve mice, allowing for the differentiation of arteries and veins. The second part presents the imaging results following the occlusion procedure, more specifically, results during occlusion and 24 hours post ischaemia. Furthermore, it describes an analysis of the changes in the cerebral blood volume following occlusion.

10.1 Pre-Ischaemic Functional Imaging

Both a typical cross-sectional reconstruction and a stained cryosection can be seen in Figure 10.1. As blood is the main source of contrast in *in vivo* optoacoustic imaging, the major blood vessels are readily visible. Other discernible anatomical features include the dentate gyrus, the cortex and the midbrain reticular formation and are easily matched to the corresponding structures in the cryosection. The true value of the data becomes apparent when looking at the unmixed data. An overlay of the distribution maps of Hb and HbO_2 not only visualises the distribution of the two types of haemoglobin, but further adds functional information (Figure 10.2). By looking at the signals of different vessels, it is possible to distinguish arteries, such as the superficial temporal artery from its venous counterpart, the superficial temporal vein.

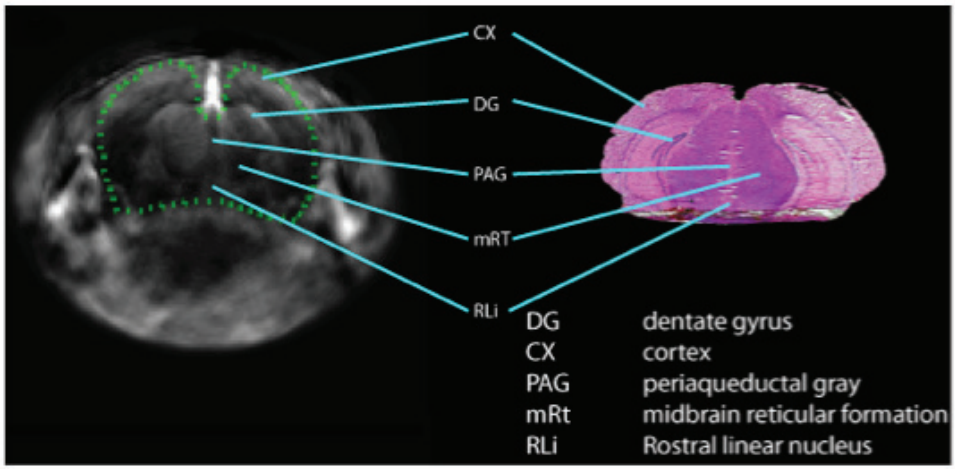

Figure 10.1: Whole-brain optoacoustic images of a mouse. Structural features visible in the cryosection (right) are matched with the corresponding optoacoustic image features (left). The representative stained cryosection shows the infarct area caused by 1h MCAO followed by 24h reperfusion. In the optoacoustic image, the area corresponding to the brain is enclosed by a green dotted line. The area affected by MCAO has been enclosed by a yellow dotted line.

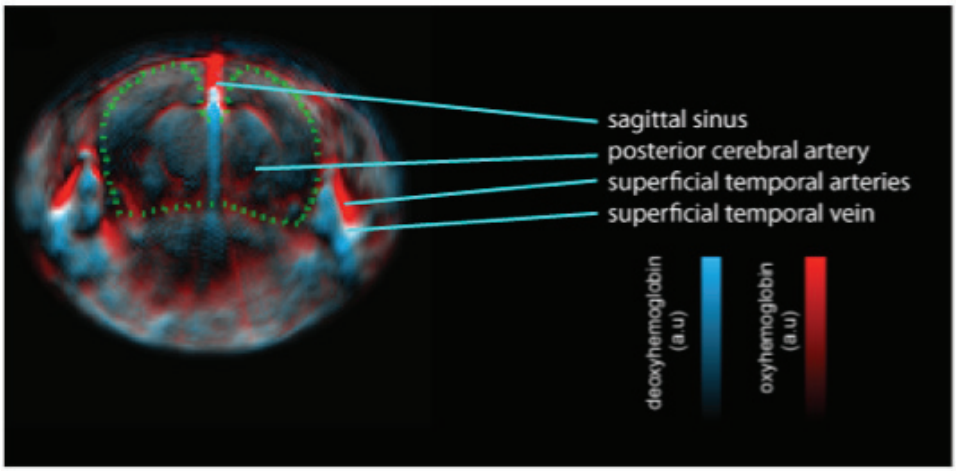

Figure 10.2: The multispectral data unmixed for the oxygenated and deoxygenated haemoglobin are overlaid on the single wavelength image from above (790 nm) in blue and red, respectively; the sagittal sinus is highly oxygenated due to the oxygen-isoflurane anaesthetic.

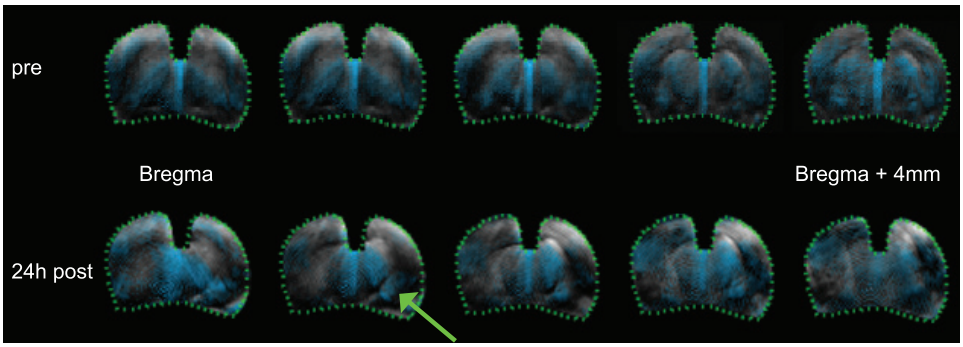

Figure 10.3: A coronal-slice set from a representative animal (distance between slices: 1 mm) with the multispectral unmixed data for deoxygenated haemoglobin in the brain presented in blue. The top row shows the pre ischaemia scan. The bottom row shows the data 24h post ischaemia of the same animal, with the Hb asymmetry marked by an arrow in one slice.

10.2 Ischaemic and Post-Ischaemic Functional Imaging

10.2.1 Whole Head Imaging

In analysing the scan data unmixed for Hb acquired at the time point of 24 hours post ischaemia, a clear asymmetry is visible (see Figure 10.3). The asymmetry is apparent throughout the whole brain and shows a distinct and finite core of strong Hb signal.

This increase of Hb however does not represent the necrotic ischaemic core of the stroke model. While the brain is reperfused after 60 minutes, the area adjacent to ischaemic core remains insufficiently perfused, creating an increased abundance of Hb at one side at 24 hours post ischaemia [82]. A similar asymmetry is visible during occlusion (see Figure 10.4). We propose that this area is part of the ischaemic penumbra [61]. The penumbra consists of tissue that is still considered viable but suffers from hypoperfusion. This area is therefore not completely destroyed, may however, depending on the progression dynamics of the stroke either recover or become part of the spreading necrotic core [83].

The necrotic core differs in both size and shape between different animals, with the extent and size of the Hb asymmetry exhibiting similar behaviour. More precisely, mouse A exhibits the largest stroke volume of approximately 58.5 mm^3, followed by mouse B (49 mm^3) and mouse C (48.5 mm^3), where

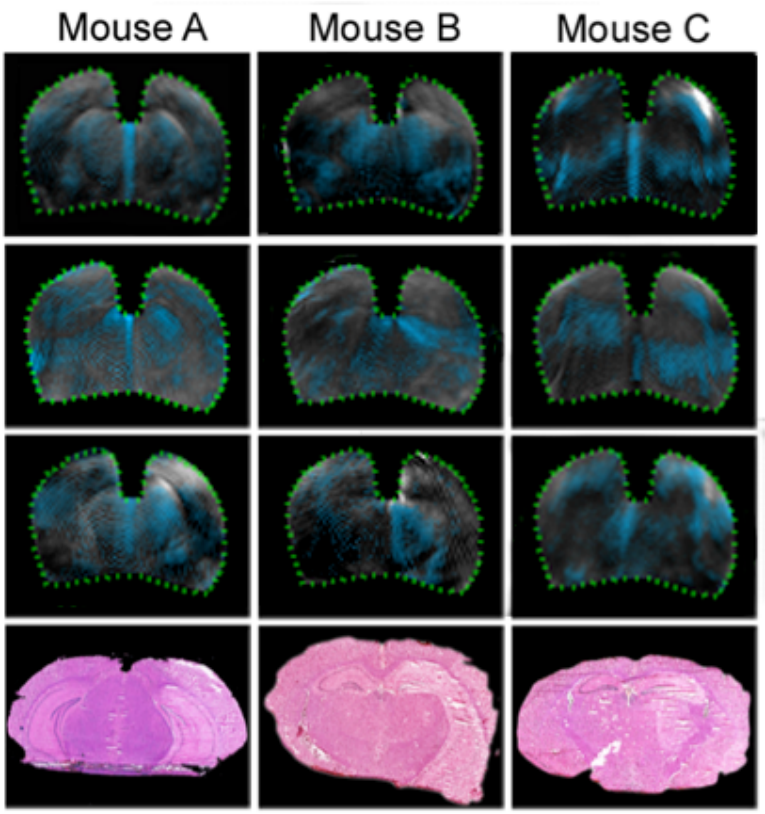

Figure 10.4: Deoxygenated haemoglobin distribution in several mice. From top down: Pre-, during, and 24 hours post-ischaemia MSOT images for three MCAO mice (left to right) with corresponding HE stained cryosections for each mouse (bottom; per mouse). MSOT: multispectral data for deoxygenated haemoglobin are presented in blue. Compared with the pre-ischaemia situation, images taken during and 24h post ischaemia show clear asymmetry in the vicinity of the infarcted regions, as also apparent in the corresponding histological sections.

the volumes are calculated from the stained histological slices. The volume size likely relates closely to the strength of the Hb asymmetry. It should be noted that some mice (mouse A and B in Fig. 10.4) seem to show very little or even no Hb signal in the cortex, even 24 hours after reperfusion. As the infarct core is characterised by no (or dramatically reduced) cell activity, oxygen consumption is significantly reduced. Thus the local haemoglobin supply is not deoxygenated, resulting in pseudo-normal or reduced Hb signal [83].

10.2.2 Cerebral Blood Volume Dynamics

In order to analyse the behaviour of the cerebral blood volume (CBV), ratios within the single wavelength data recorded at 790 nm are calculated. The illumination wavelength of 790 nm is very close to the isosbestic point of haemoglobin. Both Hb and HbO_2 therefore contribute equally to the acquired signals, thus directly relating the signal strength to total CBV. Comparisons are made by using ratios of the mean values of contralateral regions of interest selected in the cortex and in the striatum. Changes of the ratios are calculated as percentages relative to each pre-ischaemia value. The Friedman Repeated Measures Analysis of Variance on Ranks is performed to compare the absolute ratio data statistically. If a significant difference was detected, a Tukey Test (all pairwise multiple comparison procedures) is used as post hoc analysis; $p < 0.05$ was considered significant (see Figure 10.5).

It is apparent that during artery occlusion, the total CBV in the cortex is reduced (Fig. 10.5a), and all mice show a similar reduction in the ratio value. After 24 hours of recovery, the ratios have returned to near normal values. The overall trend is found by averaging the data for the seven mice. This shows that a significant difference exists between the ratios during and 24 hours post ischaemia (illustrated by an asterisks in Fig. 10.5). No such difference exists between the initial pre-ischaemia scan and 24 hours post-ischaemia.

The analysis of the striatum exhibits a different ratio behaviour, see Figure 10.5b. The ratios increase during artery occlusion for all mice and even remain elevated after 24 hours. The data averaged over all seven mice shows a significant difference between the ischaemic and post-ischaemic data set when compared to the initial pre-ischaemia data (Fig. 10.5).

Overall, the ratios between hemispheres demonstrate different longitudinal behaviour in different parts of the brain. The dropping ratios in the cortex are easily explained by the reduced CBV due to artery occlusion. The

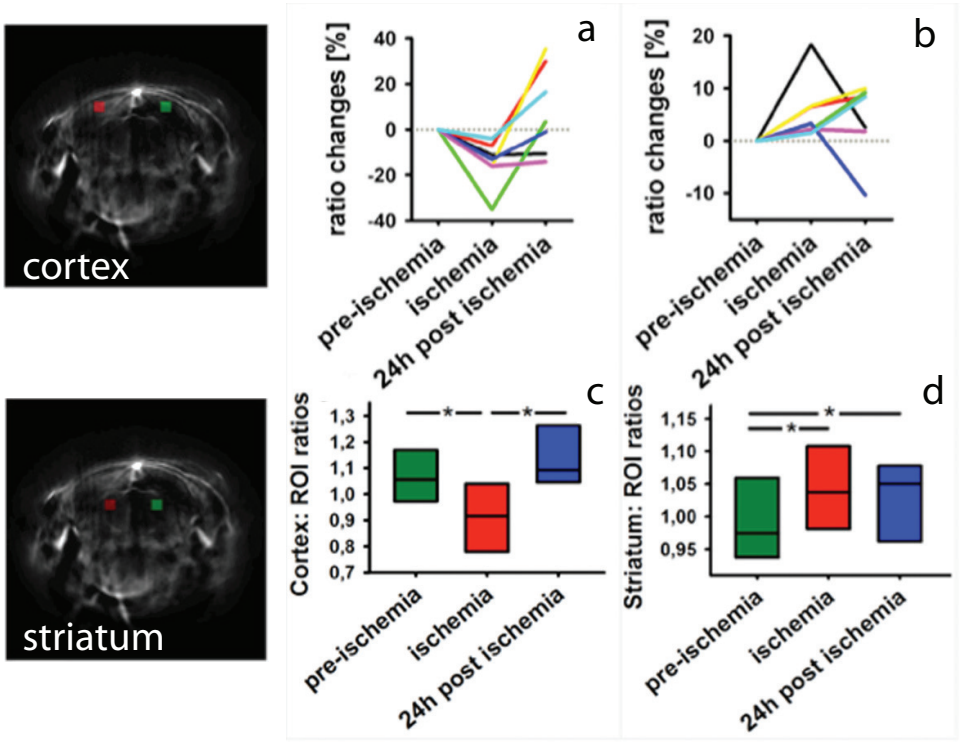

Figure 10.5: CBV ratio analysis for all the 7 imaged animals based on single wavelength optoacoustic images acquired at isosbestic wavelength of blood at 790nm. Ratios of the mean in the ischaemic cortex to the mean of its contralateral counterpart were calculated for the cortical areas (top left panel) and striatum areas (bottom left panel) and % changes relative to pre-ischaemia values are presented. a: All mice show reduction in CBV in the cortex, followed by return to normal values after reperfusion at 24h (middle). b: For the striatum areas, the mice show an increase of CBV during ischaemia, which remains elevated in most of the animals after reperfusion. Averaged data of absolute ratio values from all the mice (box plots with median and 25th and 75th percentile) are shown in panels c and d for the cortical and striatum areas, respectively.

increasing ratios in the striatum are however more difficult to explain. We propose the following explanation. The reduced blood flow in the penumbral region causes autoregulatory dilation of the local cerebral vasculature, thus leading to an increase in CBV [84]. If the blood flow is sufficient, the cells located in the hypoxic penumbra will be able to maintain their metabolism and survive the occlusion. In areas where the blood flow is not sufficient and the vessel dilation is not able to compensate the loss of flow, the cells will not be able to keep up their activity and the area will become part of the infarcted region.

Chapter 11

Summary and Conclusion

Investigation into potential treatments for stroke requires non-invasive imaging studies to track and validate findings. MSOT has proven to work as a non-invasive functional imaging technique for stroke.

While the ischaemic core could not be imaged directly, it was possible to visualise the penumbra in the animal model as a site of local hypoxia in the brain. This is promising for future studies to investigate potential treatments affecting the development of this hypoxic area and thus limiting the spread of the potentially dangerous necrotic core.

The intrinsic sensitivity of MSOT to functional blood parameters, combined with its strong spatio-temporal resolution make it a valuable tool for future studies. Clinical translation of current knowledge of stroke has been slow [56], largely owing to the complicated pathophysiology of stroke and its connection to what is known about regeneration and repair. Because of the characteristics explained above, MSOT should play a key part in these translational efforts.

However, it is clear that compared to other techniques, the presented data has not exhausted the full extent of possibilities, especially with regard to resolution. While the demonstrated resolution is enough to differentiate between different structures of the brain and to distinguish major vessels in the head and neck, it is not sufficient to visualise the fine cortical vasculature. For finer tracking of disease progression, high resolution data allowing for the real-time calculation and tracking of the penumbral volume would be immensely valuable.

Therefore, increasing the achievable spatial resolution in volumetric optoacoustic imaging is of high importance and will be able to further increase the value of the modality. Current micro CT and dedicated small animal

MRI scanners perform very well concerning high resolution imaging, but still exhibit the drawbacks of their larger scale cousins of high acquisition and running costs.

Combining the proven abilities to image endogenous contrast like the oxygenation status of haemoglobin and exogenous contrast agents like injected fluorescence indicators with increased spatial resolution promises valuable results.

Parts IV and V deal with increasing the spatial resolution in optoacoustic neuroimaging and describe two approaches to high resolution volumetric optoacoustics using higher frequency transducers. Part V furthermore includes the optoacoustic monitoring of fluorescent indicators, a promising way of going beyond the typical blood oxygenation dependent imaging scenarios (e.g. functional blood-oxygen-level-dependent or BOLD MRI) and directly image and track neural activity.

Part IV

Development of High-Resolution Deep Penetration Optoacoustic Brain Microscopy

Chapter 12

Introduction

Microscopes have been used for an extended period of time to image objects too small for the naked eye to resolve. To date, microscopes commonly use beams of light (or electrons in electron microscopy) that interact with the imaged sample. By collecting the result of this interaction, be it scattered light or fluorescence photons, microscopes enable studying small objects at high resolution. Technological advances have resulted in developments such as the confocal laser scanning microscope or multi-photon excitation microscopy, ever pushing the boundaries of what is achievable in terms of temporal and spatial resolution and depth penetration.

Optoacoustic Microscopy (OAM) uses the optoacoustic effect (Section 5.1) to create high resolution images. In optoacoustic microscopy, like in traditional bright field microscopy, samples are investigated using light. The signals that form the actual images are however ultrasonic in nature. It follows that optoacoustic microscopy can be categorised into two types of setups, namely optical resolution and acoustic resolution optoacoustic microscopy, see Figure 13.1. The dual nature of the method in terms of both excitation and detection and focusing, promises a wealth of possible applications.

The next chapters describe the two established approaches and the development of a third, new method to acquire high resolution optoacoustic data. Validation experiments are presented that cover imaging of agar phantoms, the analysis of the murine skull, as well as first *in vivo* results of zebrafish and mouse imaging experiments.

Chapter 13

Existing Types of Optoacoustic Microscopy Setups

This chapter describes current optoacoustic microscopes and explains their respective limitations, thus highlighting the need for the development of a novel approach presented in Chapter 14.

Optoacoustic microscopy operates in the $1 - 100$ MHz range, with the frequency spectrum of each measurement being dependent on the physical size and shape of the absorbers responsible for creating the optoacoustic signal. Smaller absorbers create higher frequency signals, meaning that as the imaged structures reduce in size (i.e. capillary structures, instead of larger vessels, like the sagittal sinus or the vena cava), the frequency spectrum of their respective optoacoustic signatures shifts to higher frequencies.

Generally, this relationship follows:

$$f_c \approx 0.8 \cdot c/d, \tag{13.1}$$

where f_c is the peak frequency of the optoacoustic spectrum, c is the speed of sound and d is the diameter of the sample.

OAM images are typically formed by scanning the sample. This can be achieved by scanning the incident beam of focused light [85], [86], or the transducer [87]. The transducer and data acquisition systems used in OAM record time resolved data for each position. By raster scanning in two dimensions, whole three-dimensional volumes are acquired. The different methods of creating and acquiring optoacoustic data in microscopy setups is described below.

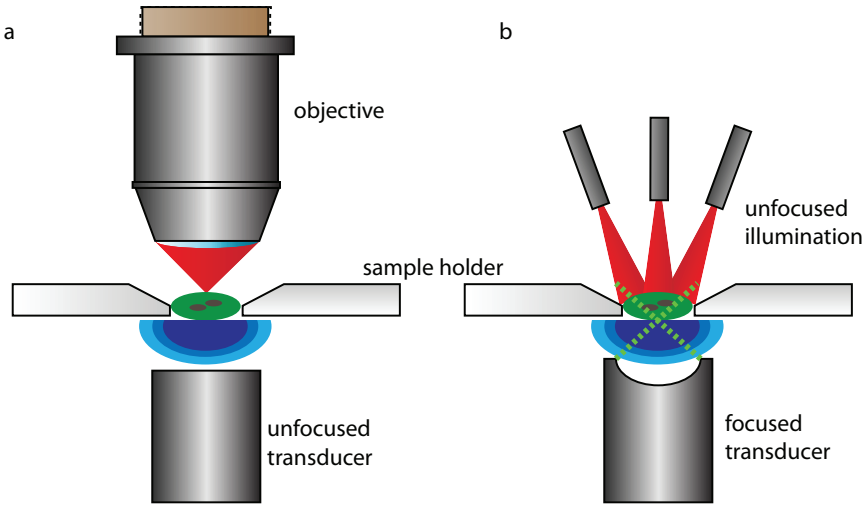

Figure 13.1: a: Optical resolution is achieved by tightly focusing the excitation beam (red) through a microscope objective. An unfocused high frequency ultrasound transducer records the optoacoustic wave (blue). b: the excitation beam (red) is delivered through unfocused fibers. Resolution is achieved through the focused ultrasound transducer.

13.1 Optical Resolution Optoacoustic Microscopy

In optical resolution optoacoustic microscopy (OR-OAM), resolution is achieved by focusing the excitation beam into the sample, see Figure 13.1a. This allows for diffraction limited focusing governed by [88]:

$$d = \frac{\lambda}{2n \sin \theta}, \tag{13.2}$$

where $n \sin \theta$ is known as the numerical aperture NA, λ is the wavelength of the observed light and θ is half the opening angle of the objective. The diffraction limit d is the achievable resolution, or the distance between two lines of a lattice, required for them to be resolvable using the microscope. In the case of a common $10X$ microscope objective with a NA of 0.25, in conjunction with light of a wavelength λ of 550 nm, we get:

$$d = \frac{550\,\text{nm}}{2 \cdot 0.25} = 1100\,\text{nm} \tag{13.3}$$

Potentially achieving a resolution of 1.1 μm is excellent, this superior resolution however comes at a price. OR-OAM suffers from the same limi-

tations as the established optical microscopy techniques. Photon scattering heavily limits the achievable resolution at depth. Here, the limit of the imaging depth is governed by the mean free path (MFP), which describes the distance that a photon travels between two consecutive scattering events [89]. In biological tissues, a scattering event is a process where a photon interacts with a cellular structure and in result changes its direction. While this direction change is usually in the forward direction, the large number of scattering events, even within a typical and comparatively small mouse organ results in a random walk of the photons. The MFP is given by [89]:

$$MFP = \frac{1}{\mu_t}, \tag{13.4}$$

with the transport coefficient $\mu_t = \mu_a + \mu_s$ being made up of the scattering coefficient μ_s and the absorption coefficient μ_a. For visible light, the MFP typically lies in the order of 100μm in tissues and results from the interaction of photons with cellular structures at these wavelengths. This means that blurring of the focused excitation beam occurs after the first 100 μm, when the bulk of photons has experienced at least one scattering event. This therefore limits the achievable resolution at depth.

13.2 Acoustic Resolution Optoacoustic Microscopy

In acoustic resolution optoacoustic microscopy (AR-OAM), resolution is achieved using focused ultrasound transducers (Fig. 13.1b) [87]. AR-OAM setups typically use spherically focused transducers with a high central frequency to achieve diffraction limited acoustic resolution. A typical transducer with a central frequency of 50 MHz can be used to achieve a lateral resolution of 45 μm and axial resolution of 15 μm at the focal zone [90]. In order to recover out of focus signals, virtual detector approaches have been used, producing promising three dimensional results [91]. A fast scanning coaxial AR-OAM system was introduced by Ma et al [87] to counteract the drawbacks of previous designs. Namely, owing to the difficult alignment of the illumination with the focal zone of the transducer, previous AR-OAM iterations had to sacrifice imaging speed for signal-to-noise ratio (SNR) by averaging shots at every imaging position. By aligning the illumination with the focal zone of the transducer through an aperture in the transducer's center, real-time imaging could be achieved. While this approach solved one big issue, AR-OAM still suffers from inferior resolution, when comparing it to optically focused methods.

Chapter 14

Hybrid Focus Real-time Optoacoustic Microscopy

As apparent in Sections 13.1 and 13.2, development concerning optoacoustic microscopy is not yet complete. While efforts to focus light through scattering media exist, for example using spatial light modulators [92], these approaches are usually slow and do not yet deliver the energy, time resolution and field of view needed for functional deep brain microscopy. Therefore, we developed a new approach that enables the combination of high optical focusing with the high penetration depth of acoustic focusing. This work has been partly published in Estrada et al. [34] and [93].

As illustrated in Figure 14.1, the approach uses a hybrid optical and acoustic focusing method to achieve the desired performance. The deciding factor for this approach is the optoacoustic head that enables coaxial alignment of the two foci. A special lens and fiber combination is inserted into the central aperture of the spherically focused transducer, thus aligning the foci.

A diode pumped Nd:YAG Q-swichted laser (IS8II-E, Edge-Wave GmbH, Würselen, Germany) is combined with a dye laser (Credo, Sirah Lasertechnik GmbH, Grevenbroich, Germany) as the illumination source. The setup provides pulses with a duration of 8 ns at a repetition frequency of up to 10 kHz. By using Pyrromethene 597 as the active agent in the dye laser, the illumination is tuneable between 575 and 605 nm. The light is subsequently coupled into a photonic crystal fiber (LMA20, NKT Photonics A/S, Birkerd, Denmark), with a gradient-index (GRIN) lens (Grintech GmbH, Jena, Germany) with a focal distance of approximately 6.5 mm attached to the fiber output.

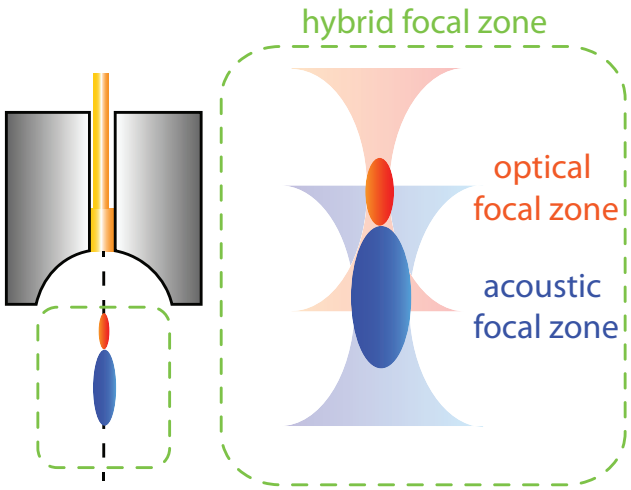

Figure 14.1: A fiber inserted into the transducer aperture enables coaxial alignment of the optical (orange-red) and acoustic (blue) focus. As the optical focus spreads within the tissue, the acoustic focus takes over.

This combination (see Figure 14.2) was chosen for several reasons. Photonic crystal fibers are single mode fibers, the light from their output is therefore focusable to a small spot. Unlike traditional single mode fibers however, they are able to transmit high amounts of energy. The flat surface of GRIN lenses simplifies handling at the small sizes required in this setup. Furthermore, the low NA of the GRIN lens allows for an extended focal zone with a Rayleigh length of $z_R = \pi\omega_0^2/\lambda = 2.2\,\text{mm}$, where λ is the wavelength of the light and $\omega_o = 20.3\,\mu\text{m}$ the beam waist of the Gaussian beam. In order to ensure proper alignment of the fiber output and the lens, the pair was securely mounted in a metal housing. The central bore of the transducer is however smaller than 0.9 mm in diameter, therefore requiring very precise manufacturing of the lens and lens housing.

The final part of the optoacoustic head consists of the ultrasound transducer. An ultrawideband spherically-focused Polyvinylidene Fluoride (PVdF) ultrasound transducer (Precision Acoustics, Dorchester, United Kingdom) is used (see Figure 17.2d for a typical frequency response). It has an active diameter of 6 mm and a focal length of 7.4 mm.

The optoacoustic head is mounted on motorised stages for scanning. By mounting the head on a fast linear piezoelectric stage (M683, Physik Instrumente GmbH, Karlsruhe, Germany), a frame rate of 18 frames per second is achieved for 3mm B-scans. To facilitate lateral scanning in two dimensions,

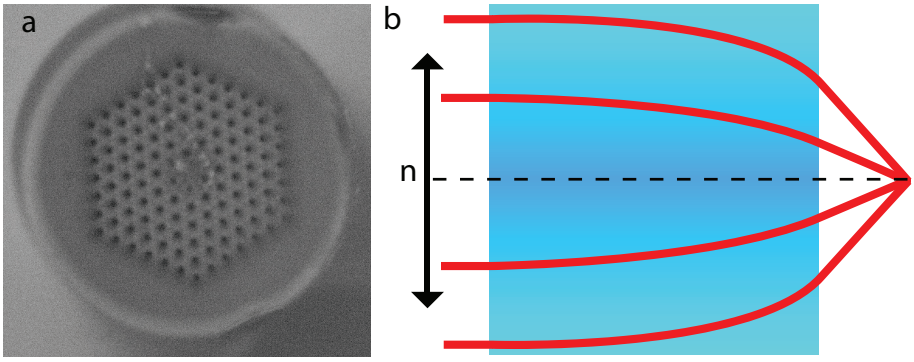

Figure 14.2: a: microscopy photograph of a 20 μm core photonic crystal fiber. b: The changing gradient index n of a GRIN lens focuses light

a second linear stage (LTM 60F, Owis GmbH, Staufen, Germany) translates the optoacoustic head in the second dimension. The combination of a fast piezoelectric stage and a slower linear stage has created two possible modes of acquiring three dimensional data (see Figure 14.3).

In raster scanning mode, a region of interest (ROI) is predefined by setting the lateral ranges and the step size. The stages then move the optoacoustic head from position to position, halting at every position until the A-line data is acquired (blue arrows in Figure 14.3). This has the advantage that it allows for the averaging of multiple shots at every grid position, greatly enhancing the achievable SNR. Because continuous acceleration and deceleration of the stages is very time consuming, this method of scanning is slow and is used only for non-dynamic and *ex vivo* studies.

In continuous mode, the movement of the stages is initiated once and shots are acquired on the fly (green line in Figure 14.3). This has the great advantage of resulting in much shorter acquisition times, in the range of several seconds for a whole volume, but lacks the ability of signal averaging. In order to achieve near uniform shot distribution throughout the ROI, the stage motion has to be calibrated. This is done by tracking the piezo stage motion with a laser distance sensor. When the range of motion and the speed of the stage is chosen before a scan, the calibration is started. Herein, the stage moves back and forth over the predefined distance and its position data is read out from an internal sensor. This process is slow and cannot be done on the fly, requiring a new calibration for every new set of imaging parameters. The stage position data is then matched to the readout of the laser distance sensor, thus allowing for accurate predictions of the stage

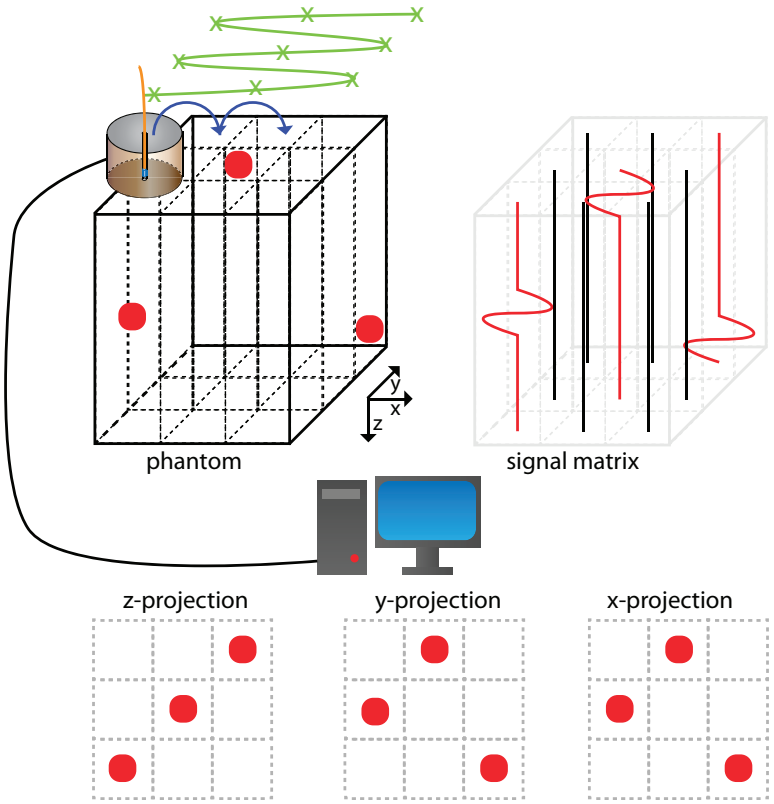

Figure 14.3: A phantom can be scanned in raster (blue arrows) or in continuous mode (green arrow). A PC stores individual shots into a signal matrix. Maximum amplitude projections are a way of displaying the acquired data (bottom row).

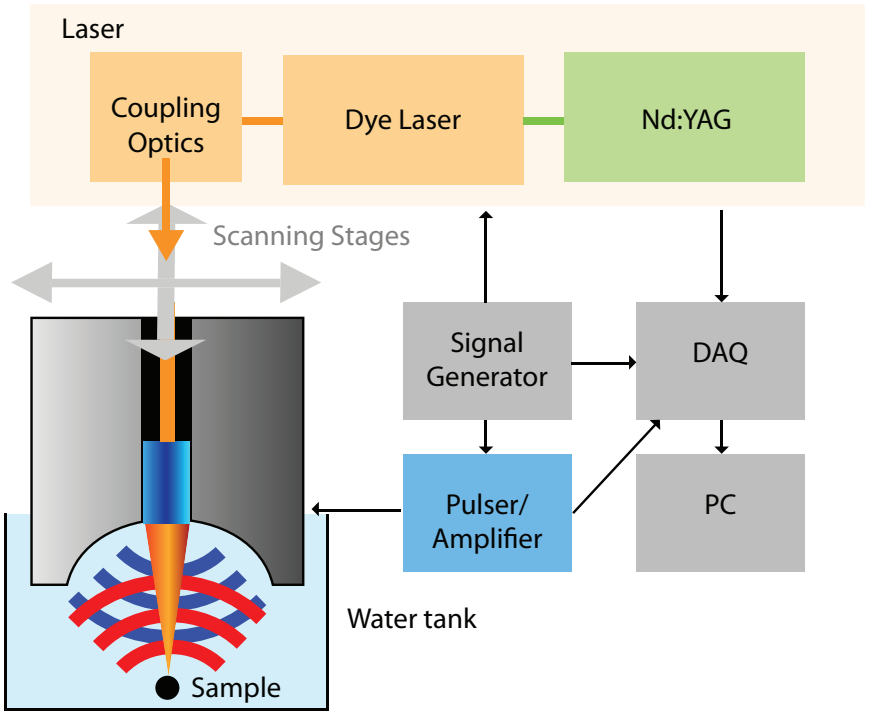

Figure 14.4: The sample is illuminated through a GRIN lens attached to a photonic crystal fiber. This emits ultrasound (red waves). In pulse-echo mode, the pulser excites the transducer to send out an ultrasound wave (blue wave), that will experience scattering and reflection in the imaging sample.

position from the laser distance sensor readout. By knowing the desired step size, as well as the stage speed, the repetition frequency of the trigger signal generator is calculated. During the scan, a shot is then acquired, every time the signal generator triggers a laser pulse, with the stages moving at a constant velocities.

One of the main advantages of PVdF transducers is their ability to be operated in both receive and pulsed mode. This means that the system is able to acquire both pure pulse-echo ultrasound data as well as optoacoustic data with the same transducer. To achieve this, the transducer is excited by pulses with a duration of 6 ns generated by an ultrasonic pulser and receiver (5073PR, Olympus, Japan) (Fig. 14.4)[93].

The ultrasound or optoacoustic data is then recorded using a data acquisition (DAQ) card (M3i.4142, Spectrum Systementwicklung Microelectronic GmbH, Grosshansdorf, Germany). The card is installed in a personal

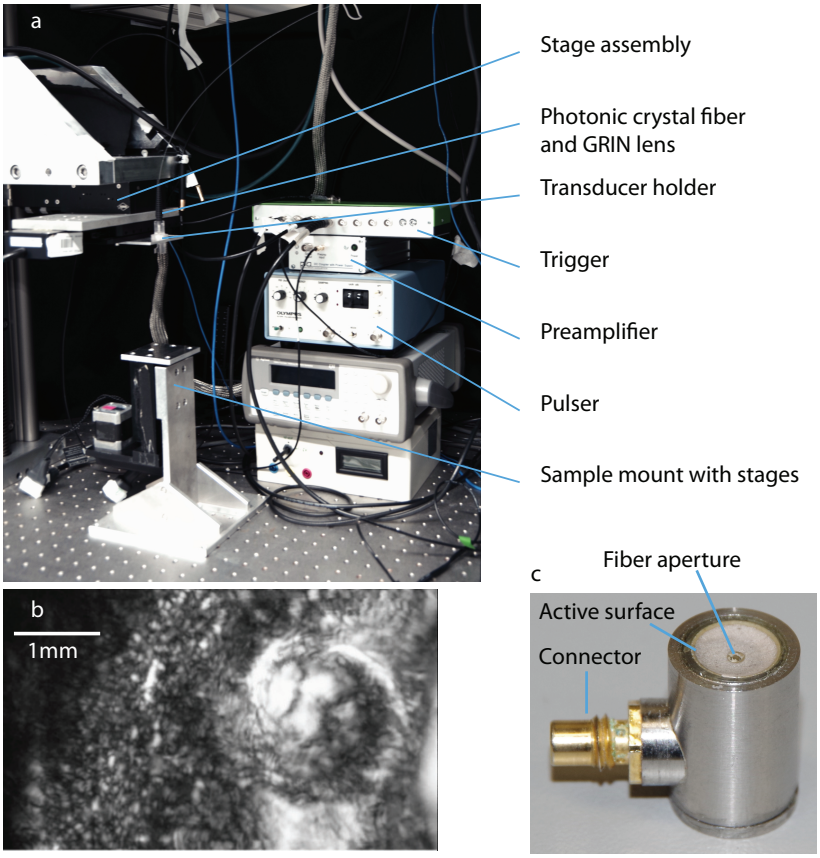

Figure 14.5: Photograph of the finished setup (a) with a closeup of the transducer (c). Example of an ultrasound image acquired of a skull with a thinned cortical window (b).

computer (PC), which is also responsible for data storage and control of measurement parameters, (see Fig. 14.5). Image reconstruction, as well as live previews are also handled by the same PC.

Chapter 15

Imaging of Agar Phantoms with Hybrid Focus Optoacoustic Microscopy

This chapter shows comparatively simple experiments used to characterise the system's imaging performance. The samples used are absorbers, sutures in the shown example, embedded in agarose (or agar). Unless otherwise stated, the agar was prepared by mixing 1.3% of agar (Sigma-Aldrich, USA) and distilled water. The mixture is then heated to the boiling point, after which the absorbers are moved into their desired position and shape and the agar is left to cool down. As the agar sets, it fixes the absorbers in the desired shape. Because of their similar speed of sound to water, agar phantoms can be used in optoacoustic imaging, without creating huge impedance mismatch artefacts. Furthermore, the simple preparation allows for the addition of scattering agents like Intralipid (Sigma-Aldrich, USA) or absorbing agents like ink to be added to the mixture, thus allowing for a wide range of possibilities to create scattering and even tissue mimicking phantoms using agar.

15.1 Optical Resolution Imaging

The result shown in Figure 15.1a consists of a small region of interest containing one 10 μm suture and is acquired using optical resolution mode. In this manner the effective system resolution is created through optical focusing. By using the focused illumination from the output of the GRIN lens in non-scattering samples or at the surface (below one mean free path) of

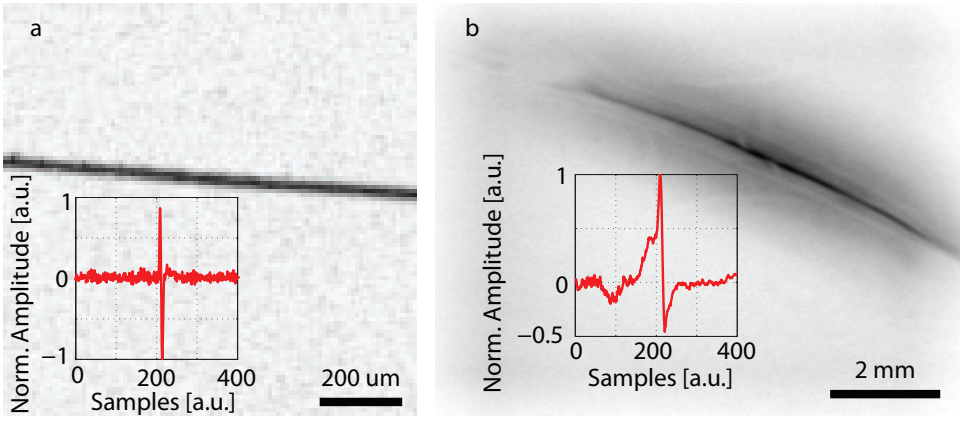

Figure 15.1: a: optical resolution optoacoustic microscopy of a 10 μm suture. An example shot is shown in the inset. b: acoustic resolution scan of a 50 μm suture. An example shot is shown in the inset.

scattering phantoms, the resulting lateral resolution will be created by the focused spot. The tightly focused spot is able to resolve small details and shows clear boundaries when imaging the thin suture.

15.2 Acoustic Resolution Imaging

Typical results from an acoustic resolution scan are seen in Figure 15.1b. To achieve acoustic resolution, unfocused illumination is used to ensure that only the focusing properties of the ultrasound transducer affect the system resolution. This can be achieved by illuminating the samples through multimode fibers or through a liquid light guide (Lumatec, Germany). The sample consists of a 50 μm suture embedded in highly scattering agar, to ensure uniform illumination. The acoustic focus is less tight, when compared to the optical focus. The boundaries of the larger suture are less defined, yet the suture is still clearly visible.

Chapter 16

Imaging of Zebrafish

Zebrafish have become a widely used model organism. Mutants have been created to study the embryonic development of vertebrates and many other applications in biological and preclinical research [94]. As fish, they are perfectly suited for optoacoustic imaging, as they can survive in the coupling medium water without the need for complicated breathing masks. This is especially true for zebrafish larvae that survive through perfusion and can even be restrained by being embedded in agar during *in vivo* experiments.

This section shows the results of zebrafish experiments using the optoacoustic microscope for imaging of larval stages through to adults. In the case of the larvae, a longitudinal study was performed that imaged the development and migration of melanophores over time. Zebrafish were chosen for imaging, because they enable first *in vivo* and *ex vivo* imaging of biological targets with greatly reduced difficulty compared to mammals. Their small size reduces the requirements for the size of the ROIs and thus the amount of resulting data. In the developmental stages, zebrafish are almost entirely transparent. Validation of imaging results by taking planar photographs is therefore much easier than in the case of the highly scattering tissue of mammals. This work has been published by Kneipp et al. [95].

16.1 *Ex vivo* Imaging of Zebrafish

In producing these results, the fish were sacrificed and embedded in agar. The agar was prepared using phosphate buffered saline (PBS) instead of distilled water. Distilled water would greatly speed up the cell degradation because of the huge saline concentration gradient between the cells and the surrounding agarose.

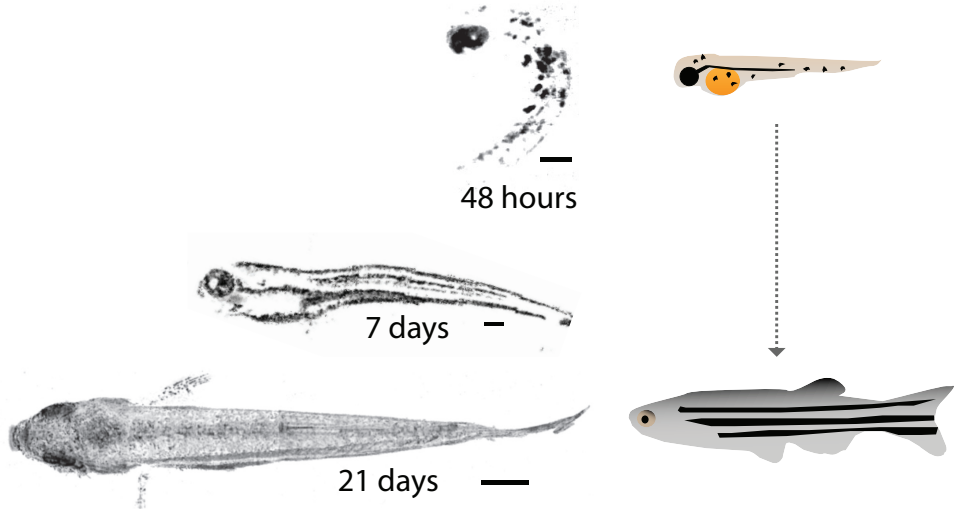

Figure 16.1: The optoacoustic microscope is capable of imaging zebrafish throughout all ages (left: OA images). In the larval stages, melanophores are the main source of contrast on the largely transparent fish. As the fish grow, the complexity of their shape and pigmentation increases. Scale bars are 200 μm for the 48 hour and 7 day fish and 1 mm for the 21 day old fish.

Figure 16.1 shows the results from imaging fish of different ages. The system was used to image larvae at the very young age of 48 hours post fertilisation (hpf). The fish are virtually transparent at this age, with the main source of contrast being the melanin contained in the melanophores that have spread across the body of the fish. The eyes are also strongly pigmented and therefore create excellent contrast for optoacoustics.

As the fish grow, the melanophores are no longer visible as blob-like structures, but have started to give the fish its characteristic striped pigmentation pattern. At 7 days post fertilisation (dpf), several stripes are visible along the body of the fish.

By 21 dpf, the zebrafish has reached its adult shape and pigmentation pattern. It will now only continue to increase in size, given the right conditions.

Optoacoustic microscopy is inherently three dimensional. This opens up new possibilities for structural imaging. As can be seen in Figure 16.2, features whose z-position is unknown from looking at planar photographs can be analysed in all three dimensions using optoacoustics. This is especially important in cases similar to Figure 16.2a. A stripe that appears to be made

up of melanophores at one depth in the photograph is actually, as revealed by optoacoustics, made up of three cells at different depths.

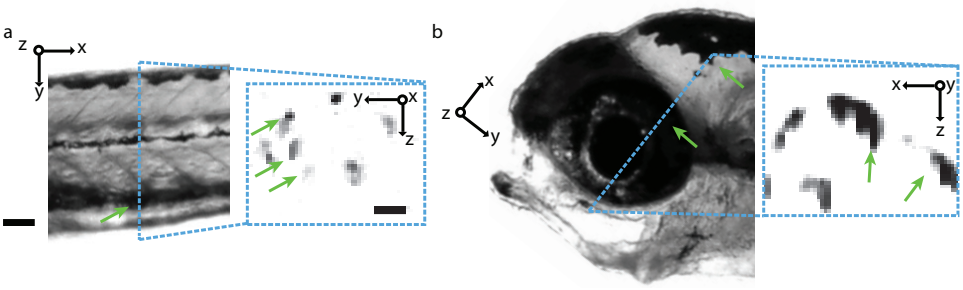

Figure 16.2: Optoacoustic datasets are three-dimensional. a: The green arrows mark melanophores that appear to be a stripe at one depth in the photograph. The optoacoustic slice reveals their different z-positions (blue box). b: The z-positions of the eye and the melanophores (arrows) are indistinguishable in the photograph. The optoacoustic slice reveals their relative position (blue box). Scale bar is 100 μm.

16.2 *In vivo* Imaging of Zebrafish

While *ex vivo* measurements are an elegant way of characterising a system and testing its abilities, the true value of an imaging modality lies in its possibility to excel in *in vivo* measurements. This means that the modality has to perform to the desired standards without being harmful. Potential damage can be caused by the excitation illumination, where just like in traditional forms of optical microscopy, high fluence can cause phototoxicity and photobleaching, potentially harming and killing cells [96].

After running a phototoxicity test series assessing the effects of focused illumination on melanocytes in young zebrafish, a longitudinal session was launched to image the development and migration of melanophores. The wild type larvae are embedded in agar made with fish water at 24 hpf and moved to the microscope setup. Imaging was performed once an hour for 11 hours, with a per pulse energy of 280 nJ.

As visible in Figure 16.3, the optoacoustic microscope is able to perform longitudinal imaging studies. In the shown time series, the eyes are the first to become pigmented and therefore the first to appear in the optoacoustic scans. Melanophores then originate in the head and trunk crest [97], after which they spread to cover the whole body (Fig. 16.3a). Individual body

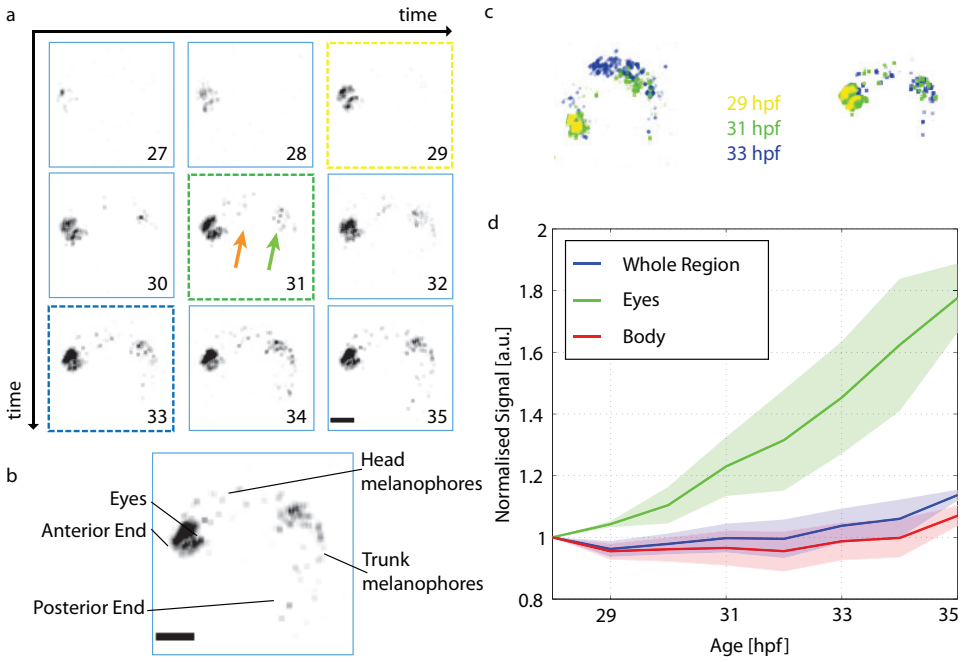

Figure 16.3: a: time lapse of developing zebrafish embryo, during melanophores formation and spreading. The time interval between each snapshot is one hour. The orange and green arrows mark the position of the head and trunk crest respectively. Scale bar is 200 μm. b: 35 hpf old fish. Different body regions and cells identifiable from the optoacoustic data are labeled. c: Colour-coded overlay for two different fish. The eyes are the first to express melanin (yellow). Signal then appears centralised around the putative region where head and trunk neural crest derived melanophores originate, with the eyes reaching full pigmentation (green). The melanophores likely spread outwards to eventually cover the whole body (blue). Time points are also marked in (a) with colour-coded dashed boxes. d: The mean optoacoustic signal of the fish increases over time. Different parts exhibit different dynamics. Standard mean error (n=3) is shaded.

parts are readily distinguishable in the scan data (Fig. 16.3b). Melanin is the main source of contrast in this study, an increase in the mean optoacoustic signal is therefore directly proportional to an increase in melanin present in the region of interest. A signal increase over time is apparent for several fish (n=3) in Figure 16.3c,d. As mentioned above, the eyes exhibit much steeper and earlier increase when compared to the rest of the body.

Chapter 17

Analysis of the Murine Skull

The murine skull is a strong hindrance in optoacoustic neuromicroscopy. This chapter describes the analysis of said skull using the hybrid focus optoacoustic microscope.

17.1 Background

Studies involving zebrafish are highly fascinating and are able to produce valuable insights, in order to understand and treat human diseases, other model organisms are however even better suited. It was shown in Part III that optoacoustics is able to image mammals, specifically mice. Mouse models are used to study a vast variety of human diseases [98]. As mammals, they are genetically and physiologically closer related to humans than zebrafish. For optoacoustic neuroimaging, they do pose a great challenge however. Mice posses a comparatively thick skull bone that is scattering and attenuating to both light and ultrasound and can therefore strongly influence the result of an optoacoustic measurement. This chapter aims to analyse the effects of the murine skull on optoacoustic imaging.

The work in this chapter has been published by Kneipp et al. [99].

17.2 Skull Phantoms

The proposed effects of the skull are illustrated in Figure 17.1. Signals from sources on or very close to the top surface of the skull will experience reflections at the skull-tissue interface. These will potentially mask the vasculature underneath the skull or even appear as shadow vasculature, where there is none. Furthermore, the skull effectively acts as a low-pass filter, meaning

that higher frequency signals experience stronger attenuation. Here, this is illustrated by the smaller sphere, creating higher frequency signals and therefore suffering stronger attenuation. In optical resolution mode, the optical scattering of the skull becomes apparent. When trying to focus light onto an absorber below the skull, the effective resolution is reduced through broadening of the focused beam by the scattering skull.

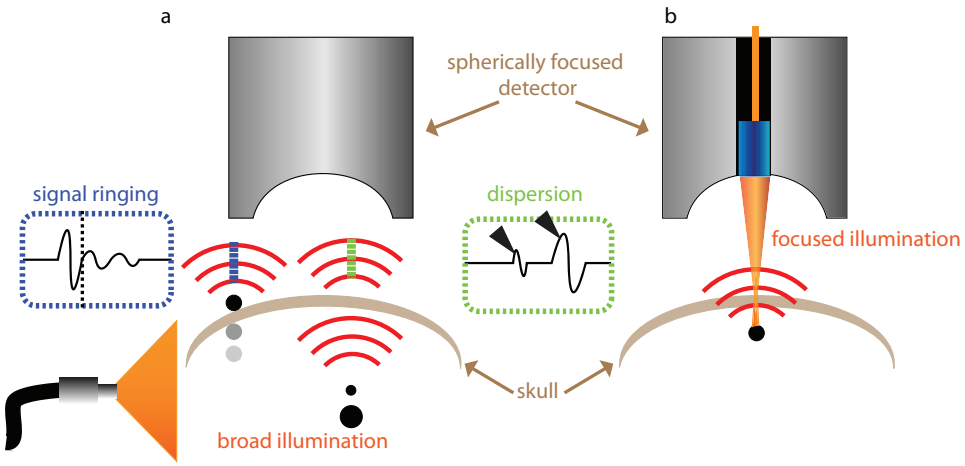

Figure 17.1: Schematics of the experimental approaches. (a) Acoustic resolution optoacoustic microscopy configuration using broad illumination. Optoacoustic sources located just above the skull generate ringing artefacts and shadow signals due to reverberation in the skull (vertical line in the blue box denotes temporal position of the skull). Frequency dependent attenuation leads to higher frequency signals (generated by smaller objects) experiencing stronger attenuation compared to lower frequency content (generated by larger objects), see green box. (b) Optical resolution optoacoustic microscopy configuration using focused light illumination. Focused light is scattered by the skull, broadening the excitation beam and affecting the lateral resolution performance.

In order to quantify these aspects, the signal of a 10 μm microsphere is compared with and without having to pass through an excised piece of murine skull. The microsphere is fixed in an agar phantom an illuminated broadly at a 90° angle, see Figure 17.1a. This step is taken to ensure no difference in fluence would affect the signal intensities whether the data is acquired through the piece of skull or not. The microsphere is moved into the focal plane of the transducer and two separate scans are acquired. One

without and one with a 230 μm thick piece of skull obstructing the direct view of the transducer.

Figure 17.2 shows the results of the skull and microsphere experiment. The frequency dependent insertion loss is calculated by dividing the with and without skull signal traces of the microsphere, by each other in the Fourier domain. Finite bodies support the existence of leaky guided waves, namely leaky Lamb and Scholte-Stoneley waves [100]. Because of these effects and the fact that the microsphere acts as an ultrasound point source, the transmitted waves experience both frequency and angle dependent filtering. Together with the finite detection angle of the spherically focused transducer, these factors explain the non-monotonic behaviour of the insertion loss (Fig. 17.2c).The insertion loss can be simulated using a homogenous plate model [101]. The insertion loss IL is approximated by:

$$IL(\omega) \approx \frac{\int_{\theta_1}^{\theta_2} T(k_0 \sin(\theta), \omega)\ \sin(\theta) d\theta}{\cos(\theta_1) - \cos(\theta_2)}, \tag{17.1}$$

where k_0 is the wavenumber in the fluid, ω is the angular frequency and T corresponds to the transmission coefficient of the plate model. A close correlation between the measured and simulated data can be achieved by using a density value of 1800 $\frac{\mathrm{kg}}{\mathrm{m}^3}$ [102], a speed of sound of 2900 $\frac{\mathrm{m}}{\mathrm{s}}$ and 1444 $\frac{\mathrm{m}}{\mathrm{s}}$ for longitudinal and shear waves respectively [103] and a thickness of 245.5 μm. Along with the general trend, the maximum transmission around 5 MHz and other peaks and troughs resulting from leaky lamb modes can be explained [100]. With increasing frequency, the relationship between prediction and measurement becomes largely qualitative, but remains in close relation above 25 MHz.

The FWHM of the Hilbert-transformed signals is 35 ns (53 μm) and 62 ns (93 μm) for the unattenuated and attenuated case, respectively. This is larger than expected for a 10 μm microsphere, it is however expected, as the axial resolution is governed by the acoustic focus of the transducer. Because of the low-pass filtering effects described above, the peak of the signal is boarder and lower in amplitude after it has been attenuated.

As a consequence of the above mentioned frequency and angle dependent filtering effects, the skull will introduce both time shifts and ringing artefacts in the measured signals. Specifically, it can be observed that the signal arrives earlier, when it travels through skull bone. This is because of the higher speed of sound of bone compared to that of water. A signal travelling through a combination of water and bone arrives earlier than a signal that covers the same distance just in water.

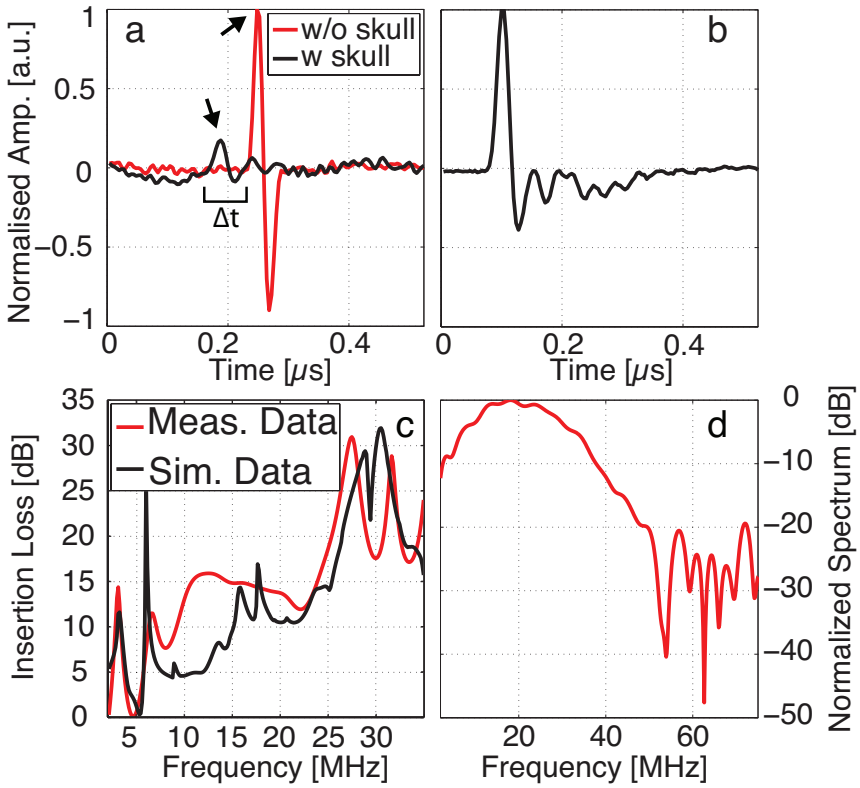

Figure 17.2: Results of the microsphere experiments demonstrate acoustic dispersion and ringing effects of adult murine skull. (a) Optoacoustic signal traces generated in the presence and absence of the skull. The attenuated peak is lower in amplitude and broader when compared to the non-attenuated peak (marked by arrows). The signal shift Δt is labeled. (b) Time domain signal of a microsphere placed in the immediate vicinity of the skull surface clearly shows signal ringing due to reflections at the skull-tissue interface. (c) Simulated (black) and measured (red) frequency dependent insertion loss of the skull showing a strong increase with frequency. (d) Normalised US frequency spectrum of the signal of a single 10 μm microsphere excited with a nanosecond laser pulse and measured with a ultrawideband PVdF transducer.

By using:

$$c_{sk} = \frac{c_w \cdot w}{w - c_w \cdot \triangle t}, \tag{17.2}$$

where w is the skull's thickness of 230 μm, c_w is the speed of sound in water and $\triangle t$ is the time shift of 72ns, we can calculate the speed of sound in skull c_{sk} to be 2828 $\frac{\text{m}}{\text{s}}$. This value is very close to the value range found in literature of 2800-2900 $\frac{\text{m}}{\text{s}}$ [104], [105].

An example of signal ringing can be seen in Figure 17.2b. The typical N-shaped signal is followed by reflections that potentially mask underlying absorbers.

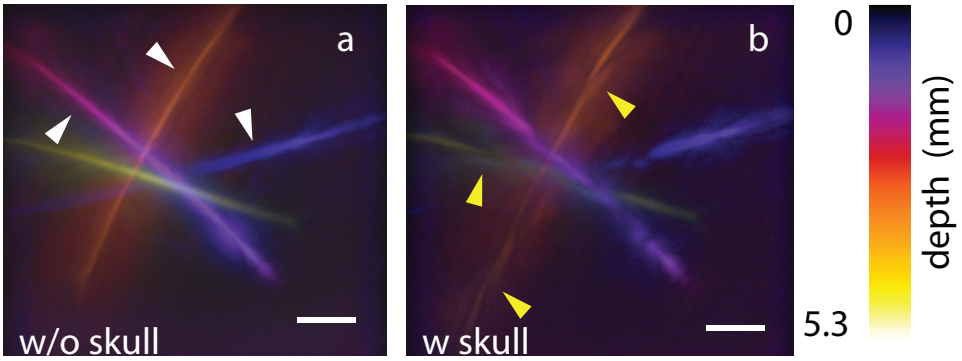

Figure 17.3: Effects of acoustic attenuation on imaging performance in the acoustic resolution mode. (a) Three-dimensional optoacoustic image (projection image colour-coded for depth) of four absorbing sutures randomly arranged inside tissue-mimicking scattering agar phantom. (b) The corresponding image acquired in the presence of skull. Scale bars correspond to 1.5 mm. Yellow arrows mark irregularities in the skull measurements. White arrows mark the position of FWHM measurements: 365 μm, 261 μm, 210 μm and 402 μm, 308 μm, 236 μm in (a) and (b) respectively.

While the signal analysis of 10 μm microspheres is highly useful for the technical characterisation of the skull and its effects, full volume effective imaging performance is just as important. In order to assess the acoustic resolution imaging performance with and without the skull, a phantom with several 50 μm sutures positioned in a scattering agar phantom at different depths is scanned. The agar is made to be highly scattering with 1% total intralipid concentration and illumination is delivered through a multimode fiber positioned underneath the phantom, again to ensure no difference in

fluence between the skull and no skull cases. The acoustic data was reconstructed using spatial impulse response weighted synthetic aperture focusing [106]. This algorithm is based on similar approaches in radar and ultrasound array technology, but caters to the special case of the optoacoustic microscope, that uses a single scanning detector. The algorithm is able to recover acoustic resolution outside of the focal zone of the transducer, resulting in a reconstructed volume with uniform resolution.

Figure 17.3 shows the result of the measurement. When introducing the skull, the FWHM increases only by 13% on average. This is in accordance with the results described above, as the sutures create spectra with a lower peak frequency than the smaller microspheres. Their signal therefore experiences less attenuation. The skull is irregular in shape and its multilayered make-up distort the acoustic signals. Such distortions can be seen in Figure 17.3b, where they are marked by yellow arrows.

17.3 Optoacoustic Imaging of the Perfused Mouse Brain

The ultimate goal of developing a system for biological and translational research is however not to image phantoms. Because *in vivo* imaging is highly prone to motion artefacts due to the beating heart and breathing, a method for creating stable but biological samples for optoacoustic imaging was developed. By imaging these samples, the system performance in biological samples can be assessed and optimised without the added difficulties of *in vivo* imaging and without creating unnecessary discomfort for any animals. Here the results are dominated by the optical resolution regime.

The procedure entails an adapted perfusion fixation technique [107]. Adult CD1 mice are sacrificed with an overdose of ketamine and xylazine, with 200 units of heparin being administered post delivery of the lethal dose of anaesthesia via intraperitoneal injection. The animal's chest cavity is opened and the animal is perfused through the left ventricle with heparinised PBS (5 units heparin per ml PBS). A second perfusion agent, prepared earlier, consisting of a 1:4 mixture of Pelikan 4001 ink (Pelikan Holding AG, Switzerland) to agar is used to perfuse the animal. The agar used in this case is prepared using 1.5% low gelling agar (SeaPrep, Lonza, Switzerland) in PBS. The animal is perfused with the second solution until all the blood and heparinised PBS has been replaced with the ink and agar mixture. The animal is then transferred into a 4° C fridge, where the agar is allowed to set for 45 minutes. This procedure allows for the complete re-

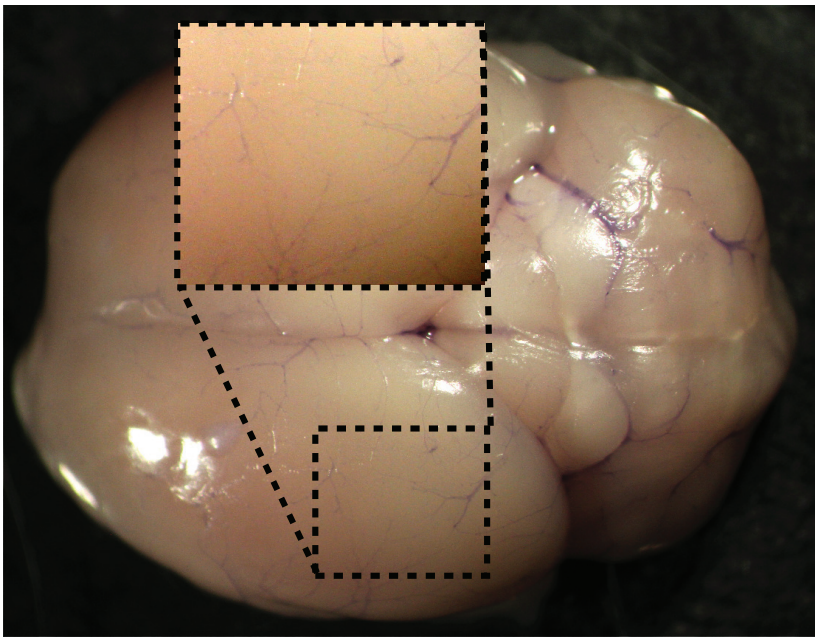

Figure 17.4: An excised brain perfused with agar and ink mixture.

placement of blood with highly absorbing ink, without disrupting the tissue integrity, see Figure 17.4. The agar acts as a stabilising medium for the fine vasculature and closely matches the speed of sound of both tissue and water, therefore minimising any adverse effects and reflections because of possible impedance mismatches. The method is adaptable for a myriad of different contrast agents that can be introduced into the second perfusion agent.

In order to accurately test the transcranial imaging performance in a biological setting, the head is removed from the body after the agar has set and the scalp is cut away. The skull is then prepared in the desired fashion. For this study, three different scenarios are prepared for comparison. The first consists of the skull being left completely intact, with only the scalp removed. This aims to minimise the effect of skull surface absorbers producing shadow signals through the ringing artefacts described above. The second scenario consists of a thinned skull preparation. Here the skull is thinned down using a high speed handheld drill (IDEAL Micro Drill, Cellpoint Scientific, USA). This is a common technique in many microscopy studies [108]. For the third scenario, the brain is exposed by removing the skull completely, resulting in an unobstructed view for the transducer and focused illumination of the perfused brain. The acquisition time was around

one minute for all three scenarios.

Maximum intensity projections are shown in Figure 17.5. Even through the intact skull (Fig. 17.5a), the cortical vasculature is readily visible. The finer capillary network is however hidden. The FWHM of the resolvable vessels decreases, when the skull is thinned (Fig. 17.5c). The finest vasculature is visible in the case of the completely removed skull (Fig. 17.5b). The FWHM goes down to as low as 21.8 μm with the cases of the thinned and intact skull producing higher FWHMs at 29.4 μm and 40.5 μm, respectively. As stated above, the results in this experiment are largely governed by the optical resolution. Here the reduction in effective resolution is largely due to the optical scattering in the skull, broadening the beam and therefore reducing the lateral resolution. By then low-pass filtering the created signals, the skull has further adverse effects on the optoacoustic signals. In some cases, the skull even completely masks the underlying vasculature, mainly due to strong absorbers still present in and on the bone tissue.

These strong attenuation effects make it clear that work towards direct optoacoustic imaging of neural activation cannot be done directly in mice, without first solving the issue of the skull. Until a method of choice for skull preparation, as well as possible combinations with correction algorithms have been found and validated, the validation and analysis of the performance characteristics of optoacoustic imaging of direct neural activation should be performed using a simpler model organism. In doing so, the next part (Part V) will describe an approach, where a volumetric optoacoustic scanner, with a lower central frequency than the microscope is used to image genetically encoded calcium indicators in zebrafish.

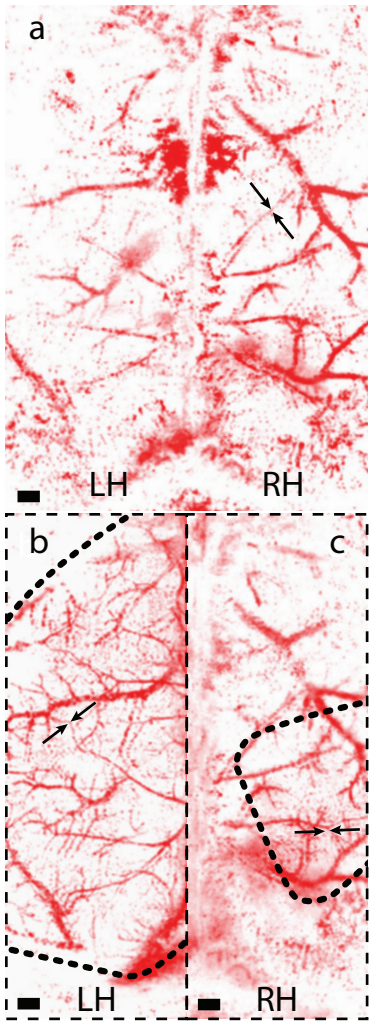

Figure 17.5: Murine skull affects the effective lateral resolution performance in optical resolution optoacoustic microscopy scans of biological targets. Maximum amplitude projections of optical resolution images of the perfused brain recorded through an intact skull (a), thinned skull (c) and without presence of the skull (b). Dashed lines mark the area where the skull was thinned (c) or removed (b). (b) and (c) each show one hemisphere (LH: left hemisphere, RH: right hemisphere) of the whole brain depicted in (a). Scale bars are 375 μm. Arrows mark the position of FWHM measurements, resulting in 40.5 μm, 21.8 μm and 29.4 μm for (a), (b) and (c) respectively.

Chapter 18

In vivo Imaging of a Mouse Ear

Biologically driven experiments typically require the ability to image samples *in vivo* non-invasively. In order to demonstrate these capabilities, the ear of an anaesthetised adult mouse was imaged non-invasively *in vivo*.

In doing so, the mouse is anaesthetised using a mixture of isoflurane and oxygen. When the mouse is sufficiently subdued, it is transferred to a stereotactic mouse holder to fix its position and reduce motion artefacts. A heating pad is used to ensure a constant physiological well-being of the mouse. Because the mouse cannot be easily submerged in water in *in vivo* experiments, coupling between the ear and the transducer is more difficult than for phantoms or fish. Therefore, the base of the imaging chamber is removed and replaced with a thin transparent film. This film is optically and acoustically transparent, but is strong enough to support the small column of water resting on it, without tearing. The chamber is then filled with water and the transducer is aligned with the region of interest. To further increase coupling between the ear and the film, a drop of water is placed on the ear and on the thin film prior to establishing physical contact between the two.

The result can be seen in Figure 18.1. The ear consists of highly vascularised tissue. Because of the high optical resolution in the hybrid focus optoacoustic microscope, vessels down to the capillary level are identifiable. Branching of larger vessels into finer vessels is readily visible, with the complex structure of the vasculature system becoming apparent. At 4.5 by 4.5 mm^2, the region of interest is sufficiently large to image a variety of organs, diseases and biological processes in the murine model organism.

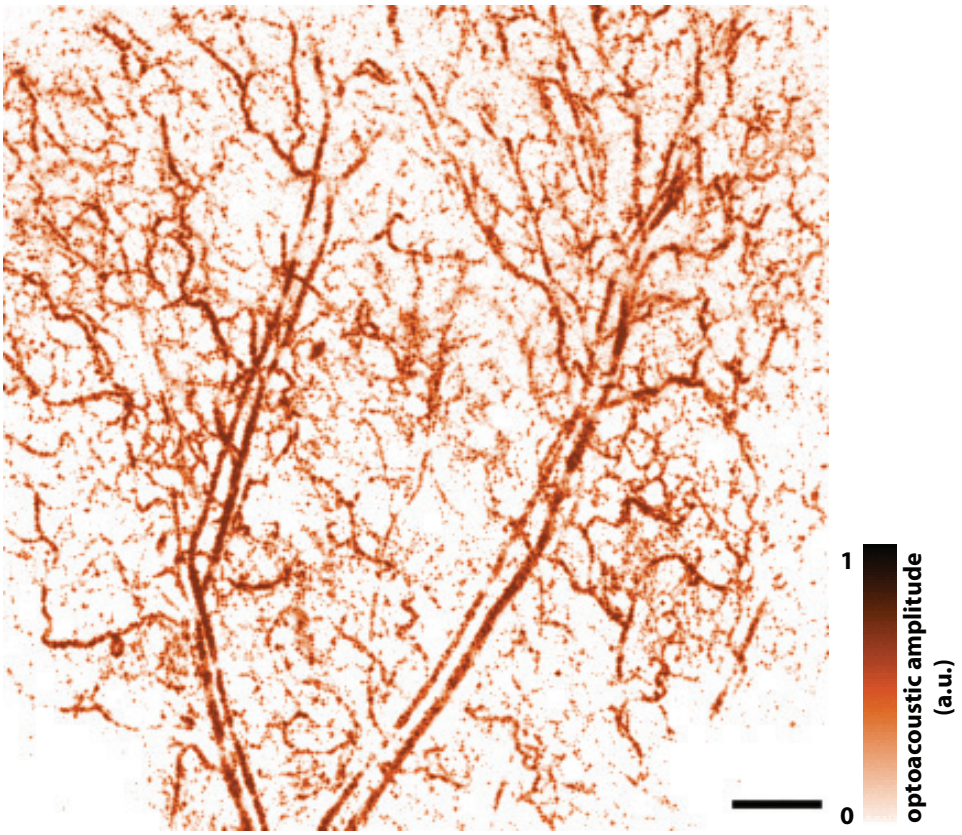

Figure 18.1: Projection image of an *in vivo* mouse ear. Larger vessels branch off into finer vasculature down to the capillary level. Scale bar is 500 μm

Chapter 19

Summary and Conclusion

A novel approach to optoacoustic microscopy was developed. The system uses hybrid focusing to combine the benefits of tight optical focusing with the superior penetration depth of acoustic focusing. The system can therefore excel in experiments, where systems based on optical focusing with high numerical aperture are not applicable because of their limited penetration depth. The coaxial alignment of the optical and acoustic axis and therefore their respective focal zones, allows for a seamless transition between optical resolution in the superficial layers of a sample and acoustic resolution in the deeper layers. While the high frame rate of up to 18 frames per second is already impressive, faster stages could further improve this figure.

The fusion between the fast scanning optoacoustic microscope and pulse-echo ultrasound biomicroscopy not only simplifies the focusing and alignment process, but enables the system to perform comparison studies and help in the development of multimodal contrast agents.

However, as shown in Chapter 17, the skull creates indisputable difficulties in optoacoustic imaging. By affecting both lateral and axial resolution in acoustic and optical resolution scenarios, the skull limits the achievable effective resolution in future non-invasive *in vivo* experiments. Optical scattering and frequency dependent acoustic attenuation shift the achievable spectrum peaks of measurements to the lower frequencies, thereby limiting the ability to image the high frequency signature of the fine capillary networks. The next part will therefore tackle direct optoacoustic imaging of neural activation using genetically encoded calcium indicators in fish. Their much thinner skulls have a reduced disruptive effect on the optoacoustic measurements.

Future developments of the system will include the realisation of dual

wavelength acquisition. At present, imaging is possible with either the pump laser at 532 nm or with the output of the dye laser (wavelength is dependent on the dye). Switching between the two requires changing the beam paths in the coupling optics in order for the 532 nm beam to bypass the dye laser cell, or for it to to be aligned into said cell. The coupling optics of the fiber further require optimisation following a wavelength switch. Pockel cells enable the fast switching between two wavelengths [109], adding yet another dimension (multispectral imaging) to the system.

In order to image deep within highly scattering and absorbing tissues like the brain, the number of incident photons has to be greatly increased. Focusing the required light intensities onto a small spot would create huge fluences, capable of cavitating and ablating tissues. In order to bypass this danger, a dual illumination setup is proposed, where a tightly focused spot is superimposed onto broad unfocused illumination.

In summary, the high spatial and temporal resolution together with the deep penetration into scattering tissue and the remaining expandability of the method are promising for the setup's future as a valuable tool in diagnostics, neuroimaging and cancer research.

Part V

Functional Optoacoustic Neurotomography of Neural Activation

Chapter 20

Introduction

In studying the single-cell physiology of neurones, it has been found that calcium is responsible for regulating cellular signalling events in many tissues and organisms [110]. These signalling events are known as action potentials in neurones and arise synchronically with rapid changes in intracellular calcium [111], specifically an influx of calcium ions through voltage-gated ion channels into the cell.

Neural activation is usually not a single, isolated event, but rather a systemic process, where different parts of an organism's nervous system react to a stimulus. *In vivo* and *in vitro* electrophysiology techniques have tried to track these events and their interconnections by monitoring neurones in varying degrees of separation [110]. The pattern of these processes reflect the interconnections and the relationships between the different parts of the nervous system. The interconnected parts communicate in neuronal subcircuits for information processing, decision making and governing general survival tasks. In attempts to study these networks proper, techniques to monitor whole populations had to be developed. To this end, synthetic calcium indicators have been used to measure action potentials in neural activation studies [112].

It follows that imaging techniques to volumetrically track neural activation with high spatial and temporal resolution deep within the brain would be key in understanding the fundamental processes of neural activation. Efforts of simulating the natural behaviour of neural networks has lead to technologies that allow for optical imaging of large, distributed neural populations [113], [114]. While advances have been made in imaging transparent organisms using single [115] and multi-photon [116] light-sheet and light-field microscopy [117], their inability of imaging scattering tissues

still limits the possible applications of the respective technology. This part therefore describes a method for imaging neural activation via genetically encoded calcium indicators using volumetric functional optoacoustic neurotomography.

The results presented in this chapter have been submitted for publication.

Chapter 21

Genetically Endcoded Calcium Indicators

21.1 Background

Most modern *in vivo* imaging studies of living brains rely on microscopy technology and fluorescent contrast labels [110]. Through bulk and intracellular loading, small molecules like fluorescent calcium indicators can be introduced into cells. These methods however do not allow for targeted imaging, as it is not possible to selectively load certain cell types, populations or cell organelles. Due to the aggressive and invasive nature of the technique, prolonged and repetitive loading is also not possible [118], [119]. Genetically encoded calcium indicators (GECIs) are an alternative to the synthetic indicators that facilitate targeted and longitudinal *in vivo* experiments [120]. Targeting of GECIs is not limited to cell types, but can be specified to range from populations of cells, over single cells to sub-cellular structures including dendrites or synapses [119]. Because delivery of the GECIs is at maximum minimally invasive (delivery either through transgenesis or viral constructs), they are compatible with long-term and repeated *in vivo* experiments [120].

These genetically encoded indicators are comprised of amino acids and consist of a calcium binding domain and at least one fluorescent protein. After being genetically expressed, they are formed spontaneously within cells. They further mainly localise in the desired location of the cytosol and do not leak from the expressing cell [120]. GECIs have the strong advantage that they allow for chronic, non invasive imaging of highly defined cells and cellular compartments [121].

Conceptually, GECIs can offer very high contrast between their bound and unbound states. In their resting states, the intracellular calcium concentration in neurones is extremely low [122]. Upon activation, voltage-gated calcium channels open and a rapid influx of calcium ions increases the local calcium concentration [119]. It is this strong difference between the resting and activated state that has the potential to illicit strong variations in suitable calcium indicators.

The actual performance of the indicators depends on a variety of variables. Their calcium affinity, brightness (governed by the extinction coefficient and the quantum yield), the pH sensitivity, folding stability and potential photobleaching all influence the acquirable signals [119].

21.2 GCaMP

State of the art GECIs include Förster resonance energy transfer indicators [123], but the GCaMP family of GECIs is one of the most prominent indicators in current research [111]. Efforts of improving the GCaMP family have increased its sensitivity both in culture and *in vivo* in worms, flies and mice [111]. *In vitro* experiments have been able to produce a fluorescence increase of 1200% upon calcium binding for GCaMP3 [111]. Using the GCaMP3 variant to track activity changes, large populations of neurones in the motor cortex, the barrel cortex and the hippocampus were studied in behaving mice [121]. Additional efforts have included probing light-evoked responses in the zebrafish tectum [124], *Drosophila* [125], and the mouse retina [126].

GCaMP5G is chosen for this study, as it exhibits strong absorption changes upon binding to calcium [121]. It was shown that GCaMP5G has superior calcium detection, exhibits a stronger response and has a greater dynamic range than the GCaMP3 variant [121]. Here, the GECI was genetically expressed in zebrafish. The specific zebrafish imaged in this experiment is the HuC:GCaMP5G strain, with both larvae and excised adult brains being the subject of the imaging study.

Figure 21.1 shows the absorption dependence of the chosen calcium indicator. The greatest absorption difference between the bound and unbound state, and therefore the greatest proposed difference in optoacoustic signal is around the second peak of shown spectrum. Imaging is therefore performed at 488 nm. A reference image was taken at 530 nm. This wavelength is characterised by low GCaMP absorption. From Figure 21.2, it follows, that the zebrafish clearly express GCaMP in their nervous system. The spine and

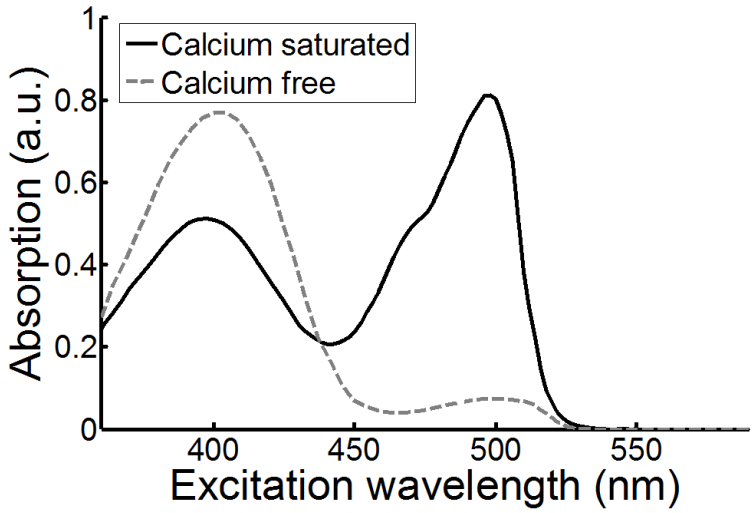

Figure 21.1: Spectral dependence of GCaMP5 absorption in bound and unbound states (reproduced from [121]).

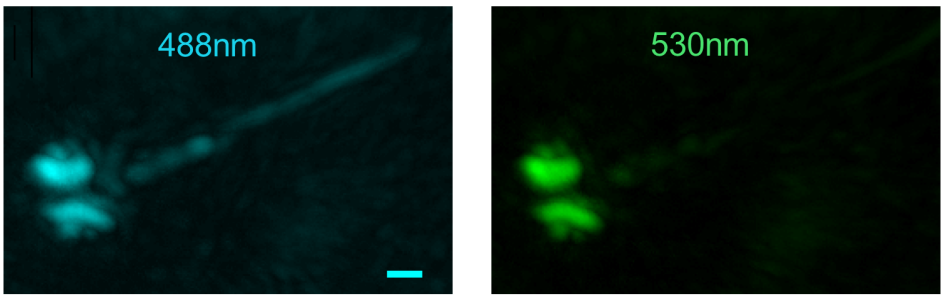

Figure 21.2: GCaMP is expressed in the spine and brain and clearly visible when excited at 488nm. At 530 nm, the minimal absorption of GCaMP limits the visible structures to the melanin expressing eyes. Scale bar is 250 μm.

brain are readily visible in the image acquired at 488 nm. At 530 nm, only the eyes are visible. Their signal is created by highly absorbing melanin.

Chapter 22

Functional Optoacoustic Neurotomography Setup

22.1 Motivation

Handheld and small animal optoacoustic scanners (see Part III) have been able to acquire two-dimensional cross-sectional images in real-time [33], but thus far suffer from several technological difficulties and drawbacks. Uniform illumination, especially in handheld systems is difficult to achieve. Inefficient illumination from the lateral sides of the transducer, together with limited angular coverage of the region of interest greatly restricts the achievable image quality. While steps have been taken to improve the image quality by using cylindrically focused transducer arrays, the acquired data is still only two-dimensional [127].

This limited dimensionality can be considered a major drawback, as two-dimensional data is not accurately representative of the physical phenomena it is trying to reproduce. Furthermore, the reconstruction algorithms used for the visualisation of two-dimensional data are based on simplifications to the three-dimensional optoacoustic wave propagation model and therefore create quantification errors in the reconstructed images [33].

In imaging neural activation in real-time without these quantification errors, a high frequency spherical transducer array is used to acquire the vast amounts of data, typical in three-dimensional tomography. The imaging system and its implementation is explained below.

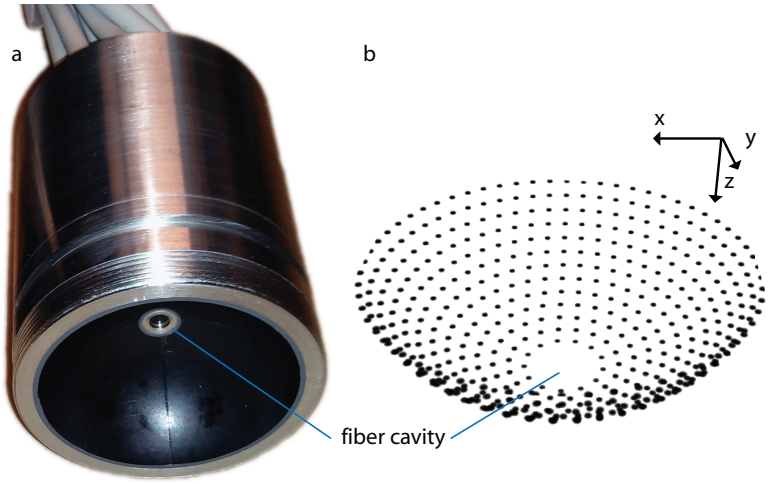

Figure 22.1: a: photograph of the handheld optoacoustic probe. b: element positions of the 512 elements in space. Samples are excited by inserting an illumination fiber bundle through the central cavity.

22.2 High Resolution Volumetric Optoacoustic Tomography

The volumetric optoacoustic tomography system used is adapted from the 256-element probe described by Deán-Ben et al. [32], [33]. The probe was designed to acquire real-time volumetric tomographic data at very high spatio-temporal resolutions, penetrating deep into tissue, far beyond the limits of current microscopes. The high resolution is achieved through the use of high frequency transducers. The spatial resolution in optoacoustic tomography systems scales with the bandwidth of the ultrasound transducers. The probe comprises a custom densely packed piezocomposite 512-element transducer array with an element size of approximately 6 mm^2. The central frequency of the elements is 10 MHz with a bandwidth of over 80%. In order to provide a tomographic view of the imaged sample, the elements are arranged on a spherical surface with a radius of 30 mm and an angle of coverage of approximately $1.3\pi \approx 140°$. The elements are oriented in such a way, that they maximise the angular coverage and therefore greatly limit the contributions of limited-view artefacts. The distribution of the transducer elements allows for a field of view of around 6 mm × 6 mm × 6 mm within the center of the sphere, see Figure 22.1. A cavity in the transducer surface allows for coaxial alignment of the illumination and detection during experiments.

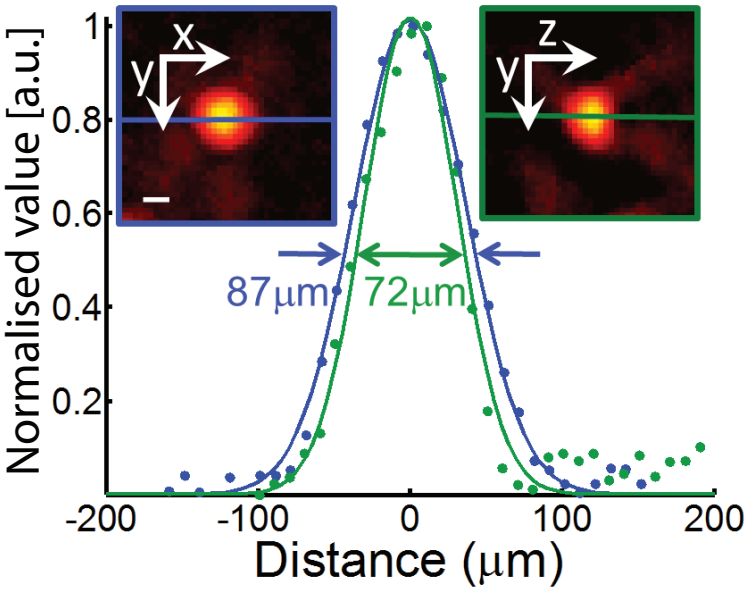

Figure 22.2: Considering the 50 μm size of the spheres, the resulting resolution lateral and axial resolution are 71 μm and 52 μm. Scale bars are 50 μm.

A parallel data acquisition platform, triggered by the output of the laser system, was custom developed to handle the simultaneous data acquisition of the 512 channels and data transfer to the host PC over a 1Gb Ethernet connection. The host PC is equipped with a high-end graphics processing unit (HD7900, AMD Radeon, USA) for real time data processing [33]. The reconstruction method for real-time visualisation is based on the back projection algorithm (see 8.2). Herein, the acquired signals are deconvolved with the transducer's impulse response, band-pass filtered and then finally reconstructed using back projection [33], see Subsection 8.2.1. The more accurate, but also more computationally expensive model based approach is used for analysis of the data in post-processing.

Samples are excited using a tuneable optical parametric oscillator laser (InnoLas Laser GmbH, Krailling, Germany). The beam is coupled into a custom made silica fused-end fiber bundle (CeramOptics GmbH, Bonn, Germany), designed to uniformly illuminate the sample with unfocused and broad illumination.

In order to characterise the spatial resolution of the volumetric imag-

ing system, three dimensional optoacoustic data of 50 μm microspheres is analysed. The microsphere is embedded in scattering agar, mimicking the scattering of biological tissue. By considering the actual size of the sphere, this analysis yields a resolution performance of 52 μm along the z-axis and 71 μm along the x- and y-axes.

The acquisition frame rate is limited by the laser's repetition frame rate of 100 Hz, wich was capable of delivering a fluence of 3 $\frac{\text{mJ}}{\text{cm}^2}$ to the sample at 488 nm. In order to compare the optoacoustic data to planar fluorescence images, a rapid high resolution sCMOS camera (pco.edge 4.2, PCO AG, Kelheim, Germany) is integrated into the setup and synchronised with the pulsed laser. Blinding of the camera is avoided by exciting the sample with side illumination. Figure 22.3 shows a sketch of the completed imaging setup. Although the system would be capable of imaging the samples in real-time multispectrally, the limited optical filtering capabilities of the camera limit the useable wavelength range. To further avoid blinding of the camera, only 488 nm illumination is used in the experiments.

In all experiments described here, the transducer array was filled with agar as to ensure acoustic coupling. A small mould in the center of the cup is made to facilitate exact placement of the samples.

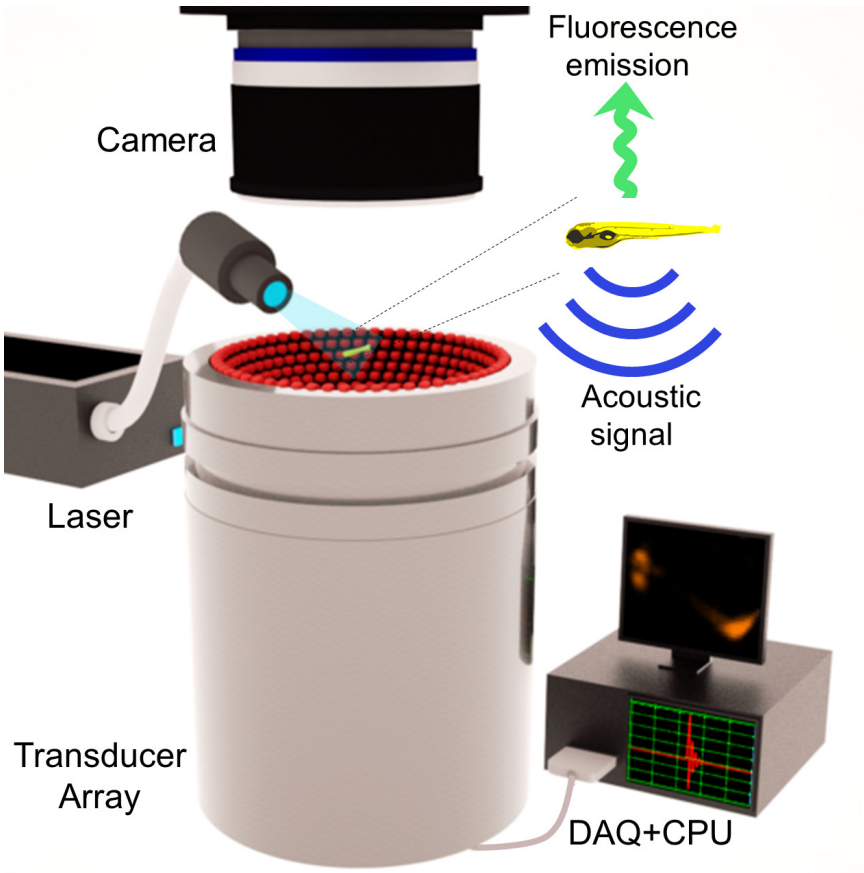

Figure 22.3: The imaged sample is placed in the vicinity of the geometrical center of a custom-made spherical ultrasound detection array. Light illumination of the entire object is provided via an optical fiber bundle. The generated optoacoustic signals are acquired by the array transducer while the induced fluorescence is simultaneously recorded by the high speed sCMOS camera.

Chapter 23

Optoacoustic Imaging of Neural activation

This chapter describes the experimental procedures and presents the results of the optoacoustic neurotomography study.

23.1 Experimental procedures

Two sets of stimulation experiments are run. With the two test subjects being *in vivo* zebrafish larvae and freshly excised and still activatable adult zebrafish brains. The breeding and maintenance of all fish is done under standard conditions [128]. All fish belong to the HuC:GCaMP5G strain, originating from the lab of Michael B. Orger and arrived as a kind gift of Hernán López-Schier. Embryos are raised in embryo medium at a constant temperature of 28°C with a standard light-dark-cycle.

Larvae experiments are conducted on freely swimming and immobilised 6-day old fish. The freely swimming fish are released into the above mentioned, fish water filled mould. The animals are given up to a minute to get used to their new surroundings before the stimulation procedure is initiated. Immobilisation of the second experimental group is achieved by placing the larvae in fish water containing 0.5% muscle relaxant (Gallamine triethiodide, Sigma-Aldrich). This step is to be performed before embedding the larvae in 0.5% low gelling agar, which is used to position the fish correctly in the field of view of the neurotomography setup. Stimulation is achieved by applying 50 mM Pentylenetetrazole (PTZ, [129]) using a syringe pump to deliver a volume of 100-200 μL at a flow rate of 5 μL, directly into the surrounding environment of the larvae. PTZ most likely interferes with GABAergic sig-

nalling to cause ictal-like spikes in the larvae's nervous system, also resulting in changes in their swimming behaviour [130].

Ex vivo brains are isolated from adult HuC:GCaMP5G fish at the age of 1.5 months. The fish are euthanised and the brains excised as described by Tomizawa et al. [131]. The excised brains are immediately submerged in artificial fish cerebral spinal fluid (aCSF: 100 mM NaCl, 2.46 mM KCL, 1mM $MgCl_2 \cdot 6H_2O$, 0.44 mM $NaH_2\,PO_4\,H_2$, 1.13 mM $CaCl_2 \cdot H_2O$, 5 mM $NaHCO_3$, pH 7.2, [132]). The brains are mounted in 0.5% low meting agar made with aCSF and positioned, as above, in the field of view of the transducer array. Application of PTZ follows the same procedure described above.

23.2 Optoacoustic Results

23.2.1 Optoacoustic Imaging of Immobilised Larvae

The exposure to the neuroactivating agent PTZ causes robust activation waves, characterised by transient changes of intracellular calcium concentration, spreading along the larvae's spinal cord. The wave travels from the posterior, the site of injection to the anterior of the larvae (see Fig. 23.1). Simultaneous coaxial acquisition of the planar fluorescence and three dimensional optoacoustic data allows for direct comparison of the respective signal traces. The fluorescence signal and the optoacoustic signal exhibit strong correlation at both, the tip and the midtail section ($R^2 = 0.98$ and $R^2 = 0.97$ respectively), see Figure 23.1b, c.

23.2.2 Optoacoustic Imaging of Excised Adult brains

As previously discussed, zebrafish larvae are ideal first test subjects, as they are virtually transparent, allowing for easy co-registration of optoacoustic and fluorescence data. They do however not demonstrate the three dimensionality of optoacoustics sufficiently. For demonstration of the deep penetration capabilities of the method, excised adult brains are imaged. Several brains are examined, measuring 2-3 mm on their short axis. The brains are highly scattering, yet the neurotomography system is capable of providing high-quality time-resolved three dimensional data (see Fig. 23.2, 23.3). The one-sided illumination limits the penetration depth of the excitation photons. As described above, the samples were illuminated from the side to avoid blinding of the fluorescence camera. This creates a bias of the fluence to one side of the sample. In the shown case, the illumination was capable of exciting the forebrain and most of the optic tectum

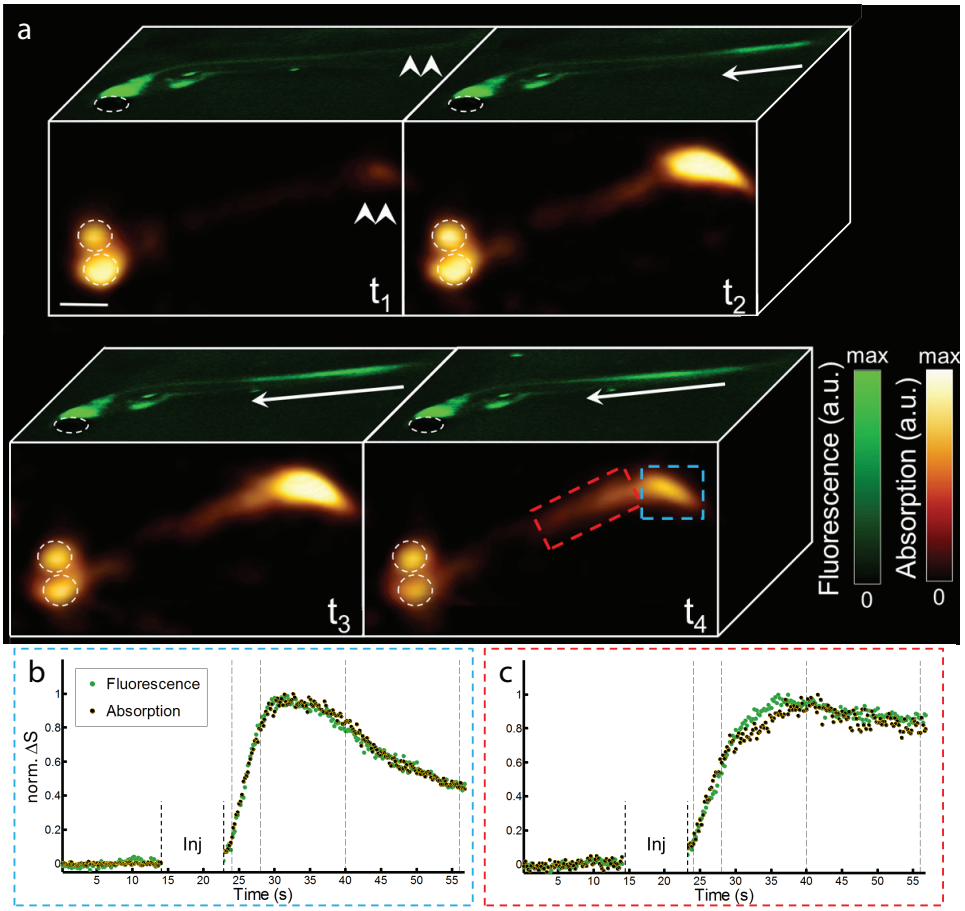

Figure 23.1: a. Planar epi-fluorescence (green) and 3D optoacoustic (brown) images of a 6 day old larvae at 4 time points post injection of PTZ show similar signal (scale bar - 500 μm). The arrows indicate the direction of the activation as it progresses from the posterior (site of injection marked by a double arrow) to the anterior part of the tail. b. Traces of the fluorescence and absorption (optoacoustic) signal changes in the posterior region of spinal cord (marked by red rectangle in panel A). The corresponding traces in the anterior region marked by the blue rectangle are shown in panel c. The time points shown in panel a are marked by vertical dotted lines. Since both the background fluorescence and optoacoustic signals were close or below the noise level, the changes in the signals ($\triangle$S) were normalised to unity instead of being divided by the respective resting signals. The injection phase caused image artefacts and is therefore excluded from the graphs.

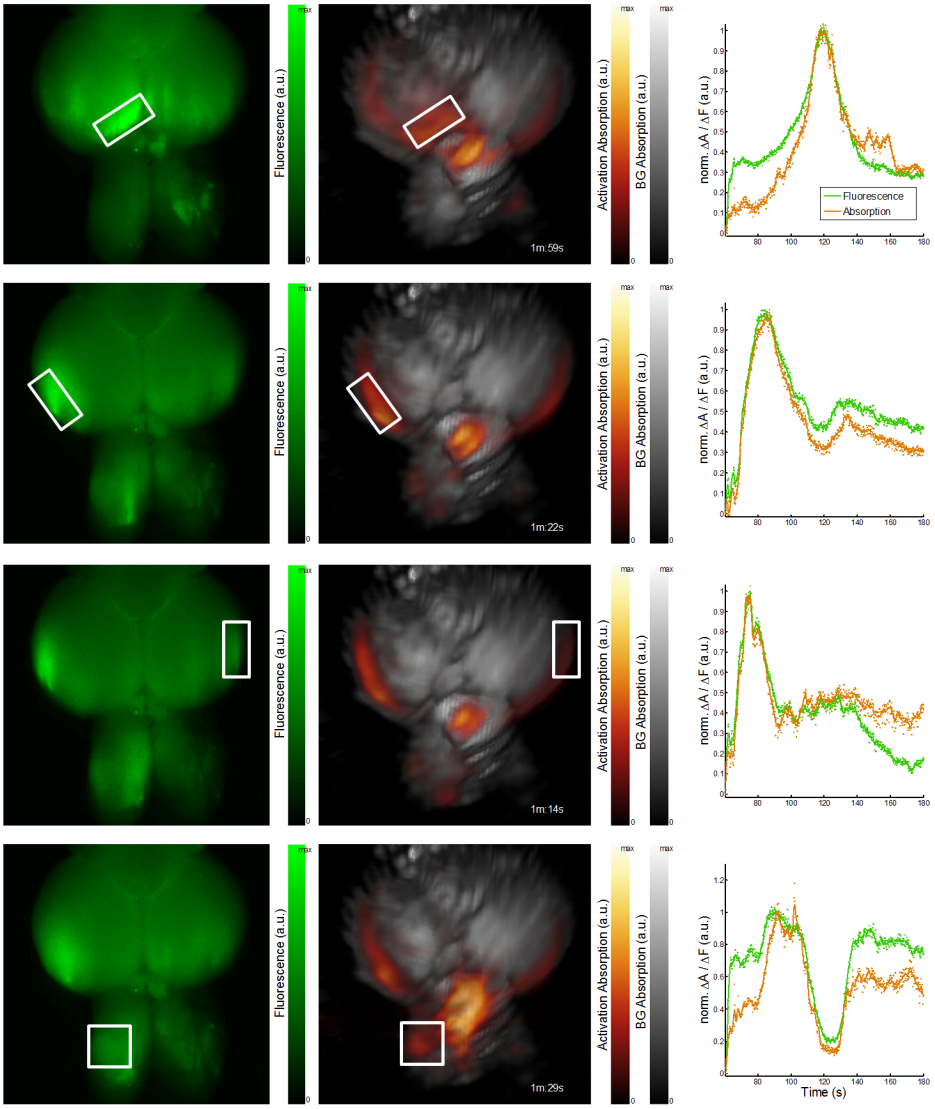

Figure 23.2: Strong correlation can be seen in selected regions of interest between fluctuations in the planar fluorescence images (left column) and the optoacoustic data (middle column). Normalised signal traces (right column) exhibit high similarities.

(OT). For analysis, five volumes of interest (VOIs) are selected to display the dynamics of the GCaMP5G activity. Figure 23.3 matches the absorption (optoacoustic) to the planar fluorescence activation traces. Analysis of the three dimensional optoacoustic data shows that the greatest activation-related changes, reaching a $\triangle A_{max}/A_0$ value of 8.5 are to be found deep within the tissue. These regions include the grey, pink, yellow and cyan VOIs in Figure 23.3, with more superficial VOIs, including the one marked in blue showing less extreme behaviours. The planar fluorescence images lack this information. The depth penetration is severely limited by scatting within the tissue and therefore cannot yield the same uniform resolution at depth as optoacoustics. The resulting images therefore represent a smeared and averaged surface representation of the true volumetric events [133].

Figure 23.3 therefore exemplifies that epifluorescence imaging is not able to acquire and illustrate the correct spatial and volumetric signals of the activation dynamics in scattering tissue, due to severe blurring.

23.2.3 Optoacoustic Imaging of Freely Swimming Larvae

Tracking neural activation during natural and unaltered behaviour remains as one of the great challenges of current neuroscientific research. Experiments conducted on immobilised, anaesthetised samples already offer great insights into the interconnectivity of neural networks, they however lack the the ever important natural behaviour component. Previous developments that include bioluminescence imaging [134] and light-sheet microscopy [135] have produced great first results in imaging the natural behaviour of zebrafish, are however limited in their volumetric imaging capabilities. The system described here is therefore tested for its applicability as such a natural behaviour imaging tool. The comparatively large field of view poses no limit on the ability to image neural activation simultaneously to the natural swimming behaviour of larvae. To test the high frame rate volumetric scanner, the larvae were placed in the agar mould acting as an imaging chamber, with an approximate footprint of 0.5 cm^2, allowing the larvae to navigate the chamber freely. During data acquisition, the larvae are then exposed to PTZ, causing the same transient calcium concentration change and resulting activation change, as described above. The activation agent elicits rapid movements of the larvae that are followed by long periods of complete rest. The optoacoustic data is able to reveal that the absorption changes of GCaMP5G amount to $\triangle A/A_0 = 1.8$ throughout the nervous system before the abrupt start of rapid tail motion initiates the quick movements (see Figure 23.4). A white arrow marks the spine of the fish in Figure 23.4, the site

where a strong increase is visible when comparing the first to the last frame. Rapid tail movement followed the frames shown here, thus translating the fish in the imaging chamber.

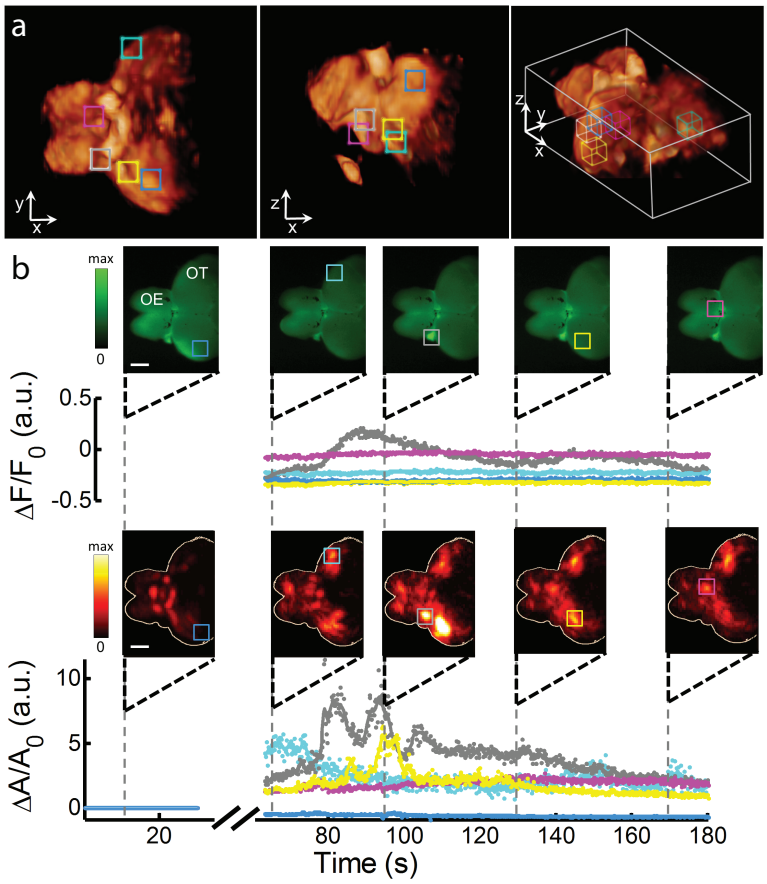

Figure 23.3: a. Typical 3D optoacoustic image acquired from a highly scattering brain of adult fish in its resting state (two side views and one isometric view of the 3D reconstruction are shown). The olfactory epithelium (OE) and most of the optic tectum (OT) are clearly visible. Five 300 μm x 300 μm x 300 μm VOIs were chosen at different locations and depths within the brain. b. Traces of the fluorescence (top) and optoacoustic (bottom) signal changes are shows for the five VOIs in corresponding colours (all signal changes are normalised to the resting signal levels). Note that the optoacoustic traces are calculated over volumes whereas the fluorescent signals are calculated over the roughly corresponding planar areas. Snapshots acquired at 5 different time points before and after introduction of the neuroactivation agent are shown (scale bar - 500 μm). The injection phase caused image artefacts and is therefore excluded from the graphs.

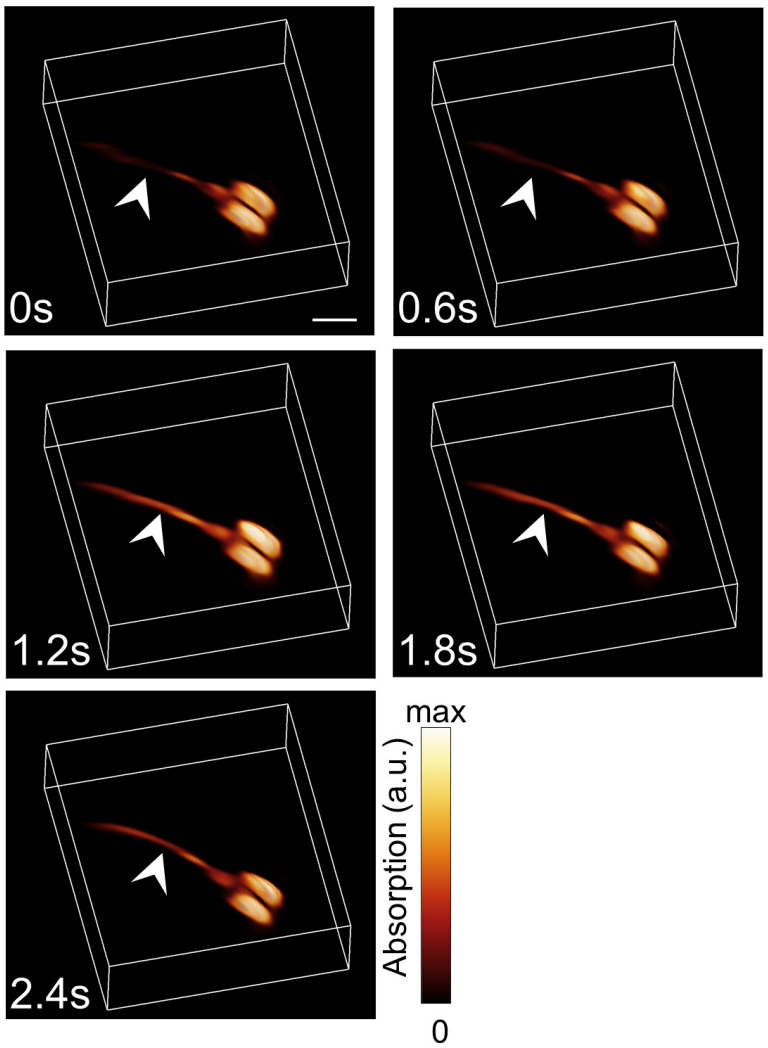

Figure 23.4: Time series of volumetric optoacoustic images from a freely swimming larva is shown. Following PTZ injection, the larva occasionally stops swimming while experiencing a surge of activation through its tail (the arrows point to the location of optoacoustic signal increase) before it starts moving promptly to a new position (notice movement of the tail in the last frame). Scale bar is 500 μm.

Chapter 24

Summary and Outlook

24.1 Summary

In summary, the optoacoustic neurotomography setup is shown to be capable of direct imaging of neural activation, yielding data with high spatio-temporal resolution, even deep within scattering brains. The experiments have shown that modern GECIs are viable contrast agents for optoacoustics. Specifically, GCaMP5G shows a direct relationship between its fluorescence increase and its optoacoustic response upon binding of calcium. This promises to open doors in combining established activatable microscopy probes with optoacoustics, to produce data showing responses with high spatial and temporal resolution.

By illuminating the samples with widely-tuneable nanosecond OPO lasers, the system is not limited to a small number of probes. The wavelength can be conveniently adjusted to fit the excitation spectrum of many different probes. These probes could include the next generation GCaMP6 [136] or red shifted examples like RGECO [137], with the only requirement being that the absorption and not just the molecular quantum yield changes upon activation. The flexible illumination therefore enables the neurotomography setup to become a multi-colour modality, exhibiting high spatial resolution at depth, without sacrificing temporal resolution. As there is no need to change the excitation and emission filters like in traditional optical imaging, the temporal resolution is merely limited by the wavelength switching speed of the laser, which in this case can be performed on a per pulse basis with a repetition frequency of 100 Hz.

The system proved its ability to image and track the movement and neural activation simultaneously in freely swimming larvae, creating the

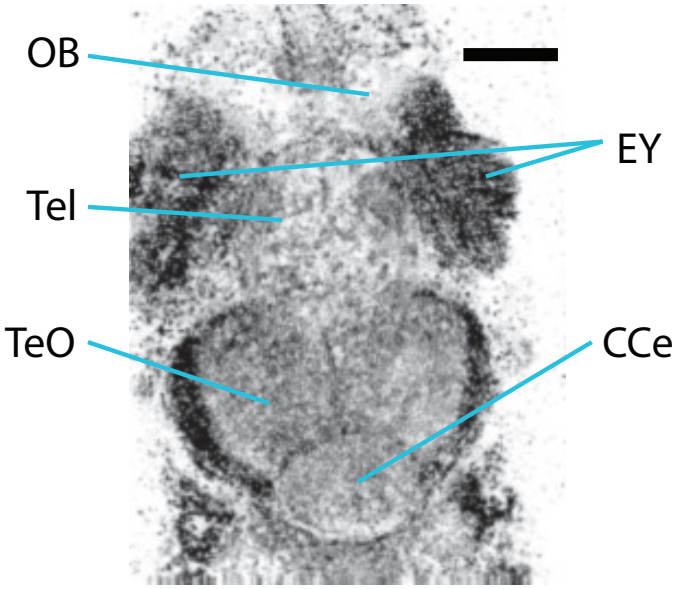

Figure 24.1: A projection image in z direction of optoacoustic micrsocopy data of an adult zebrafish brain reveals cortical structures. TeO - Tectum opticum, CCe - corpus cerebelli, Tel - telencephalon, EY - eye, OB - olfactory bulb. Scale bar is 750 μm.

possibility for previously impossible behavioural studies.

24.2 Outlook

While the system already produced great results in imaging zebrafish and tracking neural activation, potential for future developments remains. The setup already has an increased central frequency over the original design [32], [33], but as shown in Part IV, even higher frequency transducers can be used to acquire images with higher spatial resolution. Figure 24.1 shows an exemplary image of an adult zebrafish brain acquired with the optoacoustic microscope. Cortical structures are readily identifiable, even through the intact skull. This is highly promising for future devices that could yield unprecedented spatio-temporal resolution even at great depths, deep within scattering tissue. Behavioural studies with such imaging performance would also proof highly valuable.

Part VI

Thesis Summary, Future Directions and Final Remarks

24.3 Summary

In this thesis, several advances in the field of optoacoustic neuroimaging were presented. In doing so, an introduction to the theoretical background of optoacoustic was given and several types of optoacoustic imaging systems were introduced and compared to other imaging modalities. Three different setups were described in detail and neuroscientifically motivated applications were demonstrated. Overall, this thesis set out to answer questions that arise when fusing neurological research with optoacoustics. In more detail:

Part III showed the applicability of optoacoustics for functional neuroimaging. Functional blood parameters were resolved in a stroke study using the middle cerebral artery occlusion model. It was possible to identify an area of malperfused tissue, known as the penumbra. The study furthermore proved the non-invasive nature of the method, as the animals were scanned several times over 24 hours without being harmed. This set the scene for the continued efforts to evolve optoacoustics for neuroimaging applications and lead to the additional research described in this thesis.

Additionally, Part III was able to prove that optoacoustic setups can penetrate deep into the tissue thus enabling whole brain imaging of mice. The system used was however not perfect, and showed the need for further development. Clear limitations herein include the two-dimensional cross-sectional images and the low spatial resolution. In efforts to increase the resolution, Part IV introduced the concept of optoacoustic microscopy and described the development of a hybrid focus optoacoustic microscope, achieving high lateral resolution down to 20 μm. High resolution optoacoustic microscopy of the mouse brain is however challenged by the mouse skull, the attenuating effects of which on both the optical and acoustic path were described in Part IV.

Part V then described an alternative setup for high resolution volumetric imaging, using a tomography based approach. Furthermore, it proved the applicability of tracking neural activation through the absorbance traces of established genetically encoded calcium indicators. This direct imaging approach enables faster tracking of the neural responses as it does not suffer from time delays introduced by slower neurovascular effects. The part described the successful tracing of neural activation in free swimming and immobilised zebrafish larvae, as well as in excised, but activatable brains and validated the findings using planer fluorescence imaging.

24.4 Conclusion and Outlook

Overall, the work presented in this thesis includes promising advances in the combined field of optoacoustic neuroimaging. Imaging of the ischaemic penumbra is of high importance, as this area is one of the key areas of current efforts to develop new treatments and therapies for stroke. While the first results are promising, research in this area should continue and can potentially see great progress. Possible experiments could include the use of apoptosis probes that could be used to image not just the penumbra, but the growing ischaemic core simultaneously, thus yielding direct data of the transition between the two tissue statuses. Longitudinal tracking of injected labeled cells that potentially aid in the regeneration of the compromised area could provide valuable insights into this prospective therapy.

The hybrid microscopy system has shown great potential and can lead to a myriad of possible applications. Technological and theoretical developments would aid the setup in living up to its potential. These include, but are not limited to:

Steps should be taken to realise dual illumination to suit the hybrid focusing method. In order to fully utilise the transition between optical and acoustic focusing and thereby penetrate deep into the tissue, while retaining optical focusing at the tissue surface, broad illumination is needed. By coaxially aligning broad and focused illumination through a combination of multimode and photonic crystal fibers, enough energy could reach the deep tissue regions without breaking fluence limits set by the governing bodies.

Additionally, faster switching of the illumination wavelengths would open up the possibility to perform first multispectral scans, even with the limited number of wavelengths. Efforts have begun in realising the required developments.

As demonstrated, the skull still limits the achievable effective resolution in non-invasive neuroimaging. Correction algorithms treating the skull as a solid plate could help in recovering some of the losses introduced by the skull.

It was shown that direct imaging of neural activation is possible with optoacoustics. Direct imaging and monitoring of neural activation offers faster responses than tracking of the neurovascular effect. Red shifted calcium indicators should therefore be evaluated for use in high resolution applications (optoacoustic microscope or higher frequency iterations of the neurotomography system). In doing so, technologies for growing neuronal networks in a dish, such as bioengineered large-scale neuronal networks [114], could be promising tools in initial testing selection of promising indicators.

Overall, this thesis set the scene for a wealth of potential future applications that promise a bright future for optoacoustic neuroimaging.

Acknowledgements

I would not have been able to complete my thesis without the helpful support of a myriad of people. I would therefore like to start by thanking everyone at the Institute of Biological and Medical Imaging of the Helmholtz Zentrum München for the great and supportive atmosphere.
Special thanks goes to Prof. Dr. Daniel Razanksy for his supervision and supportive helpful insights, while working in his group.
Additionally, both Prof. Dr. Vasilis Ntziachristos and Prof. Dr. Gil Westmeyer offered their permanent and insightful support during the entirety of my PhD research.
Prof. Dr. Shy Shoham and his staff at the Technion in Haifa, Israel taught me valuable practical skills and kindly welcomed me into their group during my research stay at their lab.
Prof. Dr. Ute Lindauer was kind enough to support the initial study presented in this thesis with her wealth of knowledge concerning functional neuroimaging.
I would like to thank my office and work mates Jake Turner, Christian Lutzweiler, Hector Estrada and Amy Lin for their (sometimes) constructive criticism.
Deep thanks goes to Sarah Glasl, Uwe Klemm and Florian Jurgeleit for their support, whenever needed.
I lastly acknowledge the support and understanding of my friends and family.

Bibliography

[1] Liesi E Hebert, Laurel A Beckett, Paul A Scherr, and Denis A Evans. Annual incidence of alzheimer disease in the united states projected to the years 2000 through 2050. *Alzheimer Disease & Associated Disorders*, 15(4):169–173, 2001.

[2] Daniel M Skovronsky, Virginia M-Y Lee, and John Q Trojanowski. Neurodegenerative diseases: new concepts of pathogenesis and their therapeutic implications. *Annu. Rev. Pathol. Mech. Dis.*, 1:151–170, 2006.

[3] JPND Research. Why?, 2014.

[4] J. Olesen, A. Gustavsson, M. Svensson, H.-U. Wittchen, B. Jönsson, on behalf of the CDBE2010 study group, and the European Brain Council. The economic cost of brain disorders in europe. *European Journal of Neurology*, 19(1):155–162, 2012.

[5] Saving Lives. Saving money: Dividends for americans investing in alzheimer research. *A report from the Lewin Group, commissioned by the Alzheimer's Association. Washington, DC*, 2004.

[6] Karen Ritchie and Simon Lovestone. The dementias. *The Lancet*, 360(9347):1759–1766, 2002.

[7] Richard L Ernst, Joel W Hay, Catharine Fenn, Jared Tinklenberg, and Jerome A Yesavage. Cognitive function and the costs of alzheimer disease: an exploratory study. *Archives of neurology*, 54(6):687–693, 1997.

[8] Peter J Nestor, Philip Scheltens, and John R Hodges. Advances in the early detection of alzheimer's disease. 2004.

[9] Greg Zaharchuk, Masaru Yamada, Masao Sasamata, Bruce G Jenkins, Michael A Moskowitz, and Bruce R Rosen. Is all perfusion-weighted magnetic resonance imaging for stroke equal? the temporal evolution of multiple hemodynamic parameters after focal ischemia in rats correlated with evidence of infarction. *Journal of Cerebral Blood Flow & Metabolism*, 20(9):1341–1351, 2000.

[10] Walter E. Dandy. Ventriculography following the injection of air into the cerebral ventricles. *Annals of Surgery*, 68(1), 1918.

[11] Aaron Filler. The history, development and impact of computed imaging in neurological diagnosis and neurosurgery: Ct, mri, and dti. 2009.

[12] Jonathan S. Lewin. Functional mri: An introduction to methods. *Journal of Magnetic Resonance Imaging*, 17(3):383–383, 2003.

[13] Kelly M. A history of the electrical activity of the brain: The first half-century. *Archives of Internal Medicine*, 110(6):932–934, 1962.

[14] Robert L. Savoy. History and future directions of human brain mapping and functional neuroimaging. *Acta Psychologica*, 107(1–3):9 – 42, 2001. Beyond the decade of the brain: Towards functional neuronanatomy of the mind.

[15] JW Belliveau, DN Kennedy, RC McKinstry, BR Buchbinder, RM Weisskoff, MS Cohen, JM Vevea, TJ Brady, and BR Rosen. Functional mapping of the human visual cortex by magnetic resonance imaging. *Science*, 254(5032):716–719, 1991.

[16] Peter A. Bandettini. Functional mri: A confluence of fortunate circumstances. *NeuroImage*, 61(2):A3 – A11, 2012.

[17] Alexander Graham Bell. On the production an reproduction of sound by light. *American Journal of Science*, 20(305):24, 1880.

[18] Andrew C. Tam. Applications of photoacoustic sensing techniques. *Rev. Mod. Phys.*, 58:381–431, Apr 1986.

[19] Günther Tölg. Photoacoustics and photoacoustic spectroscopy. von a. rosencwaig. wiley and sons, chichester 1980; xii, 309 s., 139 abb., geb. £ 19.00. *Angewandte Chemie*, 94(3):229–229, 1982.

[20] Changhui Li and Lihong V Wang. Photoacoustic tomography and sensing in biomedicine. *Physics in Medicine and Biology*, 54(19):R59, 2009.

[21] G. J. Diebold, T. Sun, and M. I. Khan. Photoacoustic monopole radiation in one, two, and three dimensions. *Phys. Rev. Lett.*, 67:3384–3387, Dec 1991.

[22] Robert A. Kruger, Pingyu Liu, Yuncai "Richard" Fang, and C. Robert Appledorn. Photoacoustic ultrasound (paus)—reconstruction tomography. *Medical Physics*, 22(10):1605–1609, 1995.

[23] Ralph Weissleder and Vasilis Ntziachristos. Shedding light onto live molecular targets. *Nature medicine*, 9(1):123–128, 2003.

[24] Laser Institute of America (2007). *American National Standard for Safe Use of Lasers, ANSI Z136.1.* 2007, ISBN: 978-1-940168-00-5. https://www.lia.org/store/ANSI/106.

[25] Rana A Fine and Frank J Millero. Compressibility of water as a function of temperature and pressure. *The Journal of Chemical Physics*, 59(10):5529–5536, 1973.

[26] Allan Rosencwaig. *Photoacoustics and photoacoustic spectroscopy.* Wiley, 1980.

[27] Robert A Kruger. Photoacoustic ultrasound. *Medical physics*, 21(1):127–131, 1994.

[28] Xueding Wang, Yongjiang Pang, Geng Ku, Xueyi Xie, George Stoica, and Lihong V Wang. Noninvasive laser-induced photoacoustic tomography for structural and functional in vivo imaging of the brain. *Nature biotechnology*, 21(7):803–806, 2003.

[29] Daniel Razansky, Claudio Vinegoni, and Vasilis Ntziachristos. Multispectral photoacoustic imaging of fluorochromes in small animals. *Optics letters*, 32(19):2891–2893, 2007.

[30] Daniel Razansky, Martin Distel, Claudio Vinegoni, Rui Ma, Norbert Perrimon, Reinhard W Köster, and Vasilis Ntziachristos. Multispectral opto-acoustic tomography of deep-seated fluorescent proteins in vivo. *Nature Photonics*, 3(7):412–417, 2009.

[31] Andreas Buehler, Amir Rosenthal, Thomas Jetzfellner, Alexander Dima, Daniel Razansky, and Vasilis Ntziachristos. Model-based optoacoustic inversions with incomplete projection data. *Medical physics*, 38(3):1694–1704, 2011.

[32] Xosé Luís Deán-Ben and Daniel Razansky. Functional optoacoustic human angiography with handheld video rate three dimensional scanner. *Photoacoustics*, 1(3):68–73, 2013.

[33] X Dean Ben, A Oezbek, and Daniel Razansky. Volumetric real-time tracking of peripheral human vasculature with gpu-accelerated three-dimensional optoacoustic tomography. 2013.

[34] Héctor Estrada, Jake Turner, Moritz Kneipp, and Daniel Razansky. Real-time optoacoustic brain microscopy with hybrid optical and acoustic resolution. *Laser Physics Letters*, 11(4):045601, 2014.

[35] Shriram Sethuraman, Salavat R Aglyamov, James H Amirian, Richard W Smalling, and Stanislav Y Emelianov. Intravascular photoacoustic imaging using an ivus imaging catheter. *Ultrasonics, Ferroelectrics and Frequency Control, IEEE Transactions on*, 54(5):978–986, 2007.

[36] Joon-Mo Yang, Konstantin Maslov, Hao-Chung Yang, Qifa Zhou, K Kirk Shung, and Lihong V Wang. Photoacoustic endoscopy. *Optics letters*, 34(10):1591–1593, 2009.

[37] Christian Lutzweiler, Reinhard Meier, Ernst Rummeny, Vasilis Ntziachristos, and Daniel Razansky. Real-time optoacoustic tomography of indocyanine green perfusion and oxygenation parameters in human finger vasculature. *Optics letters*, 39(14):4061–4064, 2014.

[38] A.G. Webb. *Introduction to Biomedical Imaging*. IEEE Press Series on Biomedical Engineering. Wiley, 2002.

[39] John P McGahan and Barry B Goldberg. *Diagnostic ultrasound*, volume 1. Informa Health Care, 2008.

[40] Terry J DuBose. Fetal biometry vertical calvarial diameter and calvarial volume. *Journal of Diagnostic Medical Sonography*, 1(5):205–217, 1985.

[41] Claude Franceschi. *L'investigation vasculaire par ultrasonographie Doppler*. Masson, 1979.

[42] Vasilis Ntziachristos and Daniel Razansky. Molecular imaging by means of multispectral optoacoustic tomography (msot). *Chemical reviews*, 110(5):2783–2794, 2010.

[43] William H Oldendorf. The quest for an image of brain a brief historical and technical review of brain imaging techniques. *Neurology*, 28(6):517–517, 1978.

[44] Jerrold T Bushberg and John M Boone. *The essential physics of medical imaging*. Lippincott Williams & Wilkins, 2011.

[45] Hal O Anger. Scintillation camera. *Review of scientific instruments*, 29(1):27–33, 1958.

[46] JW Scuffham, MD Wilson, P Seller, MC Veale, PJ Sellin, SDM Jacques, and RJ Cernik. A cdte detector for hyperspectral spect imaging. *Journal of Instrumentation*, 7(08):P08027, 2012.

[47] Stephan A Mayer, Angela Lignelli, Matthew E Fink, Deborah B Kessler, Carole E Thomas, Rupendra Swarup, and Ronald L Van Heertum. Perilesional blood flow and edema formation in acute intracerebral hemorrhage a spect study. *Stroke*, 29(9):1791–1798, 1998.

[48] Michael E Phelps. *PET: molecular imaging and its biological applications*. Springer, 2004.

[49] Michel M Ter-Pogossian, Nizar A Mullani, John Hood, Carol S Higglns, and C Michael Currie. A multislice positron emission computed tomograph (pett iv) yielding transverse and longitudinal images 1. *Radiology*, 128(2):477–484, 1978.

[50] Paul C Lauterbur et al. Image formation by induced local interactions: examples employing nuclear magnetic resonance. *Nature*, 242(5394):190–191, 1973.

[51] DJ Bryant, JA Payne, DN Firmin, and DB Longmore. Measurement of flow with nmr imaging using a gradient pulse and phase difference technique. *Journal of computer assisted tomography*, 8(4):588–593, 1984.

[52] Costas Balas. Review of biomedical optical imaging—a powerful, noninvasive, non-ionizing technology for improving in vivo diagnosis. *Measurement science and technology*, 20(10):104020, 2009.

[53] AP Gibson, JC Hebden, and Simon R Arridge. Recent advances in diffuse optical imaging. *Physics in medicine and biology*, 50(4):R1, 2005.

[54] Gary D Luker and Kathryn E Luker. Optical imaging: current applications and future directions. *Journal of Nuclear Medicine*, 49(1):1–4, 2008.

[55] European Stroke Organisation (ESO). Stroke facts, 2014.

[56] European Stroke Network. Research background, 2014.

[57] Jeremiah F Kelly and Carol H Winograd. A functional approach to stroke management in elderly patients. *Journal of the American Geriatrics Society*, 1985.

[58] Stroke Center. Ischemic stroke, 2014.

[59] Stroke Association. Stroke treatments, 2014.

[60] Andrew R Xavier, Adnan I Qureshi, Jawad F Kirmani, Abutaher M Yahia, and Rohit Bakshi. Neuroimaging of stroke: a review. *Southern medical journal*, 96(4):367–379, 2003.

[61] W-D Heiss, R Graf, K Wienhard, J Löttgen, R Saito, T Fujita, G Rosner, and R Wagner. Dynamic penumbra demonstrated by sequential multitracer pet after middle cerebral artery occlusion in cats. *Journal of Cerebral Blood Flow & Metabolism*, 14(6):892–902, 1994.

[62] Lingfeng Yu, Elaine Nguyen, Gangjun Liu, Bernard Choi, and Zhongping Chen. Spectral doppler optical coherence tomography imaging of localized ischemic stroke in a mouse model. *Journal of biomedical optics*, 15(6):066006–066006, 2010.

[63] Moritz Kneipp, Jake Turner, Sebastian Hambauer, Sandro M Krieg, Jens Lehmberg, Ute Lindauer, and Daniel Razansky. Functional real-time optoacoustic imaging of middle cerebral artery occlusion in mice. *PloS one*, 9(4):e96118, 2014.

[64] Daniel Razansky, Andreas Buehler, and Vasilis Ntziachristos. Volumetric real-time multispectral optoacoustic tomography of biomarkers. *Nat. Protocols*, 6(8):1121–1129, 07 2011.

[65] Rui Ma, Adrian Taruttis, Vasilis Ntziachristos, and Daniel Razansky. Multispectral optoacoustic tomography (msot) scanner for whole-body small animal imaging. *Optics express*, 17(24):21414–21426, 2009.

[66] Daniel Razansky and Vasilis Ntziachristos. Hybrid photoacoustic fluorescence molecular tomography using finite-element-based inversion. *Medical physics*, 34(11):4293–4301, 2007.

[67] Kornel P Köstli, Martin Frenz, Hans Bebie, and Heinz P Weber. Temporal backward projection of optoacoustic pressure transients using fourier transform methods. *Physics in medicine and biology*, 46(7):1863, 2001.

[68] Minghua Xu and Lihong V Wang. Universal back-projection algorithm for photoacoustic computed tomography. *Physical Review E*, 71(1):016706, 2005.

[69] Christoph GA Hoelen, Frits FM de Mul, et al. Image reconstruction for photoacoustic scanning of tissue structures. *Applied Optics*, 39(31):5872–5883, 2000.

[70] Amir Rosenthal, Daniel Razansky, and Vasilis Ntziachristos. Fast semi-analytical model-based acoustic inversion for quantitative optoacoustic tomography. *Medical Imaging, IEEE Transactions on*, 29(6):1275–1285, 2010.

[71] Christopher C Paige and Michael A Saunders. Lsqr: An algorithm for sparse linear equations and sparse least squares. *ACM Transactions on Mathematical Software (TOMS)*, 8(1):43–71, 1982.

[72] Amir Rosenthal, Vasilis Ntziachristos, and Daniel Razansky. Model-based optoacoustic inversion with arbitrary-shape detectors. *Medical physics*, 38(7):4285–4295, 2011.

[73] Adrian Taruttis, Stefan Morscher, Neal C Burton, Daniel Razansky, and Vasilis Ntziachristos. Fast multispectral optoacoustic tomography (msot) for dynamic imaging of pharmacokinetics and biodistribution in multiple organs. *PloS one*, 7(1):e30491, 2012.

[74] Jürgen Glatz, Nikolaos C Deliolanis, Andreas Buehler, Daniel Razansky, and Vasilis Ntziachristos. Blind source unmixing in multi-spectral optoacoustic tomography. *Optics express*, 19(4):3175–3184, 2011.

[75] Mark J Niedre, Gordon M Turner, and Vasilis Ntziachristos. Time-resolved imaging of optical coefficients through murine chest cavities. *Journal of biomedical optics*, 11(6):064017–064017, 2006.

[76] Jung-Taek Oh, George Stoica, Lihong V Wang, Meng-Lin Li, Hao F Zhang, and Konstantin Maslov. Three-dimensional imaging of skin melanoma in vivo by dual-wavelength photoacoustic microscopy. *Journal of biomedical optics*, 11(3):034032–034032, 2006.

[77] Zhun Xu, Changhui Li, and Lihong V Wang. Photoacoustic tomography of water in phantoms and tissue. *Journal of biomedical optics*, 15(3):036019–036019, 2010.

[78] Yun-Sheng Chen, Wolfgang Frey, Seungsoo Kim, Pieter Kruizinga, Kimberly Homan, and Stanislav Emelianov. Silica-coated gold nanorods as photoacoustic signal nanoamplifiers. *Nano letters*, 11(2):348–354, 2011.

[79] Terrance Chiang, Robert O Messing, and Wen-Hai Chou. Mouse model of middle cerebral artery occlusion. *Journal of visualized experiments: JoVE*, (48), 2011.

[80] Ulrich Dirnagl et al. Standard operating procedures (sop) in experimental stroke research: Sop for middle cerebral artery occlusion in the mouse. *Nat. Precedings*, 19:1–10, 2010.

[81] Masaya Oda, Taku Sugawara, Kohei Kokubun, Kazuo Mizoi, and Hiroyuki Kinouchi. Intraluminal middle cerebral artery occlusion model in mice. In *Animal Models of Acute Neurological Injuries*, pages 197–205. Springer, 2009.

[82] Ferdi A van Dorsten, Ryuji Hata, Keiichiro Maeda, Claudia Franke, Manfred Eis, Konstantin-Alexander Hossmann, and Mathias Hoehn. Diffusion-and perfusion-weighted mr imaging of transient focal cerebral ischaemia in mice. *NMR in Biomedicine*, 12(8):525–534, 1999.

[83] Shimin Liu, Honglian Shi, Wenlan Liu, Takamitsu Furuichi, Graham S Timmins, and Ke Jian Liu. Interstitial po2 in ischemic penumbra and core are differentially affected following transient focal cerebral ischemia in rats. *Journal of Cerebral Blood Flow & Metabolism*, 24(3):343–349, 2004.

[84] Zilin Deng, Zhen Wang, Xiaoquan Yang, Qingming Luo, and Hui Gong. In vivo imaging of hemodynamics and oxygen metabolism in acute focal cerebral ischemic rats with laser speckle imaging and functional photoacoustic microscopy. *Journal of biomedical optics*, 17(8):0814151–0814159, 2012.

[85] Junjie Yao, Chih-Hsien Huang, Lidai Wang, Joon-Mo Yang, Liang Gao, Konstantin I Maslov, Jun Zou, and Lihong V Wang. Wide-field fast-scanning photoacoustic microscopy based on a water-immersible mems scanning mirror. *Journal of biomedical optics*, 17(8):0805051–0805053, 2012.

[86] Lei Li, Chenghung Yeh, Song Hu, Lidai Wang, Brian T Soetikno, Ruimin Chen, Qifa Zhou, K Kirk Shung, Konstantin I Maslov, and Lihong V Wang. Fully motorized optical-resolution photoacoustic microscopy. *Optics letters*, 39(7):2117–2120, 2014.

[87] Rui Ma, Sebastian Söntges, Shy Shoham, Vasilis Ntziachristos, and Daniel Razansky. Fast scanning coaxial optoacoustic microscopy. *Biomedical optics express*, 3(7):1724–1731, 2012.

[88] Christoph Cremer. Lichtmikroskopie unterhalb des abbe-limits. lokalisationsmikroskopie. *Physik in unserer Zeit*, 42(1):21–29, 2011.

[89] Vasilis Ntziachristos. Going deeper than microscopy: the optical imaging frontier in biology. *Nature methods*, 7(8):603–614, 2010.

[90] Hao F Zhang, Konstantin Maslov, and Lihong V Wang. In vivo imaging of subcutaneous structures using functional photoacoustic microscopy. *Nature protocols*, 2(4):797–804, 2007.

[91] Meng-Lin Li, Hao F Zhang, Konstantin Maslov, George Stoica, and Lihong V Wang. Improved in vivo photoacoustic microscopy based on a virtual-detector concept. *Optics letters*, 31(4):474–476, 2006.

[92] Ivo M Vellekoop and Christof M Aegerter. Scattered light fluorescence microscopy: imaging through turbid layers. *Optics letters*, 35(8):1245–1247, 2010.

[93] Héctor Estrada, Emil Sobol, Olga Baum, and Daniel Razansky. Hybrid optoacoustic and ultrasound biomicroscopy monitors' laser-induced tissue modifications and magnetite nanoparticle impregnation. *Laser Physics Letters*, 11(12):125601, 2014.

[94] Michael Brand, Michael Granato, and Christiane Nüsslein-Volhard. Keeping and raising zebrafish. *Zebrafish*, 261:7–37, 2002.

[95] Moritz Kneipp, Héctor Estrada, Antonella Lauri, Jake Turner, Vasilis Ntziachristos, Gil G Westmeyer, and Daniel Razansky. Volumetric

tracking of migratory melanophores during zebrafish development by optoacoustic microscopy. *Mechanisms of Development*, 2015.

[96] Herbert Schneckenburger, Petra Weber, Michael Wagner, Thomas Bruns, Verena Richter, Sarah Schickinger, and Rainer Wittig. Multidimensional fluorescence microscopy in live cell imaging–a mini review. *Photonics and Lasers in Medicine*, 1(1):35–40, 2012.

[97] Kevin Curran, David W Raible, and James A Lister. Foxd3 controls melanophore specification in the zebrafish neural crest by regulation of mitf. *Developmental biology*, 332(2):408–417, 2009.

[98] Mary A Bedell, David A Largaespada, Nancy A Jenkins, and Neal G Copeland. Mouse models of human disease. part ii: recent progress and future directions. *Genes & development*, 11(1):11–43, 1997.

[99] Moritz Kneipp, Jake Turner, Héctor Estrada, Johannes Rebling, Shy Shoham, and Daniel Razansky. Effects of the murine skull in optoacoustic brain microscopy. *Journal of biophotonics*, 9999, 2015.

[100] Igor Aleksandrovich Viktorov. *Rayleigh and Lamb waves: physical theory and applications*, volume 147. Plenum press New York, 1967.

[101] Tribikram Kundu. *Ultrasonic nondestructive evaluation: engineering and biological material characterization*. CRC press, 2004.

[102] Jill Peterson and Paul C Dechow. Material properties of the inner and outer cortical tables of the human parietal bone. *The Anatomical Record*, 268(1):7–15, 2002.

[103] PJ White, GT Clement, and K Hynynen. Longitudinal and shear mode ultrasound propagation in human skull bone. *Ultrasound in medicine & biology*, 32(7):1085–1096, 2006.

[104] Philip Palin Dendy and Brian Heaton. *Physics for diagnostic radiology*. CRC Press, 2011.

[105] Chao Huang, Liming Nie, Robert W Schoonover, Zijian Guo, Carsten O Schirra, Mark A Anastasio, and Lihong V Wang. Aberration correction for transcranial photoacoustic tomography of primates employing adjunct image data. *Journal of biomedical optics*, 17(6):0660161–0660168, 2012.

[106] Jake Turner, Héctor Estrada, Moritz Kneipp, and Daniel Razansky. Improved optoacoustic microscopy through three-dimensional spatial impulse response synthetic aperture focusing technique. *Optics Letters*, 39(12):3390–3393, 2014.

[107] Tong Jianbin, Huang Liang, Huang Jufang, Wang Hui, Chen Dan, Zeng Leping, Zhou Jin, and Luo Xuegang. Improved method of ink-gelatin perfusion for visualising rat retinal microvessels. *Acta histochemica et cytochemica*, 41(5):127, 2008.

[108] Guang Yang, Feng Pan, Christopher N Parkhurst, Jaime Grutzendler, and Wen-Biao Gan. Thinned-skull cranial window technique for long-term imaging of the cortex in live mice. *Nature protocols*, 5(2):201–208, 2010.

[109] K. Iwansson, G. Sinapius, W. Hoornaert, and S. Middelhoek. *Measuring Current, Voltage and Power*. Handbook of Sensors and Actuators. Elsevier Science, 1999.

[110] Jason ND Kerr and Winfried Denk. Imaging in vivo: watching the brain in action. *Nature Reviews Neuroscience*, 9(3):195–205, 2008.

[111] Lin Tian, S Andrew Hires, Tianyi Mao, Daniel Huber, M Eugenia Chiappe, Sreekanth H Chalasani, Leopoldo Petreanu, Jasper Akerboom, Sean A McKinney, Eric R Schreiter, et al. Imaging neural activity in worms, flies and mice with improved gcamp calcium indicators. *Nature methods*, 6(12):875–881, 2009.

[112] Joseph R Fetcho, Kingsley JA Cox, and Donald M O'Malley. Monitoring activity in neuronal populations with single-cell resolution in a behaving vertebrate. *The Histochemical journal*, 30(3):153–167, 1998.

[113] Hillel Adesnik, Laura Waller, and Shy Shoham. Optics on the brain: Osa's mulitphoton and patterned optogenetics incubator. *Optics and Photonics News*, 25(4):42–49, 2014.

[114] Hod Dana, Anat Marom, Shir Paluch, Roman Dvorkin, Inbar Brosh, and Shy Shoham. Hybrid multiphoton volumetric functional imaging of large-scale bioengineered neuronal networks. *Nature Communications*, 5, 2014.

[115] Misha B Ahrens, Michael B Orger, Drew N Robson, Jennifer M Li, and Philipp J Keller. Whole-brain functional imaging at cellular resolution using light-sheet microscopy. *Nature methods*, 10(5):413–420, 2013.

[116] Tina Schrödel, Robert Prevedel, Karin Aumayr, Manuel Zimmer, and Alipasha Vaziri. Brain-wide 3d imaging of neuronal activity in caenorhabditis elegans with sculpted light. *Nature methods*, 10(10):1013–1020, 2013.

[117] Robert Prevedel, Young-Gyu Yoon, Maximilian Hoffmann, Nikita Pak, Gordon Wetzstein, Saul Kato, Tina Schrödel, Ramesh Raskar, Manuel Zimmer, Edward S Boyden, et al. Simultaneous whole-animal 3d imaging of neuronal activity using light-field microscopy. *Nature methods*, 2014.

[118] Oded Tour, Stephen R Adams, Rex A Kerr, Rene M Meijer, Terrence J Sejnowski, Richard W Tsien, and Roger Y Tsien. Calcium green flash as a genetically targeted small-molecule calcium indicator. *Nature chemical biology*, 3(7):423–431, 2007.

[119] Lin Tian, S Andrew Hires, and Loren L Looger. Imaging neuronal activity with genetically encoded calcium indicators. *Cold Spring Harbor Protocols*, 2012(6):pdb–top069609, 2012.

[120] Marco Mank, Alexandre Ferrao Santos, Stephan Direnberger, Thomas D Mrsic-Flogel, Sonja B Hofer, Valentin Stein, Thomas Hendel, Dierk F Reiff, Christiaan Levelt, Alexander Borst, et al. A genetically encoded calcium indicator for chronic in vivo two-photon imaging. *Nature methods*, 5(9):805–811, 2008.

[121] Jasper Akerboom, Tsai-Wen Chen, Trevor J Wardill, Lin Tian, Jonathan S Marvin, Sevinç Mutlu, Nicole Carreras Calderón, Federico Esposti, Bart G Borghuis, Xiaonan Richard Sun, et al. Optimization of a gcamp calcium indicator for neural activity imaging. *The Journal of Neuroscience*, 32(40):13819–13840, 2012.

[122] BERTIL HILLE. Pumping ions, 1992.

[123] Amy E Palmer, Marta Giacomello, Tanja Kortemme, S Andrew Hires, Varda Lev-Ram, David Baker, and Roger Y Tsien. Ca¡ sup¿ 2+¡/sup¿ indicators based on computationally redesigned calmodulin-peptide pairs. *Chemistry & biology*, 13(5):521–530, 2006.

[124] Filippo Del Bene, Claire Wyart, Estuardo Robles, Amanda Tran, Loren Looger, Ethan K Scott, Ehud Y Isacoff, and Herwig Baier. Filtering of visual information in the tectum by an identified neural circuit. *Science*, 330(6004):669–673, 2010.

[125] Johannes D Seelig, M Eugenia Chiappe, Gus K Lott, Anirban Dutta, Jason E Osborne, Michael B Reiser, and Vivek Jayaraman. Two-photon calcium imaging from head-fixed drosophila during optomotor walking behavior. *Nature methods*, 7(7):535–540, 2010.

[126] Bart G Borghuis, Lin Tian, Ying Xu, Sergei S Nikonov, Noga Vardi, Boris V Zemelman, and Loren L Looger. Imaging light responses of targeted neuron populations in the rodent retina. *The Journal of Neuroscience*, 31(8):2855–2867, 2011.

[127] Alexander Dima and Vasilis Ntziachristos. Non-invasive carotid imaging using optoacoustic tomography. *Optics express*, 20(22):25044–25057, 2012.

[128] Monte Westerfield. *The zebrafish book: a guide for the laboratory use of zebrafish (Danio rerio)*. University of Oregon Press, 2000.

[129] SC Baraban, MR Taylor, PA Castro, and H Baier. Pentylenetetrazole induced changes in zebrafish behavior, neural activity and c-fos expression. *Neuroscience*, 131(3):759–768, 2005.

[130] FM Leweke, J Louvel, G Rausche, and U Heinemann. Effects of pentetrazol on neuronal activity and on extracellular calcium concentration in rat hippocampal slices. *Epilepsy research*, 6(3):187–198, 1990.

[131] Kaori Tomizawa, Junn-ichi Kunieda, and Hiroshi Nakayasu. Ex vivo culture of isolated zebrafish whole brain. *Journal of neuroscience methods*, 107(1):31–38, 2001.

[132] James G McElligott, Phyllis Beeton, and Jeffrey Polk. Effect of cerebellar inactivation by lidocaine microdialysis on the vestibuloocular reflex in goldfish. *Journal of neurophysiology*, 79(3):1286–1294, 1998.

[133] Andreas Buehler, Eva Herzog, Angelica Ale, Bradley D Smith, Vasilis Ntziachristos, and Daniel Razansky. High resolution tumor targeting in living mice by means of multispectral optoacoustic tomography. *EJNMMI Res*, 2:14, 2012.

[134] Eva A Naumann, Adam R Kampff, David A Prober, Alexander F Schier, and Florian Engert. Monitoring neural activity with bioluminescence during natural behavior. *Nature neuroscience*, 13(4):513–520, 2010.

[135] Nikita Vladimirov, Yu Mu, Takashi Kawashima, Davis V Bennett, Chao-Tsung Yang, Loren L Looger, Philipp J Keller, Jeremy Freeman, and Misha B Ahrens. Light-sheet functional imaging in fictively behaving zebrafish. *Nature methods*, 2014.

[136] Tsai-Wen Chen, Trevor J Wardill, Yi Sun, Stefan R Pulver, Sabine L Renninger, Amy Baohan, Eric R Schreiter, Rex A Kerr, Michael B Orger, Vivek Jayaraman, et al. Ultrasensitive fluorescent proteins for imaging neuronal activity. *Nature*, 499(7458):295–300, 2013.

[137] Jasper Akerboom, Nicole Carreras Calderón, Lin Tian, Sebastian Wabnig, Matthias Prigge, Johan Tolö, Andrew Gordus, Michael B Orger, Kristen E Severi, John J Macklin, et al. Genetically encoded calcium indicators for multi-color neural activity imaging and combination with optogenetics. *Frontiers in molecular neuroscience*, 6, 2013.

Publications and Presentations

Peer Reviewed Papers

Kneipp, M., Turner, J., Hambauer, S., Krieg, S. M., Lehmberg, J., Lindauer, U., & Razansky, D. (2014). Functional Real-Time Optoacoustic Imaging of Middle Cerebral Artery Occlusion in Mice. PloS one, 9(4), e96118.

Estrada, H., Turner, J., **Kneipp, M.**, & Razansky, D. (2014). Real-time optoacoustic brain microscopy with hybrid optical and acoustic resolution. Laser Physics Letters, 11(4), 045601.

Turner, J., Estrada, H., **Kneipp, M.**, & Razansky, D. (2014). Improved optoacoustic microscopy through three-dimensional spatial impulse response synthetic aperture focusing technique. Optics Letters, 39(12), 3390-3393.

Kneipp, M., Turner, J., Estrada, H., Rebling, J. Shoham, S., & Razansky, D. (2015). Effects of murine skull in optoacoustic brain microscopy. Journal of biophotonics, 9999.

Sela, G., Lauri, A., Daán-Ben, XL., **Kneipp, M.**, Shoham, S., Westmeyer, GG., & Razansky, D. Functional five-dimensional optoacoustic neuro-tomography (FONT) for whole-brain monitoring of calcium indicators. *submitted*

Kneipp, M., Estrada, H., Lauri, A., Turner, J.,Ntziachristos, V., Westmeyer, GG., & Razansky, D. (2015). Volumetric tracking of migratory melanophores during zebrafish development by optoacoustic microscopy. Mechanisms of Development.

Jiang Y., Sigmund F., Reber, J., Deán-Ben, XL., Glasl, S., **Kneipp, M.**, Estrada, H., Razansky, D., Ntziachristos, V., & Westmeyer, GG. Violacein as a genetically-controlled, enzymatically amplified and photobleaching-

resistant chromophore for optoacoustic bacterial imaging. Scientific reports, 5.

Conference Proceedings and Presentation

Kneipp, M., Turner, J., Hambauer, S., Krieg, S. M., Lehmberg, J., Lindauer, U., & Razansky, D. (2014, March). Real-time optoacoustic monitoring of stroke. In SPIE BiOS (pp. 89430L-89430L). International Society for Optics and Photonics. *Oral presentation & Proceedings*

Kneipp, M., Estrada, H., Lauri, A., Westmeyer, GG., & Razansky, D. Zebrafish imaging by means of volumetric optoacoustic microscopy. Munich Interact 2014. *Oral presentation*

Glossary

aCSF artificial Cerebral Spinal Fluid.

AD Alzheimer's disease.

AR-OAM Acoustic Resolution Optoacoustic Microscopy.

CBV cerebral blood volume.

CCA common carotid artery.

DAQ digital acquisition platform.

dpf days post fertilisation.

ECA external carotid artery.

EEG electroencephalography.

GECI Genetically Encoded Calcium Indicator.

GRIN gradient-index.

Hb deoxygenated haemoglobin.

HbO_2 oxygenated haemoglobin.

hpf hours post fertilisation.

ICA middle carotid artery.

ICG indocyanine green.

MCA middle cerebral artery.

MCAO middle cerebral artery occlusion.

MFP mean free path.

MND Motor neurone diseases.

MRI Magnetic Resonance Imaging.

MSOT Multispectral Optoacoustic Tomography.

NIR near infrared.

OA optoacoustic.

OAM Optoacoustic Microscopy.

OE olfactory epithelium.

OI optical imaging.

OPO optical parametric oscillator.

OR-OAM Optical Resolution Optoacoustic Microscopy.

OT optic tectum.

PBS phosphate buffered saline.

PC personal computer.

PCA principal component analysis.

PD Parkinson's disease.

PET Positron Emission Tomography.

PTZ Pentylenetetrazole.

PVdF Polyvinylidene Fluoride.

ROI region of interest.

SNR signal-to-noise ratio.

SPECT Single Photon Emission Tomography.

tPA tissue plasminogen activator.

US ultrasound.

VOI volume of interest.

XCT X-ray computed tomography.

List of Figures